

ABSTRACT

Dissertation Title : Development of Magnetic Field Sensors Using
Bismuth – Substituted Garnets Thin Films with
In-Plane Magnetization

Iulian Nistor, Ph.D., 2006

Dissertation Directed By: Professor of Engineering Isaak D. Mayergoyz,
Electrical and Computer Engineering
Department, and
Dr. Charles Krafft,
Laboratory for Physical Sciences

In the dissertation, the use of magnetic single crystal Bismuth-substituted iron garnet thin-films with giant magneto-optical effect as optical sensors for measuring high frequency (up to 1GHz), low intensity magnetic fields is discussed. The advantages of these sensors are high intrinsic sensitivity and the possibility of tailoring the field range of the sensor. The design of these sensors is based on single crystal epitaxial garnet thin films grown by liquid phase epitaxy method from a flux melt. The garnet thin films are fully characterized using various magnetic and optical techniques. The melt compositions that allow for the growth of films with in-plane magnetization, giant Faraday rotation per unit length, large negative uniaxial anisotropies and small cubic anisotropy are identified. The design of garnet based magnetic field sensors is performed and a noise equivalent magnetic field of $1.5 \mu T / \sqrt{Hz}$ and a signal-to-noise ratio of 68dB are demonstrated.

DEVELOPMENT OF MAGNETIC FIELD SENSORS USING BISMUTH –
SUBSTITUTED GARNETS THIN FILMS WITH IN-PLANE MAGNETIZATION

By

Iulian Nistor

Dissertation submitted to the Faculty of the Graduate School of the
University of Maryland, College Park, in partial fulfillment
of the requirements for the degree of
Doctor of Philosophy
2006

Advisory Committee:
Professor Isaak D. Mayergoyz, Chair
Professor Romel D. Gomez
Professor Julius Goldhar
Professor Howard M. Milchberg
Professor Lourdes Salamanca-Riba

© Copyright by
Iulian Nistor
2006

Dedication

*To my wonderful wife, Mihaela, and to my parents,
for their love and continuous support
during my graduate studies and in the preparation of this work.*

Acknowledgements

It is with great honor and respect that I acknowledge the support of my academic advisor, Professor of Engineering Issak D. Mayergoyz, and of Dr. Charles Krafft, Senior Engineer at the Laboratory for Physical Sciences (LPS). Their continuous support and encouragement during my entire Graduate Research Assistant appointment are greatly appreciated. Prof. Mayergoyz, as well as Dr. Krafft, constitute great examples of excellent educators and accomplished researchers, and I feel very fortunate to have been chosen to work with them.

During the four years when I was involved in the research project at the Laboratory for Physical Sciences, there have been several persons who have generously given of their time and expertise. First, I would like to acknowledge Dr. Rafael Rojas and Dr. Carsten Holthaus whose contributions were essential to the advancement of this project. I would also like to thank our former graduate student, Ms. Deanna Zhang, with whom I worked hard on many interesting and challenging research topics.

I am also in debt to Dr. Eduard Giess (formerly with IBM Research) and Dr. Vincent Fratello (Integrated Photonics) for their helpful assistance and discussions. They were of great help in establishing and improving the growth process of garnets at LPS. Finally, I would like to thank Dr. Phil Picolli for his help with the chemical analysis of our samples.

Table of Contents

Dedication	ii
Acknowledgements	iii
Table of Contents	iv
List of Publications	vi
Chapter 1: Introduction	1
1.1 The aim and organization of the dissertation	1
1.2 Fiber optic sensors – general considerations	4
1.3 Measurement of the magnetic field.....	6
Chapter 2: Garnets – materials, their properties and applications	9
2.1 Garnets materials	9
2.1.1 Faraday Effect.....	11
2.1.2 Density of the magnetic free energy	14
2.2 Magneto-optical properties of bulk magnetic garnet films.....	19
2.3 Magneto-optical properties of thin magnetic garnet waveguides	31
2.4 Magnetic field sensors using garnets	35
Chapter 3: The Growth of epitaxial single crystal garnet thin films	42
3.1 Liquid phase epitaxy growth.....	42
3.2 Garnet Engineering	47
Chapter 4: Characterization of epitaxial single crystal garnet thin films	50
4.1 X-ray measurement of lattice mismatch	50
4.2 Determination of film thickness.....	53
4.3 Magnetic measurements of material properties	54
4.4 Optical measurements of material properties	60
4.4.1 Faraday Rotation.....	62
4.4.2 Magnetostriction constants in (111) – oriented garnets.....	63
4.4.3 Cubic anisotropy constant.....	67
4.5 Influence of melt chemistry and growth conditions on the properties of LPE - grown thin epitaxial garnet films	74

4.5.1 Influence of melt chemistry and undercooling	77
4.5.2 Influence of the substrate rotation (RPM) on single crystal properties	87
Chapter 5: Magnetic field optical sensors based on garnet thin films	94
5.1 Principle of operation of the magneto-optical sensors.....	94
5.2 Design of the optical waveguide and experimental setup.....	98
5.3 Optical sensors based on single layer garnet films	100
5.3.1 Magneto-optical indicators	100
5.3.2 Noise and sensitivity measurements for sensors based on single layer garnet thin films	108
5.4 Optical sensors based on symmetric layer garnet films.....	117
5.4.1 Determination of layer specific magnetic properties in multi-layer garnets	117
5.4.2 Noise and sensitivity measurements for sensors based on multi-layer garnet films	121
5.5 Temperature dependence of sensor films	125
5.6 On-chip integration of magneto-optic field sensors.....	128
Conclusions and Future Work.....	132
Appendix A: Jones Calculus	134
Bibliography	138

List of Publications

1. R. Rojas, C. Krafft, **I. Nistor**, D. Zhang, and I. D. Mayergoyz, "Growth effects (rotation rate) on the characteristics of Bi-substituted lutetium iron garnets", *Journal of Applied Physics* **95** (11), pp. 6885 (2004).
2. **I. Nistor**, C. Krafft, R. Rojas, and I. D. Mayergoyz, "Measurement of the magnetostriction constant of Bi-doped garnets by optical observation of stress-induced stripe domains", *IEEE Transactions on Magnetics* **40** (4), pp. 2832 (2004).
3. **I. Nistor**, C. Krafft, R. Rojas, and I. D. Mayergoyz, "Magneto-optic studies of garnets subject to rotating magnetic fields", *Journal of Applied Physics* **97**, pp. 10R302 (2005).
4. **I. Nistor**, I. D. Mayergoyz, R. Rojas, and C. Krafft, "Optical study of magnetostriction in (Bi, Ga) - substituted garnet thin films", *Journal of Applied Physics* **98**, pp. 073901 (2005).
5. **I. Nistor**, C. Holthaus, C. Krafft, and I. D. Mayergoyz, "Development of LPE-grown (Bi, Gd, Lu)-substituted thin-film iron garnets", *To appear in Journal of Applied Physics* **99**, (2006).
6. C. Holthaus, **I. Nistor**, C. Krafft, and I. D. Mayergoyz, "Magnetic Field Sensors Based on Garnets with In-Plane Magnetization", *To appear in Journal of Applied Physics* **99**, (2006).
7. **I. Nistor**, C. Holthaus, C. Krafft, and I. D. Mayergoyz, "Direct imaging of two-dimensional magnetic patterns with sub-micron resolution using thin garnet films with giant magneto-optical effect", *Submitted for publication in IEEE Transaction on Magnetics*.
8. **I. Nistor**, C. Holthaus, I. D. Mayergoyz, and C. Krafft, "Determination of layer specific magnetization and anisotropy fields in multilayer garnet films from FMR and VSM measurements", *Submitted for publication in IEEE Transaction on Magnetics*.

Chapter 1: Introduction

1.1 The aim and organization of the dissertation

There has always been a growing demand for more sensitive and more reliable magnetic field sensors. The applications of these sensors are in industry and in fundamental research. Almost all of the modern devices are generating higher or lower levels of electromagnetic waves. Security check devices, medical scanners, cell phones, electrical power lines all represent but a few of the sources generating electromagnetic pollution. This pollution has to be controlled in order to reduce electromagnetic interference between electronic devices and even possible health safety concerns. In order to accomplish this control, sensors are required that will reliably measure the magnetic fields.

The electromagnetic interference is why the industry has promoted and supported for a long time the search for sensors that will be immune to the fields they are supposed to measure. Specifically, after the development of optical fibers, the focus was on developing optical remote sensing applications providing immunity to electromagnetic interference, electrical isolation and a number of other advantages. Techniques that do not use electrical currents as measuring principle are desired. These currents induce additional magnetic fields that will affect the real measured value of the field. This is especially important when measuring very small magnetic fields.

The purpose of the dissertation is to analyze the feasibility of magnetic field sensors based on iron garnet materials. These materials have the property that the

polarization plane of linearly polarized light passing through the material is rotated proportional to the applied magnetic field. This effect is called Faraday rotation. In order to guarantee optimal performance, the sensor should have a giant Faraday effect per unit length and in-plane magnetization. Obtaining a material with these properties will enable the development of more sensitive and faster optical magnetic field sensors than those currently available on the market. The potential applications of such optical sensors are numerous and range from medical field and non-destructive testing to current metering and military applications.

Such optical sensors have truly unique features that separate them from their electrical counterparts. Optical sensors built using iron garnets are free of electromagnetic interference, electrically isolated and have an excellent signal to noise and frequency response.

Since such devices are not available on the market, this is a project that starts from scratch. The involved topics are thus very complex and cover, as it will be emphasized in this research, many aspects of engineering including material science, optics and electromagnetics. The project is part of a more comprehensive research aimed at obtaining materials with appropriate properties for magneto-optical indicators and sensors. Since we are growing our own working materials, this research project features a strong material science component.

The materials of choice for this research project are the bismuth, lutetium substituted iron garnet thin films (BiLu)IG. This is because Bi-substituted iron garnets are recognized as optical materials with one of the largest known specific Faraday rotation, on the order of degrees per micrometer. They also have a relatively

low optical attenuation in the near infrared region, where the high data rate optical communication via glass fiber has been developed and many laser sources are readily available at an affordable price.

For sensing applications, a micron thick waveguide-like structure that will be etched in a thin film of garnet material has been studied. The garnet is in the form of a single crystal, required to reduce the material generated noise, and the magnetic state is a single domain to eliminate the magnetic Barkhausen noise due to domain motion. One of the most remarkable properties that justifies research in these garnet-based sensors is that their frequency response shows no decline up to the GHz range.^{1,2} If a functional device is obtained, it is expected to equal or even surpass the sensitivities and frequency range reported in the literature for optical sensors. Along the way, we also expect to develop a full engineering process that will allow us to obtain in controllable and repeatable manner films with desired properties.

The dissertation is structured as follows. First, a short discussion regarding fiber optic sensors and magnetic field sensors is necessary to understand the state of the matters in this field. Then, the most relevant topics pertinent to garnet crystals, their history and applications are presented, along with an in-depth discussion of the Faraday effect in bulk and wave-guide like garnet structures. In Chapter 3 the growth technique used to grow single crystal garnet thin films is discussed, together with major material engineering considerations to control the films properties. Chapter 4 includes a comprehensive description of the material characterization work performed on the single crystal garnet films, as well as a discussion of the influence of different growth conditions (e.g melt chemistry, substrate rotation rate, melt undercooling) on

the material properties. In Chapter 5, sensor design: theory, challenges and practical solutions are discussed in detail. The devices used for demonstrating the proof of principle are described together with measurements of their response as magnetic field sensors. Chapter 5 also includes the presentation of a different type of sensor for magnetic field, used not for measuring the magnetic field, but for imaging fringing magnetic fields of different magnetic patterns. Although not based on a waveguide structure, this imager still qualifies as a garnet based magnetic field sensor. The dissertation ends with conclusions and a short discussion on the future work required to optimize the magnetic field sensors based on single crystal epitaxial garnet thin films.

1.2 Fiber optic sensors – general considerations

A fiber optic sensor consists of an optical sensing element which, under the influence of the quantity to be measured, modulates the light, and optical fibers to guide the light to and from the sensing element. When the sensing element is also an optical fiber, the sensor is *intrinsic*, while if the optical fibers are only used for guidance purposes and the sensing element is external, the sensor is *extrinsic*. In literature, the term fiber optic sensor is sometimes reserved for the intrinsic sensors only.

The progress in this field started with the invention of laser light sources and first optical fibers. The rapid development in the field of optical fibers, shown in Fig. 1.1 has since then made optical and electro-optical components available at reasonable prices. Due to their low loss characteristics and the capacity to be optically interrogated, these components rapidly found use for measurement applications. In

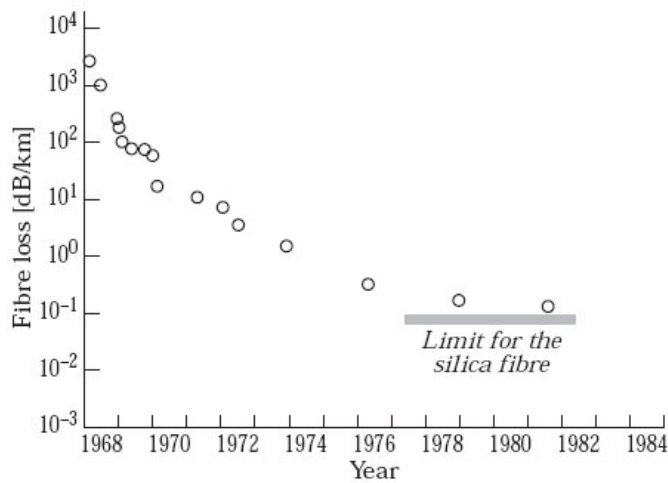


Fig. 1.1 Development roadmap for optical fibers. Due to the low absorption, and possibility to be optically interrogated, sensors based on optical fibers were introduced since the early 1970s.

the first fiber optic sensors that were developed, bundles of optical fibers were used,³ but similar sensors with single fibers soon appeared.⁴ During the early 70's, many of the commonly used sensing principles were developed.^{5,6,7,8,9} Since then, the technological advances of the fiber optic communications research and development have immediately been taken advantage of in the sensor community.

The truly unique features of the fiber optic sensors, *their immunity to electromagnetic interference and their electrical isolation*, were recognized from the very beginning, and scenarios from the seventies indicated a complete switch to optical measurement technologies. After an initial disappointing start, where these sensors did not have high enough reliability levels to be accepted by industry, there has been a renewed interest since the 1990s and the fiber optic sensors are being reintroduced, especially since one of the leading applications areas for these sensors is the electrical power industry.

Similar to the conventional electric sensors, the number of combinations of measurement quantity (intensity, wavelength, phase, or polarization state), sensing principle and output parameter is large. Care has to be exerted when considering that

intensity of the return light is in fact the only parameter that can be measured at the output of any optical system. All other parameters must be converted to intensities at one or more detectors in order to be measured.

For intrinsic sensors, changes in the measurement quantity can be caused by different mechanisms such as:

- intensity sensors: loss mechanisms such as microbending,^{10,11} reflections from gratings in the fiber,¹² temperature dependent scattering,¹³ dopants, and light decoupling;¹⁴
- phase sensors: interferometric sensors;¹⁵
- polarization sensors: photoelastic effects in fibers;^{16,17}

For extrinsic sensors, like those making the object of this dissertation, the following mechanisms can be used for sensing:

- intensity sensors: moving parts,¹⁸ environmentally dependent loss;¹⁹
- wavelength sensors: wavelength dependent loss element;²⁰
- phase sensors: interferometric sensors
- polarization sensors: Faraday effect.²

1.3 Measurement of the magnetic field

Magnetic field measurements are not only made to measure the magnetic field itself, but also to provide indirect information about other quantities, such as electrical currents, rotation speed, acoustic pressure, perturbations of the earth's field due to the presence of a metallic mass such as vehicles, weapons. The ranges of magnetic field encountered in practical applications are different. Measurements of electric currents involve fields exceeding 1T, while detection of small magnetic perturbations requires

detection sensitivities down to 10^{-11} T.^{15,21} The required bandwidths range from milliHertz for vehicle detection to gigaHz for EMC measurements.

The Figure 1.2 shows the most used types of magnetic field sensors. We can see that there are many types of sensing principles, each of them with advantages and disadvantages depending on the case. It can also be concluded that there is no ideal sensor for magnetic field measurements:

SQUIDS – are magnetic field sensors based on superconductive quantum interference effect. They are the most sensitive detectors on the market right now, but their main disadvantage is that they require expensive and bulky setups, because they only work at low temperatures.

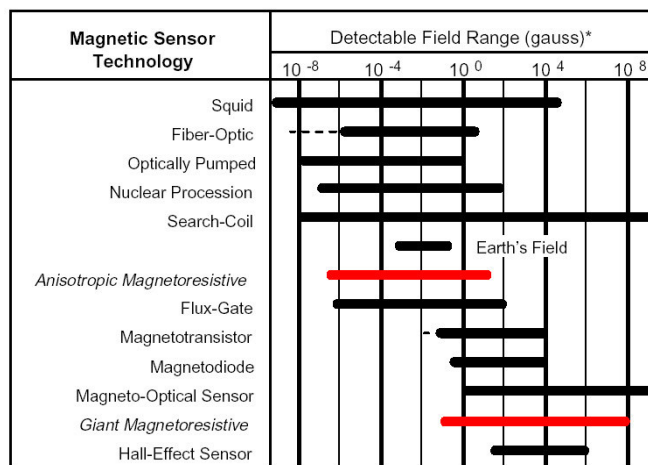


Fig. 1.2 Magnetic field sensors: different types and their sensitivities.

Fiber Optic sensors– are free of electromagnetic interference, but they are bulky due to the low Faraday effect of optical fibers. They can also be directly used as current sensors.

GMR and Hall sensors – are widely used in industry mainly because of their integration capability with semiconductor processing technologies. Being based on

detecting changes in electrical parameters, they do not have good frequency response and are prone to electromagnetic interference.

Magneto-Optical sensors – they are the focus of present work and will be discussed in detail in the following chapters.

Chapter 2: Garnets – materials, their properties and applications

This second chapter presents an overview of garnet materials with emphasis on their applications and their unique non-reciprocal behavior. A thorough theoretical discussion of Faraday effect in both bulk and waveguide devices is included, for a better understanding of the magnetic field sensing action, described later in Chapter 5.

2.1 Garnets materials

Magnetic garnets are cubic crystals having 160 ions per cubic unit cell. The chemical formula of garnets is $\text{RE}_3\text{Fe}_5\text{O}_{12}$, and in terms of crystallographic sites it can be written as $\{c^{3+}\}_3[a^{3+}]_2(d^{3+})_3O_{12}$. There are three different lattice sites for the cations with respect to the surrounding oxygen anions. The dodecahedral $\{c\}$ sites are occupied by rare-earth cations and/or by Y^{3+} , La^{3+} and Bi^{3+} . The octahedral $[a]$ and tetrahedral (d) sites are occupied by iron or iron substituents.

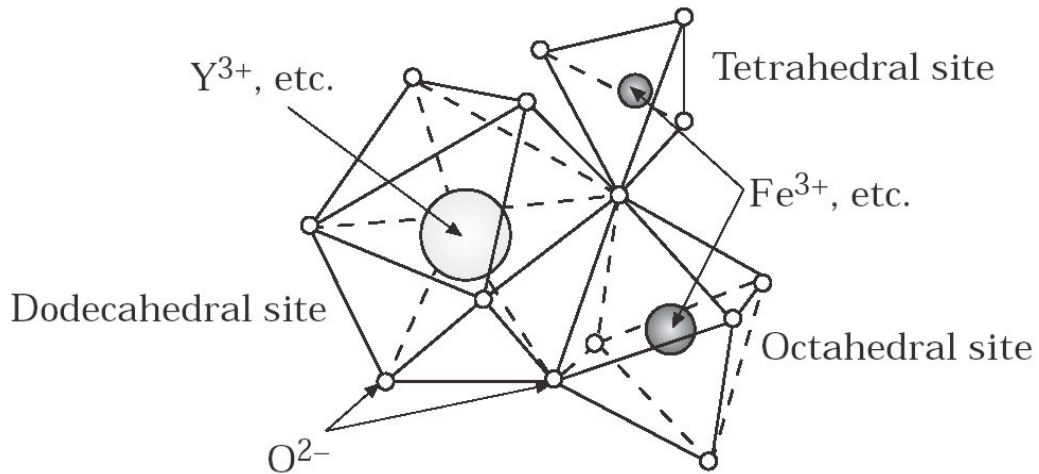


Fig. 2.1 Crystal structure of magnetic garnets.²²

These tetrahedral and octahedral sites are coupled antiferromagnetically. Since they are not equivalent, this coupling yields a ferrimagnetic crystal. The temperature dependent saturation magnetization of the crystal is given by the vector sum of the sublattice magnetizations (see Fig. 2.2):

$$M_s(T) = |\pm M_c(T) + M_a(T) - M_d(T)| \quad (2.1)$$

Without substitution of Fe^{3+} by diamagnetic ions like Ga^{3+} and Al^{3+} the magnetization of the (d) sublattice dominates. The diamagnetic ions are mainly incorporated on tetrahedral sites so that an increasing substitution level will decrease $M_d(T)$ leaving $M_a(T)$ mostly unaltered. At a certain substitution level, both the tetrahedral and octahedral sublattices are equivalent in which case they will compensate each other and the magnetization will be that of the dodecahedral substituting ion.

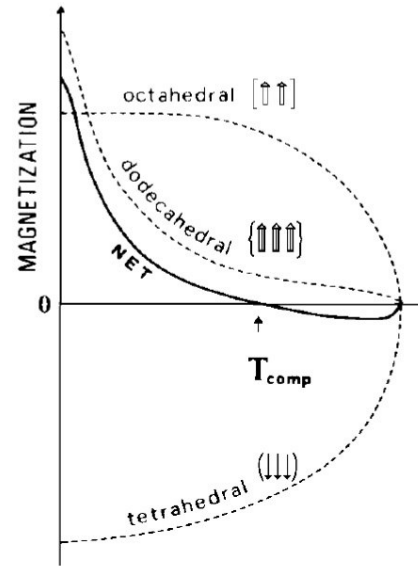


Fig. 2.2 Diagram showing the coupling between magnetization lattices in iron garnets.

Since the sites are strongly coupled through exchange constant, the temperature dependence is less pronounced. This is not the case for the {c} site, where the magnetic ions are weakly coupled and thus the corresponding magnetic moment decays rapidly with the temperature. This is not necessarily a bad thing and we will see its usefulness for our sensor application in Chapter 5.

The dodecahedral sites in garnet crystals can accept substitutions of one or more types of ions and each substitution introduces different changes in the material

properties. Bi^{3+} has been shown to induce a very strong Faraday rotation in the visible range. This combined with the fact that the crystals have low absorption in the visible and IR range makes them by far the most used materials for magneto-optic imaging, optical switches, isolators and modulators.

2.1.1 Faraday Effect

For magneto-optical applications two optical properties are of interest: the magneto-optical activity and the optical absorption. For an incident linearly polarized light beam the magneto-optical activity is defined as the rotation of the polarization plane of the light after passing through the length of the material. It can be shown that any linearly polarized light can be split into right- and left-hand circularly polarized light. In the case of magneto-optic materials, the medium has different refractive indices for these circularly polarized waves. If we want to understand this effect we have to use the fact that the indices of refraction are related to electronic transitions between electronic states. The fact that there is a difference between the left- and right-hand circular indices of refraction means that they have different resonance frequencies. In this subchapter we will see what the quantum mechanical explanation for this difference is and how to relate the microscopic parameters to the Faraday rotation.

In terms of magneto-optical activity it was experimentally observed that the Faraday rotation per unit length increases with increasing Bi concentration. The theoretical models proposed to explain this effect use data from experimental measurements of Faraday effect versus light frequency. The basis is the assumption that the substitution of Bi results in an overlap between the 6p orbital of Bi^{3+} , 2p

orbital of O^{2-} and 3d orbital of Fe^{3+} . This effect is described quantum mechanically as a spin-orbit interaction that induces splitting in the energy levels of the corresponding orbitals (both ground and excited states). There are two situations possible:²³

- *paramagnetic* transition, when only the ground state is split.
- *diamagnetic* transition, when the ground state is a singlet and the excited state is split.

Dionne and Allen questioned whether the paramagnetic transition can account for the Bi contribution since the strong superexchange field excludes Zeeman splitting of the ground state thus leaving a spin singlet ground state.²⁴ There is still some controversy but the generally accepted model involves only the diamagnetic type-transitions.

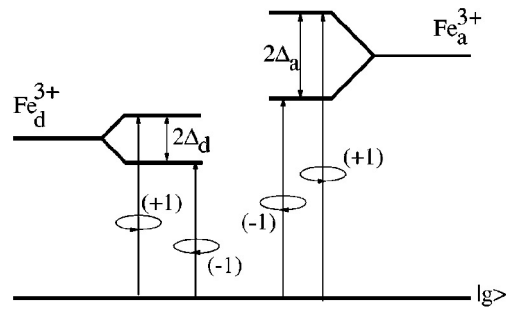


Fig. 2.2 Energy level diagram showing the transitions from the tetrahedral and octahedral sites associated with the Faraday effect. (from [23])

In this case there is a way to theoretically calculate the magneto-optic response which then can be compared to experimental data.^{23,25,26,27} This response has to be linked to the microscopic parameters (energy splitting level, and so on). This is usually accomplished through the complex permittivity tensor, which can be written as:

$$\boldsymbol{\varepsilon} = \begin{pmatrix} \varepsilon_0 & j\varepsilon_1 & 0 \\ -j\varepsilon_1 & \varepsilon_0 & 0 \\ 0 & 0 & \varepsilon_0 \end{pmatrix}, \quad (2.2)$$

where $\varepsilon_1 = \varepsilon'_1 + j\varepsilon''_1$ represents the magneto-optical response and ε_0 the nonmagneto-optical part. As it will be shown in Chapter 2, using this expression for the dielectric tensor, in the visible region the Faraday rotation can be expressed as:

$$\theta_F = \frac{\omega}{2nc} \varepsilon'_1, \quad (2.3)$$

where ω is the frequency, c the speed of light and n the index of refraction.

In order to relate the components of the permittivity tensor to microscopic quantities, Dionne and Allen showed that if the transitions are assumed of electric dipole nature, the theoretical expression for the Faraday rotation is ^{23,24}:

$$\theta_F = \frac{\pi e^2 \omega^2}{nmc} \sum_{i=a,d} \left\{ \frac{Nf_i}{\omega_i} \left[\frac{(\omega_i + \Delta_i)^2 - \omega^2 - \Gamma_i^2}{\left((\omega_i + \Delta_i)^2 - \omega^2 + \Gamma_i^2 \right)^2 + 4\omega^2 \Gamma_i^2} - \frac{(\omega_i - \Delta_i)^2 - \omega^2 - \Gamma_i^2}{\left((\omega_i - \Delta_i)^2 - \omega^2 + \Gamma_i^2 \right)^2 + 4\omega^2 \Gamma_i^2} \right] \right\} \quad (2.4)$$

The sum is over the optical transition in the tetrahedral and octahedral sublattices, $\omega_{i+} = (\omega_i + \Delta_i)$ and $\omega_{i-} = (\omega_i - \Delta_i)$ represent the resonant frequencies for right- and left-hand circular polarized transitions, f_i is the oscillator strength, Γ_i is the half-linewidth of the transitions, e and m are the electron charge and mass, respectively, and N is the active ion density (to first order assumed directly proportional to the Bi content). Due to the large number of ions involved, the resonator strength parameters are not easily accessible and usually are treated as adjustable parameters in the comparison with experimental data.

Since there are no electric dipole transitions for the corresponding photon energies of the IR region where the garnets are transparent, the Faraday effect is due to magnetic dipole transitions. It has been shown experimentally that in the IR range,

this effect does not change with the frequency like in the case of visible light and is at least one order of magnitude smaller than for the visible case. The reason for this is that the gyromagnetic effect is determined by the off diagonal terms of the permeability tensor $\hat{\mu}_r$. These components are caused by the precession of the magnetization vector under the influence of the magnetic field of the propagating electromagnetic wave:²⁸

$$\theta_F = \frac{\pi\omega n}{c}(\mu_- - \mu_+) = \frac{g\pi e M_s}{mc^2}, \quad (2.5)$$

where g is the gyromagnetic factor and M_s is the saturation magnetization.

As for the optical absorption, the essential contributions are due to the incorporation of lead and platinum in the epitaxial film. Since the crystal has to be electrically neutral, the Pb^{2+} , Pb^{4+} , Pt^{2+} and Pt^{4+} ions induce the formation of Fe^{2+} and Fe^{4+} ions. These ions have a strong optical absorption through the charge transfer mechanism. As has been shown by Hergt *et al.*²⁹ the lead and platinum content increases strongly with the undercooling and by this increase the absorption constant of the layer. In order to reduce the optical absorption it is therefore desired to substitute the garnet with ions of valence 2+, other than Fe. Some examples include Mg^{2+} , Ca^{2+} . For our proposed IR sensor, the optical absorption is very low for our level of impurities thus we are not looking into reducing this effect by other substitutions.

2.1.2 Density of the magnetic free energy

As it will be more clearly explained in the next subchapters, the Faraday rotation depends on the component of the magnetization parallel to the propagation direction

of the light in the material. For sensing applications, when the optical signal is related to the magnetic field, it is important to understand the effect of the magnetic field on the magnetization equilibrium position. For this purpose, a short discussion about the magnetic free energy is required.

In magnetic materials, the equilibrium position of the magnetization \vec{M} is described using a quantity called magnetic free energy that includes the effect of external and internal magnetic fields on the magnetization. The equilibrium position is obtained by minimizing this free energy density.

In order to mathematically express this quantity, we will use the following coordinate system (see Fig. 2.3). The direction of \vec{M} is defined by the polar angle θ and the azimuthal angle φ . Similarly, the direction of the magnetic field is defined by the polar angle θ_H and azimuth φ_H .

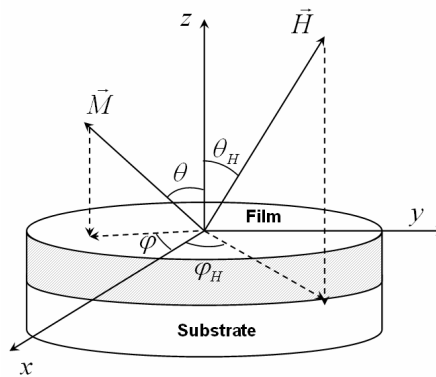


Fig. 2.3 The spherical coordinate system used to express the free energy density.

The magnetic free energy is composed of the following terms:

- **Zeeman energy** - describes the interaction between the external applied magnetic field and the magnetization vector. It has the form $f_{Zeeman} = -\vec{M} \cdot \vec{H}$. The equilibrium position of the magnetization is parallel to the applied external field.
- **Demagnetizing energy** – in magnetic materials, the presence of magnetic charges on the surface induces a divergence of the magnetization. In homogeneously magnetized ellipsoids, the demagnetizing field can be described in terms of the

demagnetizing tensor $\vec{H}_{dem} = -\hat{N}\vec{M}$, where $\hat{N} = \begin{pmatrix} N_x & 0 & 0 \\ 0 & N_y & 0 \\ 0 & 0 & N_z \end{pmatrix}$ in the principal

axis system of the ellipsoid and the components are related by $N_x + N_y + N_z = 4\pi$.

For thin, disk like films, only N_z is non zero, thus the demagnetizing field is $\vec{H}_{dem} = -N_z M_z \hat{z} = -N_z M \cos \theta \hat{z}$. From here the demagnetizing energy can be

expressed as $f_{demag} = -\frac{1}{2} \vec{M} \cdot \vec{H}_{demag} = 2\pi M^2 \cos^2 \theta$. From the demagnetizing

energy point of view, the position of equilibrium for the magnetization is $\theta = \pi/2$ which means that the magnetization lies in the plane of the thin film.

- **Exchange energy** – this interaction is a quantum mechanical effect and is due to the overlapping of the electron wave functions. The expression for this energy is

$$f_{ex} = -\sum_{i \neq j} A_{ij} \vec{S}_i \cdot \vec{S}_j$$

where A_{ij} is the overlap integral of the electron wave functions

(or the *exchange constant*). The equilibrium described by this equation is a state in which all the spins are parallel.

- **Cubic anisotropy energy** – it is also a quantum mechanical effect based on the interaction of the electron spin with the orbital angular momentum. For a cubic crystal, this energy term can be expressed as a power series of the direction cosines of the magnetization with respect to the <100>-directions:³⁰

$$f_{cubic} = K_1(\alpha_1^2\alpha_2^2 + \alpha_2^2\alpha_3^2 + \alpha_3^2\alpha_1^2) + K_2\alpha_1^2\alpha_2^2\alpha_3^2 + \dots$$

For garnet materials $K_2 \approx 0$ and $K_1 < 0$, thus the easy axes will be aligned with the <111> directions.

- **Stress-induced anisotropy** – is due to magnetoelastic interactions that relate mechanical stresses in the films to changes in magnetization direction. Phenomenologically, for cubic crystal the stress-induced term can be written as:

$$f_{me} = -\frac{3}{2}\sigma\lambda_{100}(\alpha_1^2\gamma_1^2 + \alpha_2^2\gamma_2^2 + \alpha_3^2\gamma_3^2) - 3\sigma\lambda_{111}(\alpha_1\alpha_2\gamma_1\gamma_2 + \alpha_2\alpha_3\gamma_2\gamma_3 + \alpha_3\alpha_1\gamma_3\gamma_1),$$

where $\lambda_{100}, \lambda_{111}$ are the magnetostriction constants, α_i are the direction cosines of the magnetization and γ_i are the direction cosines of the magnetization.³¹

For the case of (100) and (111) oriented films it can be shown that

$$f_{me} = -\frac{3}{2}\sigma\lambda_{100}\sin^2\theta \text{ and } f_{me} = -\frac{3}{2}\sigma\lambda_{111}\sin^2\theta \text{ respectively.}$$

If following the growth process, there is a mismatch (Δa_{\perp}) between the lattice of the substrate (a_s) and that of the epitaxial film, the stress-induced energy density can be expressed depending on the crystallographic orientation of the substrate as:

$$f_{me} = -\frac{3}{2}\frac{E}{1+\nu}\left(\frac{\Delta a_{\perp}}{a_s}\right)\lambda_{100}\sin^2\theta, \text{ or } f_{me} = -\frac{3}{2}\frac{E}{1+\nu}\left(\frac{\Delta a_{\perp}}{a_s}\right)\lambda_{111}\sin^2\theta,$$

where $E = 2.05 \cdot 10^{11} \text{ N/m}^2$ is the Young's modulus and $\nu = 0.296$ is the Poisson ratio.³² This indicates that the effect of the stress-induced anisotropy is equivalent to a magnetic uniaxial anisotropy term K_u^λ .

- **Growth-induced anisotropy** – the primary mechanism producing growth anisotropy in crystalline garnet films is the preferential ordering of rare earth ions on certain lattice sites depending on the growth orientation and the identity of ions. It can be proved that for (100) or (111) oriented substrates, the growth-induced anisotropy K_u^g gives a $\sin^2 \theta$ contribution to the free energy density (similar with the stress-induced anisotropy).

The stress- and growth-induced anisotropies are the sources of the total uniaxial anisotropy term $K_u = K_u^\lambda + K_u^g$. The free energy corresponding to this uniaxial term is given by $f_{uniax} = K_u \sin^2 \theta$. We can immediately see that in order to obtain films with in-plane magnetization we need to have $K_u < 0$. As in most cases with garnet materials there is a trade-off: increasing the Bi substitution increases the Faraday rotation but makes $K_u > 0$ which is exactly the opposite of what we need for sensing applications. The melt chemistry, growth conditions and lattice matching play an important role here and identifying the right parameters is a topic that we are actively pursuing. A more detailed discussion regarding the effect of these growth parameters on the material magnetic anisotropies is included in Chapter 4.

By adding all these energy densities we obtain the total free energy density:

$$f = f_{Zeeman} + f_{demag} + f_{ex} + f_{uniax} + f_{cubic} \quad (2.6)$$

The anisotropy energy and the demagnetizing energy are responsible for the formation of magnetic domains in the materials. The transition between the magnetic domains is not abrupt, because of the exchange energy that creates domain walls.

If the sample is assumed to be in a uniform state, the equilibrium position of the magnetization is given by the following system of equations:

$$\frac{\partial f}{\partial \theta} = \frac{\partial f}{\partial \varphi} = 0, \quad \frac{\partial^2 f}{\partial \theta^2} > 0, \quad \frac{\partial^2 f}{\partial \varphi^2} > 0. \quad (2.7)$$

2.2 Magneto-optical properties of bulk magnetic garnet films

The theoretical analysis of the magneto-optical effects is accomplished as follows. First it is assumed that the medium is an unbounded isotropic dielectric material. Then the magneto-optic properties are introduced by defining the permittivity not as a number but as a tensor. This tensor results from adding a diagonal part corresponding to the isotropic dielectric with an off-diagonal tensor representing the magnetization effects:

$$\hat{\epsilon}_r = \hat{\epsilon}_r^{iso} + \Delta \hat{\epsilon}(\vec{M}), \quad (2.8)$$

where we neglected the stress and growth induced optical anisotropies since in the first approximations they can be considered small perturbations. These off-diagonal terms lead to nonreciprocal mode conversion and nonreciprocal phase shifts.

The isotropic part is related to the complex index of refraction $N_0 = n_0 - j \frac{\alpha_0}{2k_0}$

by:

$$\hat{\boldsymbol{\epsilon}}_r^{iso} = \begin{pmatrix} N_0^2 & 0 & 0 \\ 0 & N_0^2 & 0 \\ 0 & 0 & N_0^2 \end{pmatrix} \quad (2.9).$$

In Eq. (2.9), n_0 is the isotropic index of refraction, α_0 is the absorption coefficient and $k_0 = \frac{2\pi}{\lambda} = \frac{\omega}{c} = \omega\sqrt{\epsilon\mu_0}$ is the free space wave number.

The magnetization dependent part $\Delta\hat{\boldsymbol{\epsilon}}(\vec{M})$ can be written as a power series in the components of the magnetization as:³³

$$\Delta\boldsymbol{\epsilon}_{ij}(\vec{M}) = \sum_{k=1}^3 K_{ijk} M_k + \sum_k \sum_l G_{ijkl} M_k M_l \quad (2.10).$$

G_{ijkl} are the components of the quadratic magneto-optical tensor and give rise to the reciprocal effect called Cotton-Mouton effect which is usually much smaller than the linear effects. This quadratic tensor will be neglected in the rest of the theoretical treatment.

The components of the permittivity tensor have to fulfill the Onsager relations³⁴ $\boldsymbol{\epsilon}_{ij}(\vec{M}) = \boldsymbol{\epsilon}_{ji}(-\vec{M})$ and due to crystal symmetry it follows:

$K_{123} = K_{231} = K_{312} = -K_{213} = -K_{321} = -K_{132} = K = K' + iK''$. All other components vanish. The final permittivity tensor that we will use in our model is thus:

$$\hat{\boldsymbol{\epsilon}}_r = \begin{pmatrix} N_0^2 & KM_3 & -KM_2 \\ -KM_3 & N_0^2 & KM_1 \\ KM_2 & -KM_1 & N_0^2 \end{pmatrix} = \begin{pmatrix} \boldsymbol{\epsilon}_{11} & \boldsymbol{\epsilon}_{12} & -\boldsymbol{\epsilon}_{31} \\ -\boldsymbol{\epsilon}_{12} & \boldsymbol{\epsilon}_{22} & \boldsymbol{\epsilon}_{23} \\ \boldsymbol{\epsilon}_{31} & -\boldsymbol{\epsilon}_{23} & \boldsymbol{\epsilon}_{33} \end{pmatrix} \quad (2.11).$$

The Maxwell equations are:

$$\begin{aligned}
\vec{\nabla} \times \vec{E} &= -\frac{\partial \vec{B}}{\partial t} & \vec{\nabla} \cdot \vec{B} &= 0 \\
\vec{\nabla} \cdot \vec{D} &= \rho & \vec{\nabla} \times \vec{H} &= \vec{j} + \frac{\partial \vec{D}}{\partial t}
\end{aligned} \tag{2.12}$$

where \vec{E} is the electric field, \vec{H} is the magnetic field, \vec{D} is the electric displacement, \vec{B} the magnetic flux, ρ the density of free electric charge and \vec{j} the free current density. We also have the constitutive material equations:

$$\begin{aligned}
\vec{B} &= \mu_0(\vec{H} + \vec{M}) = \mu_0 \hat{\mu}_r \vec{H} \\
\vec{D} &= \epsilon_0 \vec{E} + \vec{P} = \epsilon_0 \hat{\epsilon}_r \vec{E}
\end{aligned} \tag{2.13}$$

where $\hat{\mu}_r, \hat{\epsilon}_r$ are the magnetic permeability and electric permittivity tensors respectively.

Since the ferromagnetic resonance absorption peak for these materials is located in the gigahertz range, it means that at frequencies corresponding to visible-near IR electromagnetic waves (terahertz), the permeability tensor $\hat{\mu}_r$ can be considered equal to unity.

Eq. (2.12) combined with the fact that garnets are insulator materials ($\vec{j} = 0$) yields:

$$\vec{\nabla} \times (\vec{\nabla} \times \vec{E}) = -\vec{\nabla} \times \frac{\partial \vec{B}}{\partial t} = -\mu_0 \frac{\partial}{\partial t} (\vec{\nabla} \times \vec{H}) = -\mu_0 \epsilon_0 \hat{\epsilon}_r \frac{\partial^2 \vec{E}}{\partial t^2} \tag{2.14}$$

The wave propagation equation is then:

$$\vec{\nabla} (\vec{\nabla} \cdot \vec{E}) - (\nabla^2) \vec{E} + \mu_0 \epsilon_0 \hat{\epsilon}_r \frac{\partial^2 \vec{E}}{\partial t^2} = 0 \tag{2.15}$$

$$\text{If the media is unbounded then } \vec{E} = \vec{E}_0 e^{j(\omega t - \vec{k} \cdot \vec{z})} \tag{2.16},$$

and we have:

$$\begin{aligned}
\vec{\nabla} \cdot \vec{E} &= \frac{\partial E_x}{\partial x} + \frac{\partial E_y}{\partial y} + \frac{\partial E_z}{\partial z} = \frac{\partial}{\partial x} E_{0x} e^{j(\alpha x - k_x x - k_y y - k_z z)} + \frac{\partial}{\partial y} E_{0y} e^{j(\alpha x - k_x x - k_y y - k_z z)} + \frac{\partial}{\partial z} E_{0z} e^{j(\alpha x - k_x x - k_y y - k_z z)} = \\
&= -jk_x E_x - jk_y E_y - jk_z E_z = -j\vec{k} \cdot \vec{E} \\
\text{Next } \vec{\nabla}(\vec{\nabla} \cdot \vec{E}) &= -j \left[\frac{\partial(\vec{k} \cdot \vec{E})}{\partial x} \hat{x} + \frac{\partial(\vec{k} \cdot \vec{E})}{\partial y} \hat{y} + \frac{\partial(\vec{k} \cdot \vec{E})}{\partial z} \hat{z} \right] \tag{2.17}.
\end{aligned}$$

Since they are similar let us look closely at just one term from the above equation:

$$\begin{aligned}
\frac{\partial(\vec{k} \cdot \vec{E})}{\partial x} &= \frac{\partial}{\partial x} (k_x E_x + k_y E_y + k_z E_z) = -jk_x^2 E_x - jk_x k_y E_y - jk_x k_z E_z = \\
&= -jk_x (k_x E_x + k_y E_y + k_z E_z) = -jk_x (\vec{k} \cdot \vec{E}) \tag{2.18}
\end{aligned}$$

Using Eq. (2.18), Eq. (2.17) becomes

$$\vec{\nabla}(\vec{\nabla} \cdot \vec{E}) = -\vec{k}(\vec{k} \cdot \vec{E}) \tag{2.19}.$$

The second term of Eq. (2.15) is:

$$(\nabla^2) \vec{E} = \frac{\partial^2 \vec{E}}{\partial x^2} + \frac{\partial^2 \vec{E}}{\partial y^2} + \frac{\partial^2 \vec{E}}{\partial z^2} = -(k_x^2 + k_y^2 + k_z^2) \vec{E} = -\vec{k}^2 \vec{E} \tag{2.20}.$$

Using Eq. (2.16) the third term of Eq. (2.15) can be written as:

$$\mu_0 \epsilon_0 \hat{\epsilon}_r \frac{\partial^2}{\partial t^2} \vec{E} = \mu_0 \epsilon_0 \hat{\epsilon}_r \vec{E}_0 \frac{\partial^2}{\partial t^2} e^{j(\alpha - \vec{k} \cdot \vec{r})} = -\mu_0 \epsilon_0 \hat{\epsilon}_r \omega^2 \vec{E} \tag{2.21}$$

Substituting Eqs. (2.19), (2.20) and (2.21) in Eq. (3.8) we obtain the wave equation:

$$\vec{k}(\vec{k} \cdot \vec{E}) - (k^2) \vec{E} + k_0^2 \hat{\epsilon}_r \vec{E} = 0 \tag{2.22},$$

with k_0 defined above.

This is an eigenvalues and eigenmodes problem. The eigenvalues are obtained so that we will have nontrivial solutions for the electric field, i.e. when the determinant of the coefficients vanishes:

$$\det \left[k^2 \delta_{ij} - k_i k_j - k_0^2 \epsilon_{ij}(\omega, \vec{M}) \right] = 0 \tag{2.23}$$

Substituting the \vec{k} values into Eq. (2.22) one can determine the eigenvectors of each mode. This is the algorithm used in this dissertation.

Assume for simplicity that the wave vector of the propagating plane wave is $\vec{k} = (0,0,k)$. Then Eq. (2.23) yields:

$$\begin{vmatrix} \varepsilon_{11} - (k/k_0)^2 & \varepsilon_{12} & -\varepsilon_{31} \\ -\varepsilon_{12} & \varepsilon_{22} - (k/k_0)^2 & \varepsilon_{23} \\ \varepsilon_{31} & -\varepsilon_{23} & \varepsilon_{33} \end{vmatrix} = 0 \Leftrightarrow \quad (2.24)$$

$$(k'^2 - \varepsilon_{11})(k'^2 - \varepsilon_{22})\varepsilon_{33} + \varepsilon_{31}^2(\varepsilon_{22} - k'^2) + \varepsilon_{23}^2(\varepsilon_{11} - k'^2) + \varepsilon_{33}\varepsilon_{12}^2 = 0$$

where $\vec{k}' = \vec{k}/k_0$.

Two solutions for k are obtained:

$$k_{1,2} = k_0 \sqrt{\frac{\varepsilon_{33}\varepsilon_{22} + \varepsilon_{33}\varepsilon_{11} + \varepsilon_{23}^2 \pm \sqrt{\varepsilon_{33}^2\varepsilon_{22}^2 - 2\varepsilon_{33}^2\varepsilon_{22}\varepsilon_{11} + 2\varepsilon_{23}^2\varepsilon_{22}\varepsilon_{33} + \varepsilon_{11}^2\varepsilon_{33}^2 - 2\varepsilon_{33}\varepsilon_{11}\varepsilon_{23}^2 + \varepsilon_{23}^4 - 4\varepsilon_{33}^2\varepsilon_{12}^2}}{2\varepsilon_{33}}} \quad (2.25)$$

Since we have two possible solutions for the wave vector, it means that we will obtain two propagating eigenmodes.

We will look at the simple case of a propagating plane wave perpendicular to the film surface, with the magnetization of the material parallel to the (xz)-plane:

$$\vec{M} = M_s (\sin \theta, 0, \cos \theta), \quad (2.26)$$

the dielectric tensor $\hat{\varepsilon}$ can be written as:

$$\hat{\varepsilon}_r = \begin{pmatrix} \varepsilon_{11} & \varepsilon_{12} & -\varepsilon_{31} \\ -\varepsilon_{12} & \varepsilon_{22} & \varepsilon_{23} \\ \varepsilon_{31} & -\varepsilon_{23} & \varepsilon_{33} \end{pmatrix} = \begin{pmatrix} N_0^2 & KM_s \cos \theta & 0 \\ -KM_s \cos \theta & N_0^2 & KM_s \sin \theta \\ 0 & -KM_s \sin \theta & N_0^2 \end{pmatrix} \quad (2.27).$$

With this, the solutions for k are:

$$k_{1,2} = k_0 N_{1,2}, \quad (2.28)$$

$$\text{where } N_{1,2} = \sqrt{N_0^2 + \frac{(KM_s)^2 \sin^2 \theta}{2N_0^2} \pm j(KM_s) \sqrt{\cos^2 \theta - \frac{(KM_s)^2 \sin^4 \theta}{4N_0^4}}} \quad (2.29).$$

For $N_{1,2}$ the respective eigenmodes follow from Eq. (2.22):

$$\begin{aligned} (N_0^2 - N_{1,2}^2)E_{0x} + KM_s \cos \theta \cdot E_{0y} &= 0 \\ -KM_s \cos \theta \cdot E_{0x} + (N_0^2 - N_{1,2}^2)E_{0y} + KM_s \sin \theta \cdot E_{0z} &= 0 \\ -KM_s \sin \theta \cdot E_{0y} + N_0^2 E_{0z} &= 0 \end{aligned} \quad (2.30)$$

Thus we have:

$$\vec{E}_1 = E_0 \begin{pmatrix} 1 \\ \frac{(N_0^2 - N_1^2)}{KM_s \cos \theta} \\ \frac{(N_0^2 - N_1^2) \tan \theta}{N_0^2} \end{pmatrix} e^{j(\alpha x - k_1 z)} \quad \text{and} \quad \vec{E}_2 = E_0 \begin{pmatrix} \frac{KM_s \cos \theta}{(N_2^2 - N_0^2)} \\ 1 \\ \frac{KM_s \sin \theta}{N_0^2} \end{pmatrix} e^{j(\alpha x - k_2 z)} \quad (2.31)$$

The peculiar form of the eigenmodes was chosen for reasons that will become clear later in the demonstration. Eqs. (2.30) and (2.31) can be used to numerically analyze the propagation of a planar wave through an unbounded gyrotropic media.

At $z=0$, the eigenmodes are:³⁵

$$\begin{aligned} \vec{E}_1 &= E_0 \begin{pmatrix} 1 \\ \frac{(N_0^2 - N_1^2)}{KM_s \cos \theta} \\ \frac{(N_0^2 - N_1^2) \tan \theta}{N_0^2} \end{pmatrix} e^{j\alpha x} = E_0 \begin{pmatrix} E_x^{(1)} \\ E_y^{(1)} \\ E_z^{(1)} \end{pmatrix} e^{j\alpha x}, \\ \vec{E}_2 &= E_0 \begin{pmatrix} \frac{KM_s \cos \theta}{(N_2^2 - N_0^2)} \\ 1 \\ \frac{KM_s \sin \theta}{N_0^2} \end{pmatrix} e^{j\alpha x} = E_0 \begin{pmatrix} E_x^{(2)} \\ E_y^{(2)} \\ E_z^{(2)} \end{pmatrix} e^{j\alpha x} \end{aligned} \quad (2.32)$$

Usually in magneto-optics we are dealing with linearly polarized waves at the input and analyze the output using an analyzer. This means that in our case with \vec{k} along the z-direction, we can use the eigenmodes to express the incoming wave (linearly polarized under an angle β) as:

$$\vec{E}_{in} = E_0 \left(A \vec{E}^{(1)} + B \vec{E}^{(2)} \right) e^{j\alpha x} \quad (2.33)$$

$$\text{with } A = \frac{\cos \beta - \sin \beta \cdot E_x^{(2)}}{1 - E_y^{(1)} E_x^{(2)}} \text{ and } B = \frac{\sin \beta - \cos \beta \cdot E_y^{(1)}}{1 - E_y^{(1)} E_x^{(2)}} \quad (2.34)$$

After transmitting through a magneto-optic medium of thickness d , the emerging light wave is obtained as the composition of the two eigenmodes at $z = d$:

$$\vec{E}_{out} = E_0 \left(A \vec{E}^{(1)} e^{j(\alpha x - k_1 d)} + B \vec{E}^{(2)} e^{j(\alpha x - k_2 d)} \right) \quad (2.35)$$

Case I. The magnetization makes a small angle with respect to the light propagation direction

In order to obtain useful analytical solutions, we have to use some approximations. For a wide range of angles, usually $0 \leq \theta \leq 45^\circ$ the following approximation is valid:

$|KM_s| \sin^2 \theta \ll 2N_0^2 |\cos \theta|$, thus the terms with $\sin^2 \theta, \sin^4 \theta$ in Eq. (2.29) can be neglected. This yields for the two k solutions:

$$k_{1,2} = k_0 \sqrt{N_0^2 + \pm j(KM_s) \cos \theta} \approx k_0 N_0 \left(1 \pm j \frac{KM_s}{2N_0^2} \cos \theta \right) = k_0 N_0 \pm j k_0 \frac{(KM_s) \bar{N}_0}{2|N_0^2|} \cos \theta. \quad (2.36)$$

This means that the two propagating modes have different indices of refraction. In order to find their expression we are using the fact that $K = K' + jK''$ and

$N_0 = n_0 - j \frac{\alpha_0}{2k_0}$; thus Eq. (2.36) can be separated into a real and an imaginary part as

shown below:

$$\begin{aligned} (k_{1,2})_{real} &= k_0 n_0 \mp k_0 \frac{n_0 K'' M_s + \frac{\alpha_0}{2k_0} K' M_s}{2|N_0|^2} \cos \theta = k_0 n^\pm \\ (k_{1,2})_{img} &= k_0 \left(\frac{\alpha_0}{2k_0} \mp \frac{n_0 K' M_s - \frac{\alpha_0}{2k_0} K'' M_s}{2|N_0|^2} \cos \theta \right) = \frac{\alpha^\pm}{2} \end{aligned} \quad (2.37)$$

Also using Eq. (2.36) the eigenmodes can be expressed as:

$$\vec{E}^+ = E_0 \begin{pmatrix} 1 \\ j \\ 0 \end{pmatrix} e^{j(\alpha - k_0 n^+ z) - \alpha^+ z/2} \text{ and } \vec{E}^- = E_0 \begin{pmatrix} j \\ 1 \\ \frac{KM_s}{N_0^2} \sin \theta \end{pmatrix} e^{j(\alpha - k_0 n^- z) - \alpha^- z/2} \quad (2.38)$$

These modes correspond to right and left circularly polarized (with a small longitudinal component) plane waves, propagating along z-direction with different indices of refraction given by Eq. (2.37):

$$N^\pm = n^\pm - j \frac{\alpha^\pm}{2k_0} \quad (2.39)$$

According to Eqs. (2.33), (2.34), and (2.35) the propagating wave at the output is:

$$\begin{aligned}
\vec{E}_{out} &= \frac{1}{2}(\cos \beta - j \sin \beta) \vec{E}^+(d) + \frac{1}{2}(\sin \beta - j \cos \beta) \vec{E}^-(d) = \\
&= \frac{1}{2} e^{-j\beta} \vec{E}^+(d) + \frac{1}{2} e^{j\left(\beta - \frac{\pi}{2}\right)} \vec{E}^-(d) = \\
&= E_0 \left(\frac{1}{2} e^{-j\beta} e^{j(\alpha - k_0 n^+ d) - \alpha^+ d/2} + \frac{1}{2} j e^{j\left(\beta - \frac{\pi}{2}\right)} e^{j(\alpha - k_0 n^- d) - \alpha^- d/2} \right) = \\
&= E_0 \left(\frac{1}{2} j e^{-j\beta} e^{j(\alpha - k_0 n^+ d) - \alpha^+ d/2} + \frac{1}{2} e^{j\left(\beta - \frac{\pi}{2}\right)} e^{j(\alpha - k_0 n^- d) - \alpha^- d/2} \right) = \\
&= E_0 e^{j\left(\alpha - k_0 \frac{n^+ + n^-}{2} d\right)} e^{-\frac{\alpha^+ + \alpha^-}{4} d} \left(\frac{1}{2} e^{-j\left(\beta + k_0 \frac{n^+ - n^-}{2} d\right)} e^{-\frac{\alpha^+ - \alpha^-}{4} d} + \frac{1}{2} e^{j\left(\beta + k_0 \frac{n^+ - n^-}{2} d\right)} e^{\frac{\alpha^+ - \alpha^-}{4} d} \right) = \\
&= E_0 e^{j\left(\alpha - k_0 \frac{n^+ + n^-}{2} d\right)} e^{-\frac{\alpha^+ + \alpha^-}{4} d} \left(\frac{1}{2} j e^{-j\left(\beta + k_0 \frac{n^+ - n^-}{2} d\right)} e^{-\frac{\alpha^+ - \alpha^-}{4} d} - \frac{1}{2} j e^{j\left(\beta + k_0 \frac{n^+ - n^-}{2} d\right)} e^{\frac{\alpha^+ - \alpha^-}{4} d} \right) = \\
&= E \left(\cos\left(\beta + k_0 \frac{n^+ - n^-}{2} d\right) \frac{e^{-\frac{\alpha^+ - \alpha^-}{4} d} + e^{\frac{\alpha^+ - \alpha^-}{4} d}}{2} + j \sin\left(\beta + k_0 \frac{n^+ - n^-}{2} d\right) \frac{e^{\frac{\alpha^+ - \alpha^-}{4} d} - e^{-\frac{\alpha^+ - \alpha^-}{4} d}}{2} \right) = \\
&= E \left(\sin\left(\beta + k_0 \frac{n^+ - n^-}{2} d\right) \frac{e^{-\frac{\alpha^+ - \alpha^-}{4} d} + e^{\frac{\alpha^+ - \alpha^-}{4} d}}{2} - j \cos\left(\beta + k_0 \frac{n^+ - n^-}{2} d\right) \frac{e^{\frac{\alpha^+ - \alpha^-}{4} d} - e^{-\frac{\alpha^+ - \alpha^-}{4} d}}{2} \right) = \\
&= E \left(\cos\left(\beta + k_0 \frac{n^+ - n^-}{2} d\right) \cosh\left(\frac{\alpha^+ - \alpha^-}{4} d\right) + j \sin\left(\beta + k_0 \frac{n^+ - n^-}{2} d\right) \sinh\left(\frac{\alpha^+ - \alpha^-}{4} d\right) \right) \\
&= E \left(\sin\left(\beta + k_0 \frac{n^+ - n^-}{2} d\right) \cosh\left(\frac{\alpha^+ - \alpha^-}{4} d\right) - j \cos\left(\beta + k_0 \frac{n^+ - n^-}{2} d\right) \sinh\left(\frac{\alpha^+ - \alpha^-}{4} d\right) \right)
\end{aligned}$$

$$\text{where } E = E_0 e^{j(\alpha - k_0 n_0 d)} e^{-\frac{\alpha_0}{2} d} \quad (2.40)$$

We can see that if there is no difference between the absorption coefficients for the

$$\text{two eigenmodes, } \vec{E}_{out} = E_0 e^{j(\alpha - k_0 n_0 d)} e^{-\frac{\alpha_0}{2} d} \begin{pmatrix} \cos\left(\beta + k_0 \frac{n^+ - n^-}{2} d\right) \\ \sin\left(\beta + k_0 \frac{n^+ - n^-}{2} d\right) \end{pmatrix} \quad (2.41)$$

that describes a linearly polarized wave with the polarization plane rotated with an angle:

$$\theta_F = k_0 \frac{n^+ - n^-}{2} d = -k_0 \frac{n_0 K'' M_s + \frac{\alpha_0}{2k_0} K' M_s}{2|N_0|^2} \cos \theta \cdot d = \theta_{\max} \cos \theta \cdot d \quad (2.42).$$

This is the Faraday rotation also known as magnetic circular birefringence (**MCB**).

In general, the two propagating eigenmodes have different absorption coefficients, thus Eq. (2.40) shows that even if the incident wave is linearly polarized, the output is an elliptical polarized wave with the main axis rotated by the Faraday angle and ellipticity related to:

$$\phi = \frac{\alpha^+ - \alpha^-}{4} d = -k_0 \frac{n_0 K' M_s - \frac{\alpha_0}{2k_0} K'' M_s}{2|N_0|^2} \cos \theta \cdot d = \phi_{\max} \cos \theta \cdot d \quad (2.43)$$

This effect is called magnetic circular dichroism (**MCD**). The Faraday ellipticity is related to the angle ϕ by:

$$\tan \Psi_F = \tanh(\phi_{\max} \cos \theta \cdot d) \quad (2.44)$$

Case II. The magnetization is perpendicular to the light propagation direction

In this case $\theta = \frac{\pi}{2}$ therefore the propagation constants given by Eqs. (2.28) and (2.29)

are:

$$k_1^2 = k_0^2 N_0^2, k_2^2 = k_0^2 \left(N_0^2 + \frac{(KM_s)^2}{N_0^2} \right) \quad (2.45)$$

The eigenmodes given by Eqs. (3.23) and (3.24) are:

$$\vec{E}_1 = E_0 \begin{pmatrix} 1 \\ 0 \\ 0 \end{pmatrix} e^{j(\alpha x - k_1 z)} \quad \text{and} \quad \vec{E}_2 = E_0 \begin{pmatrix} 0 \\ 1 \\ \frac{KM_s}{N_0^2} \end{pmatrix} e^{j(\alpha x - k_2 z)} \quad (2.46)$$

The eigenmodes are linearly polarized waves, one parallel to \vec{M} and the other one perpendicular to \vec{M} . We see that \vec{E}_2 has a longitudinal component but this is not taken into account because in optical measurements we only detect the electric field components perpendicular to the propagation direction.

According to Eqs. (2.33), (2.34), and (2.35) the propagating wave at the output is:

$$\begin{aligned} \vec{E}_{out} &= \cos \beta \vec{E}_1(d) + \sin \beta \vec{E}_2(d) = \\ &= E_0 \begin{pmatrix} \cos \beta e^{j(\alpha x - k_1 d)} \\ \sin \beta e^{j(\alpha x - k_2 d)} \end{pmatrix} = E_0 e^{j(\alpha x - k_1 d)} \begin{pmatrix} \cos \beta \\ \sin \beta e^{j(k_1 - k_2)d} \end{pmatrix} \end{aligned} \quad (2.47)$$

Let us simplify the expression in Eq. (2.47). From Eq. (2.45) we have:

$$\begin{aligned} k_1 &= k_0 N_0 = k_0 n_0 - j \frac{\alpha_0}{2} \\ k_2 &= k_0 \sqrt{N_0^2 + \frac{(KM_s)^2}{N_0^2}} \approx k_0 N_0 \left(1 + \frac{(KM_s)^2}{2N_0^4} \right) = k_0 N_0 + k_0 \frac{(KM_s)^2}{2N_0^3} = k_0 N_0 + k_0 \frac{(KM_s)^2 \bar{N}_0^3}{2|N_0|^6} \end{aligned} \quad (2.48)$$

Since $N_0 = n_0 - j \frac{\alpha_0}{2k_0}$, we get:

$$N_0^3 = \left(n_0^3 - 3n_0 \frac{\alpha_0^2}{4k_0^2} \right) - j \left(3n_0^2 \frac{\alpha_0}{2k_0} - \frac{\alpha_0^3}{8k_0^3} \right) \quad (2.49)$$

Typical values for garnets are $\alpha_0 = 2000 \text{ cm}^{-1}$ and $\lambda = 628 \text{ nm}$ thus

$k_0 = \frac{2\pi}{\lambda} = 10^5 \text{ cm}^{-1}$ which yields $\frac{\alpha_0}{2k_0} \approx 10^{-4}$. This is much smaller than the value of

n_0 which is around 2.3 for visible light, which means that in Eq. (2.49) we can neglect all the terms that contain absorption. Then Eq. (2.48) can be rewritten as:

$$\begin{aligned} k_1 &= k_0 N_0 = k_0 n_0 - j \frac{\alpha_0}{2} \\ k_2 &= k_0 N_0 + k_0 \frac{(K' M_s)^2 - (K'' M_s)^2}{2n_0^3} + 2jk_0 \frac{(K' M_s)(K'' M_s)}{2n_0^3} = k_0 N_0 + k_0 \Delta n + j \Delta \alpha \end{aligned} \quad (2.50),$$

$$\text{where } \Delta n = \frac{(K' M_s)^2 - (K'' M_s)^2}{2n_0^3} \text{ and } \Delta \alpha = 2k_0 \frac{(K' M_s)(K'' M_s)}{2n_0^3} \quad (2.51).$$

By replacing the expression for k 's in Eq. (2.47) we obtain:

$$\vec{E}_{out} = E_0 e^{j(\alpha - k_0 n_0 d)} e^{-\frac{\alpha_0 d}{2}} \begin{pmatrix} \cos \beta \\ \sin \beta \cdot e^{\frac{\Delta \alpha d}{2}} e^{-jk_0 \Delta n d} \end{pmatrix} \quad (2.52)$$

In this case the situation is the reverse of case I. The difference in the refractive indices will change the ellipticity of the polarized wave:

$$\Psi_{LMB} = -\sin(2\beta) \cdot d \cdot k_0 \frac{(K' M_s)^2 - (K'' M_s)^2}{4n_0^3}, \quad (2.53)$$

where LMB stands for linearly magnetic birefringence.

In the same time due to different absorption coefficients the main axis of the ellipse will rotate by an angle

$$\Theta_{LMD} = \sin(2\beta) \cdot d \cdot k_0 \frac{(K' M_s)(K'' M_s)}{2n_0^3}, \quad (2.54)$$

which describes the linear magnetic dichroism effect.

These linear effects are generally much smaller than the circular ones discussed in case I. They also depend on M_s^2 thus they are reciprocal, which means that they cancel in the reflection geometry.

2.3 Magneto-optical properties of thin magnetic garnet waveguides

Here it is only intended to give a brief account of the coupling mode theory and to develop the formalism that will help us understand the Faraday effect in waveguides. The theory of coupled and normal modes is mathematically difficult and there is still no general demonstration of some of its more important results, such as the completeness principle, except in the case of the simplest geometries.

The principle of completeness is the most important result of the normal modes theory. In bidirectional waveguides, it states that the fields of any propagating wave can be expressed as a linear combination of transverse electric (or magnetic) fields of the forward-traveling waves. These expansions are the basis of the perturbation theory for electromagnetic systems that are close to an ideal waveguide. The components of the exact complete field are expressed using the normal modes of the system as:

$$\begin{aligned}\vec{E}(x, y, z, t) &= \sum_k A_k(z) \frac{1}{\sqrt{P_k}} \vec{e}_k(x, y) e^{j\alpha z} \\ \vec{H}(x, y, z, t) &= \sum_k A_k(z) \frac{1}{\sqrt{P_k}} \vec{h}_k(x, y) e^{j\alpha z}\end{aligned}, \quad (2.55)$$

where in the case of the unperturbed waveguide, the amplitudes $A_k(z) = A_k e^{-j\beta z}$ vary harmonically with the propagation distance z . P_k , the power of mode k is generally normalized to unity. As it will be shown next, for the case of perturbed systems, the above problem is then transformed into a set of differential equations for the expansion coefficients.^{36, 37}

The notations \vec{e}_k, \vec{h}_k represent the electric and magnetic fields of the unperturbed waveguide modes, without the $e^{j(\alpha z - \beta z)}$ dependence. In accordance with the Maxwell

equations the unperturbed mode fields can be chosen to have the form $\vec{e}_k = (E_{kx} \ E_{ky} \ jE_{kz})$, $\vec{h}_k = (H_{kx} \ H_{ky} \ jH_{kz})$ with real field components. For modes propagating in the same direction and for the special case of lossless waveguides, the orthogonality relation is:³⁸

$$\iint (\vec{H}_k \times \vec{E}_i^* - \vec{E}_k \times \vec{H}_i^*)_z dx dy = 4\delta_{ki} P_k. \quad (2.56)$$

Assuming that the guided fields in the perturbed waveguide can be expanded in terms of the modes of the unperturbed guide, the superposition above remains valid but the coefficients $A_k(z)$ are no longer of the simple harmonic dependence with z .

Using $\hat{\epsilon}_k$ for the unperturbed dielectric tensor and $\hat{\epsilon}$ for the perturbed one, the Maxwell equations can be written as:

$$\begin{aligned} \nabla \times \vec{E}_k^* &= j\omega\mu_0 \vec{H}_k^* & \nabla \times \vec{E} &= -j\omega\mu_0 \vec{H} \\ \nabla \times \vec{H}_k^* &= -j\omega\epsilon_0 \hat{\epsilon}_k^* \vec{E}_k^* & \nabla \times \vec{H} &= j\omega\epsilon_0 \hat{\epsilon} \vec{E} \end{aligned} \quad (2.57)$$

From here we obtain:

$$\begin{aligned} \vec{E}_k^* \cdot (\nabla \times \vec{H}) - \vec{H} \cdot (\nabla \times \vec{E}_k^*) &= j\omega\epsilon_0 \vec{E}_k^* \cdot \hat{\epsilon} \vec{E} - j\omega\mu_0 \vec{H} \cdot \vec{H}_k^* \\ \vec{H}_k^* \cdot (\nabla \times \vec{E}) - \vec{E} \cdot (\nabla \times \vec{H}_k^*) &= j\omega\epsilon_0 \vec{E} \cdot \hat{\epsilon}_k^* \vec{E}_k^* - j\omega\mu_0 \vec{H}_k^* \cdot \vec{H} \end{aligned} \quad (2.58)$$

Subtracting the terms in Eq. (2.58) and using the identity $\nabla \cdot (\vec{a} \times \vec{b}) = \vec{b} \cdot (\nabla \times \vec{a}) - \vec{a} \cdot (\nabla \times \vec{b})$, the following reciprocity relation can be derived:

$$\nabla \cdot (\vec{H} \times \vec{E}_k^* - \vec{E} \times \vec{H}_k^*) = j\omega\epsilon_0 \vec{E}_k^* \cdot (\hat{\epsilon} - \hat{\epsilon}_k^*) \vec{E} = j\omega\epsilon_0 \vec{E}_k^* \cdot \Delta \hat{\epsilon} \vec{E} \quad (2.59)$$

where \vec{E}_k and \vec{H}_k denote mode fields with the time and space dependence $e^{j(\alpha x - \beta_k z)}$.

We can easily see that for the unperturbed case $\Delta\hat{\epsilon}=0$ and the above equation reduces to $\nabla \cdot (\vec{H}_k \times \vec{E}_i^* - \vec{E}_k \times \vec{H}_i^*) = 0$ from which the orthogonality condition is obtained (by integrating over the x-y plane):^{39, 40}

$$(\beta_k - \beta_i) \iint (\vec{H}_k \times \vec{E}_i^* - \vec{E}_k \times \vec{H}_i^*)_z dx dy = 0. \quad (2.60)$$

An important consequence of the orthogonality relation is that the power carried by a waveguide is equal to the sum of the powers carried by each mode.

Now returning to the case of the perturbed waveguide, by integration over x-y plane, and use of Eq. (2.59) we obtain:

$$\begin{aligned} & \iint \nabla \cdot (\vec{H} \times \vec{E}_i^* - \vec{E} \times \vec{H}_i^*) dx dy = \\ & = \iint \nabla_t \cdot (\vec{H} \times \vec{E}_i^* - \vec{E} \times \vec{H}_i^*) dx dy + \hat{z} \cdot \iint \frac{\partial}{\partial z} (\vec{H} \times \vec{E}_i^* - \vec{E} \times \vec{H}_i^*) dx dy = \quad (2.61) \\ & = \iint (j\omega\epsilon_0 \vec{E}_i^* \Delta\hat{\epsilon} \vec{E}) dx dy \end{aligned}$$

Using the expansion expressions for the electric and magnetic fields and the orthogonality relation for the unperturbed modes we obtain:

$$\iint \nabla_t \cdot (\vec{H} \times \vec{E}_i^* - \vec{E} \times \vec{H}_i^*) dx dy = \sum_k A_k(z) e^{j\beta_i z} \cdot \iint \nabla_t \cdot (\vec{h}_k \times \vec{e}_i^* - \vec{e}_k \times \vec{h}_i^*) dx dy = 0 \quad (2.62)$$

The second term of Eq. (2.61) becomes:

$$\begin{aligned} & \iint \frac{\partial}{\partial z} (\vec{H} \times \vec{E}_i^* - \vec{E} \times \vec{H}_i^*) dx dy = \sum_k \iint \frac{\partial}{\partial z} [A_k(z) \cdot e^{j\beta_i z} (\vec{h}_k \times \vec{e}_i^* - \vec{e}_k \times \vec{h}_i^*)] dx dy = \\ & = \sum_k \frac{\partial A_k(z)}{\partial z} e^{j\beta_i z} \iint (\vec{h}_k \times \vec{e}_i^* - \vec{e}_k \times \vec{h}_i^*) dx dy + \sum_k j\beta_i A_k(z) e^{j\beta_i z} \iint (\vec{h}_k \times \vec{e}_i^* - \vec{e}_k \times \vec{h}_i^*) dx dy + \\ & + \sum_k A_k(z) e^{j\beta_i z} \iint \frac{\partial}{\partial z} (\vec{h}_k \times \vec{e}_i^* - \vec{e}_k \times \vec{h}_i^*) dx dy = e^{j\beta_i z} \cdot \sum_k \left(\frac{\partial A_k(z)}{\partial z} + j\beta_i A_k(z) \right) \cdot \iint (\vec{h}_k \times \vec{e}_i^* - \vec{e}_k \times \vec{h}_i^*) dx dy \quad (2.63) \end{aligned}$$

Now using the orthogonality relation for the modes in Eq. (2.60) yields:

$$\hat{z} \cdot \iint \frac{\partial}{\partial z} (\vec{H} \times \vec{E}_i^* - \vec{E} \times \vec{H}_i^*) dx dy = 4 \left[\frac{\partial A_i(z)}{\partial z} + j\beta_i A_i(z) \right] e^{j\beta_i z} \quad (2.64)$$

Using Eqs. (2.61) and (2.64) the mode coupling equations for the amplitudes are:^{38,41}

$$\partial_z A_i(z) = -j\beta_i A_i(z) - j \sum_k \kappa_{ik} A_k(z). \quad (2.65)$$

The coupling coefficients are given by (for power of the modes normalized to 1):

$$\kappa_{ik} = \frac{\omega \epsilon_0}{4} \iint \vec{e}_i^* (\Delta \hat{\epsilon}) \vec{e}_k dx dy \quad (2.66)$$

Up to this point this discussion was for a general waveguide, but now we will focus on a system closer related to our proposed dielectric slab geometry. In the general case of dielectric waveguides, we don't have pure TE and TM modes, but hybrid modes, for which neither E_z nor H_z are zero. Dielectric slab structures represent an important exception because this system is uniform along two different axes, y and z –axis (propagation direction). In this case, for isotropic materials we can express the y- independent modes as either TE or TM fields.³⁸

- **TE** modes: E_z , E_x , and H_y are zero
- **TM** modes: H_z , H_x and E_y are zero.

For such a waveguide, as it will be shown in Chapter 5, we can control the number of modes above the cut-off frequency. In the simple case when only the fundamental TE and TM modes are guided, the coupled mode equations reduce to:

$$\begin{aligned} \partial_z A_{TE} &= -j\beta'_{TE} A_{TE} - j\kappa^* A_{TM} \\ \partial_z A_{TM} &= -j\beta'_{TM} A_{TM} - j\kappa A_{TE} \end{aligned} \quad (2.67)$$

$$\text{with } \beta'_{TE} = \beta_{TE} + \kappa_{TE,TE}, \beta'_{TM} = \beta_{TM} + \kappa_{TM,TM}, \kappa = \kappa_{TM,TE}. \quad (2.68)$$

By solving this system of equations we obtain the following equation that can be used to calculate the amplitudes of the TE and TM modes as a function of the propagation distance if the initial amplitudes are given:⁴²

$$\begin{pmatrix} A_{TM}(z) \\ A_{TE}(z) \end{pmatrix} = e^{j\frac{\beta'_{TE} + \beta'_{TM}}{2}z} \cdot \begin{pmatrix} \cos \Gamma z - j\frac{\Delta\beta'}{2\Gamma} \sin \Gamma z & -j\kappa \frac{\sin \Gamma z}{\Gamma} \\ -j\kappa^* \frac{\sin \Gamma z}{\Gamma} & \cos \Gamma z + j\frac{\Delta\beta'}{2\Gamma} \sin \Gamma z \end{pmatrix} \begin{pmatrix} A_{TM}(0) \\ A_{TE}(0) \end{pmatrix} \quad (2.69)$$

where $\Delta\beta' = \beta'_{TM} - \beta'_{TE}$ and $\Gamma = \sqrt{|\kappa|^2 + (\Delta\beta'/2)^2}$.

Assuming that the propagation starts with a purely TE polarized wave, the relative power associated with the TM polarized mode after propagating through the length L of the waveguide is given by:^{41,42}

$$\frac{|A^{TM}(L)|^2}{|A^{TM}(L)|^2 + |A^{TE}(L)|^2} = \frac{|\kappa|^2}{|\kappa|^2 + (\Delta\beta'/2)^2} \sin^2 \left(L\sqrt{|\kappa|^2 + (\Delta\beta'/2)^2} \right) \quad (2.70)$$

It can be seen immediately that in order to couple an appreciable amount of power between the modes, the phase shift $\Delta\beta' = \beta'_{TM} - \beta'_{TE}$ has to be much smaller than the Faraday rotation (that is related to κ). Since this is difficult to accomplish, a complete mode conversion is sometimes difficult to obtain which limits the use of waveguides with longitudinal magnetization in isolator applications. For our sensing application, this effect is expected to have less of an influence than for isolator applications.

2.4 Magnetic field sensors using garnets

There are currently many applications involving garnets of different chemical compositions. Their use is widely spread in microwaves filters and oscillators (they have a very narrow linewidth) and optics (isolators, lasers and modulators).⁴³ These

applications use garnets in the bulk form or in the form of thin films. Recently more exotic applications have been proposed based on uni- and bi-dimensional magneto-phonic garnet structures.^{44,45}

Initially, most of the applications envisaged for garnets were in magneto-optic recording using magnetic bubbles technology. A great deal of the literature that we currently have about garnets and their behavior comes from studies performed in this field. The growth conditions, the dependence of various properties like optical absorption, lattice constants, magnetization, with growth conditions and chemical substitution were extensively investigated.⁴⁶

With the advent of high temperature superconductivity there was a new field in which garnets are used successfully. This is imaging of the high temperature superconductors, a very important technique that proved instrumental in understanding and studying the flux pinning effects.⁴⁷

In optics, the applications were motivated by the discovery of the Faraday enhancement effect with bismuth substitution. Currently, at the near infrared wavelengths, used in optical glass fiber communications, garnets are the only materials discussed for the realization of nonreciprocal devices like isolators, because they combine high magneto-optical effects with low optical losses.

More recently, with the revival of interest in optical sensing methods, garnets were the materials of choice for magnetic field measuring. Magnetic field measurements are required not only to provide the value of the magnetic field itself, but because there is a lot of indirect information that can be extracted. The ranges of magnetic fields encountered are very different. For example the measurement of

electrical current may involve fields exceeding 1T, while detecting perturbations of the earth's magnetic field due to presence of objects like submarines, weapons, requires sensitivities that approach 10^{-11} T.⁴⁸

In terms of measuring the electrical current, it may seem like an easy task to do and surprising to find that there is strong interest in non-electrical measuring methods for high voltage power systems. The reason is that the measurements are complicated by the power dissipation in the measurement circuit and the need to keep the sensor at ground potential.

As mentioned before, the research in the field of optical sensors for magnetic fields started in the 1970s using either the Faraday rotation or magnetostriction in optical fibers. The first elements used bulk optical glass elements in open or closed path configurations. Since the Verdet constant of these materials is low, multiple reflections were investigated to reduce the physical size of the sensing element without reducing the optical path.^{49,50}

The advent of optical fibers solved some of the problems with the bulk materials. Although the Verdet constant of glass is still low, a measurable rotation can be obtained from a long fiber wound around the conductor.

The alternative solution was to use compact sensing elements made from materials with high Faraday rotation. Initially YIG was identified as being a good candidate because it has a Faraday rotation of about $200^\circ/\text{cm}$ in the IR range. In the early 1990s it was shown that with flux grown garnet single crystals a field sensitivity of $100 \text{ pT}/\sqrt{\text{Hz}}$ at 500 Hz might be achieved. This value was enhanced by Deeter *et al.*⁵¹ up to $1 \text{ pT}/\sqrt{\text{Hz}}$ by using ferrite field concentrators. One of the most remarkable

properties that justifies researching these garnet-based sensors is that the frequency response shows no decline up to the gigahertz range.¹

Then it was discovered that the addition of Bi can greatly enhance this effect. Although the material was there, the path to a viable sensor was not easy. The proof is the volume of pertinent literature published especially in the '80s and '90s. BiLuIG might have a strong rotation but incorporating Bi induces changes in the material properties that inadvertently affect the potential applications as sensors. One of these examples is the fact that Bi incorporation tends to increase the growth induced anisotropy thus yielding samples with out-of-plane magnetization.

That is why most of the previous research on magnetic field sensors focused on perpendicularly magnetized films, in which magnetic stripe domains are present. The light is sent through the material perpendicular to the film surface and coupled in a fiber or analyzed directly using a polarizer-analyzer setup. When the magnetic field is strong enough to magnetically saturate the film in one direction, there are no magnetic domains and the Faraday rotation has the maximum value. As the field decreases, the stripe pattern starts to emerge and the presence of regions in which the magnetization is oriented opposite to the light propagation direction reduces the value of the Faraday rotation. These changes can be easily correlated to the value of the magnetic field, thus yielding a method for measuring external magnetic fields. The described behavior is easily observed in the sequence of images in Fig. 2.4. to 2.6, obtained using an in-house (BiLu)IG sample grown on (111) oriented substrate and a polarized microscope.

A downside of this method is that the periodic structure of stripe domains induces diffraction of the incoming light beam which in turn induces nonlinearities in the response, depending on which order is detected. Improved linearity has been demonstrated using a lensing scheme that collects and detects light in orders up to and including ± 2 .⁵² A second downside is that in order to obtain a reasonable Faraday rotation effect, the films have to be thick - on the order of hundreds of microns. This requirement introduces additional difficulties in the growth process in terms of melt depletion and film uniformity.

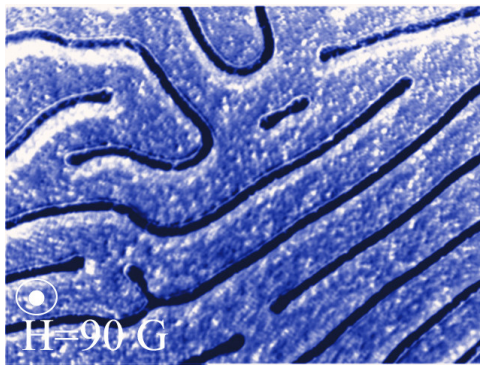


Fig. 2.4 Under a perpendicular magnetic field pointing out-of-page, the magnetic domains are expanded or contracted according to the direction of the magnetization.

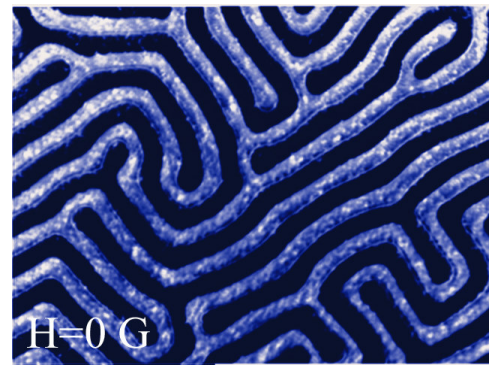


Fig. 2.5 Magnetic domain structure in the absence of any external fields.

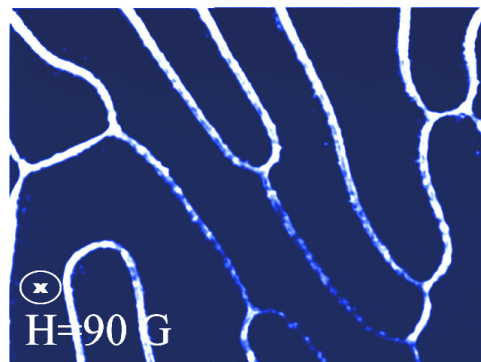


Fig. 2.6 The magnetic domains with magnetization pointing in the page are expanded.



Fig. 2.7 For sensors with out-of-plane magnetization, the stripe structure diffracts the incident light inducing nonlinear response.

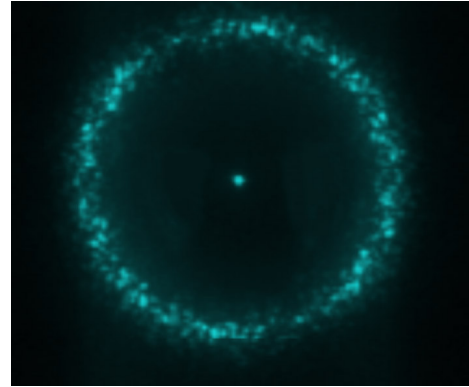


Fig. 2.8 Diffraction pattern of linearly polarized light passing through a material with domain structure as in Fig. 2.7.

Moreover, the melt compositions and growth conditions used for thin $(\text{BiLu})_3(\text{FeGa})_5\text{O}_{12}$ magneto-optic films with negative growth-induced anisotropy are unsuitable for growth of thick films. This is because the growth of films with desired properties from these melts requires high undercoolings and high growth rates that result in poor stability of the melt against homogeneous nucleation.^{53,54,55}

As we can see from this review of the literature, the idea is there, the methods to obtain good quality waveguides are there, measurement setups and techniques are common ground, but what prevented the construction of a viable sensor? The main reason is the lack of garnet thin films with **both** high Faraday rotation per unit length and in-plane magnetization (which yields samples free of magnetic domains). This is because these requirements are normally mutually exclusive: a higher Faraday rotation means more Bi, but more Bi induces a positive uniaxial anisotropy that favors the out-of-plane magnetization orientation. Ways around this problem were suggested in terms of using materials with weaker magneto-optical activity and placing them inside an optical resonator. The light beams will be reflected so many times that the actual path length will more than compensate for the low Faraday rotation per unit length. The problem that we see with these approaches is a

fundamental one. Due to material related noise (the random thermal motion of the magnetization, scattering of light on crystalline volume and surface defects) every round trip that you do in the material will increase the noise level. And this is not about the signal-to-noise ratio, but about the fact that the accumulated level of noise might become larger than the actual signal that you want to measure. Consequently the sensitivity of the sensor will decrease, and this will reduce the performance of the sensor. That is why we strongly believe that the optimum solution is a **single pass** through the magneto-optic material! This is the main reason for which we are actively investigating ways to grow thin epitaxial films with negative induced anisotropy and high Bi incorporation.

As mentioned above, limitation of the field sensitivity of a magneto-optical sensing device using garnet films is given by different noise contributions. The most important noise sources are the optical noise originating in the illumination system, electronic noise due to detection system, and the media noise due to magneto-optical garnet film. The latter one may principally originate from magnetization processes involving domain motion, from the thermally-induced random precession of the magnetization vector around the equilibrium position, from film defects, and from surface roughness. Through the use of the LPE method for film growth, we were able to obtain high quality single crystal films, thus reducing the noise coming from film defects and surface roughness.

Chapter 3: The Growth of epitaxial single crystal garnet thin films

3.1 Liquid phase epitaxy growth

The yttrium iron garnet melts incongruently at 1555°C which means that it is not directly obtainable from its melt by the Czochralski method. Alternative growth methods had to be developed. One of them is liquid phase epitaxy (LPE) growth from a solution that uses lead-oxide (PbO) as a solvent. These solutions can be saturated without spontaneous nucleation occurring.

The LPE process for the deposition of garnet layers is relatively well characterized, easy to handle, low cost and ready for mass production. The layers of garnet materials are grown on substrates that have to meet certain criteria in terms of lattice constant and optical transparency. Fortunately the flexibility of gadolinium gallium garnet (GGG) to substitutions allowed for a wide range of available substrates that meet these criteria. The regular GGG substrates have a lattice constant of 1.2383 nm which agrees well with the lattice constant of pure YIG (1.2374 nm). If larger ions like bismuth or praseodymium have to be incorporated in the epitaxial film, GGG can be substituted during the Czochralski growth process with ions like calcium, magnesium and zirconium, offering a range of possible lattice constants between 1.2382 nm and 1.2511 nm.⁵⁶

For this dissertation, LPE growth has been the method of choice for garnet deposition because the LPE method yields layers with highest crystalline quality and high deposition rates on the order of $\mu\text{m}/\text{min}$. The possibility of precisely controlling

the material properties of the samples was another reason to choose LPE over other techniques. This method being based on thermodynamic equilibrium, it is not possible to obtain a bismuth substitution level that surpasses two formula units. In order to reach Bi incorporation levels larger than 2 formula units, methods working far from equilibrium have to be used such as chemical vapor deposition (CVD), pulsed laser ablation deposition (PLAD) and rf-sputtering.⁵⁷ Since the Bi^{3+} cation has a large radius, its incorporation into the garnet structure leads to an expansion of the lattice, and the material also becomes thermodynamically unstable at high bismuth concentrations.⁵⁸ Thus pure bismuth iron garnets (BIG) cannot be grown using LPE, and only methods working far from the thermodynamic equilibrium can yield pure BIG layers.⁵⁹

The melt is basically a mixture of different oxides, in ratios computed to give us the desired growth composition. After weighing and thoroughly mixing the oxides, the platinum crucible is filled and placed in the furnace. We use a lead oxide-boron oxide mixture as solvent in platinum crucibles under ambient atmosphere. As mentioned above, it is not possible to grow iron garnets using the Czochralski method thus other melts other than $\text{Fe}_2\text{O}_3\text{-Y}_2\text{O}_3$ have to be used.⁶⁰ Alternative fluxes have been proposed, but the advantage of lead-based flux is the moderate growth temperature which is around 1000°C . Basically the lead acts like a solvent allowing the growth of iron garnets at reasonable low temperatures.

The melt consists of a mixture of solvent (PbO and Bi_2O_3), the garnet phase (Fe_2O_3), rare earths (Lu_2O_3 , Gd_2O_3) and a complexing agent used to insure melt

stability at high undercoolings (B_2O_3). Usually when designing a melt, the following cation ratios are used based on:⁶¹

$$\begin{aligned} \frac{G}{F} &= \frac{\sum \text{RareEarth} + Ga_2O_3 / Al_2O_3 + Fe_2O_3}{PbO + B_2O_3 + Bi_2O_3} \\ C_{Bi} &= \frac{Bi_2O_3}{PbO + Bi_2O_3} \\ C_B &= \frac{B_2O_3}{PbO + Bi_2O_3} \\ \frac{Fe}{Ga + Al} &= \frac{Fe_2O_3}{Ga_2O_3 + Al_2O_3} \end{aligned} \quad (3.1)$$

where the above quantities are expressed in cation concentrations. The effects of these parameters on melt characteristics are resumed in the Table III.1.

Table III.1 The melt compositions are characterized by cation ratios. [61] They can be chosen in order to yield samples with desired properties.

Parameter	Effect
G/F	<ul style="list-style-type: none"> Controls the saturation temperature of the melt and the growth rate
C_{Bi}	<ul style="list-style-type: none"> Controls the Bi incorporation in the epitaxial film
C_B	<ul style="list-style-type: none"> Stabilizes the melt allowing for larger undercoolings Reduces the saturation temperature Controls the melt viscosity
$Fe/(Ga + Al)$	<ul style="list-style-type: none"> The higher this ratio is, the lower the diamagnetic substitution thus $4\pi M_s$ increases

The melt is placed in a platinum crucible in a resistive heated five-zone furnace. The diagram of the LPE growth system developed at the Laboratory of Physical Sciences is shown in Fig. 3.1. An image of the actual LPE growth furnace together with the adjacent control panel is presented in Fig. 3.2.

The melt is then homogenized by heating the furnace at a temperature well above the melting point of the oxide mixture (900-950°C) for several hours (overnight) and by stirring with a platinum paddle.

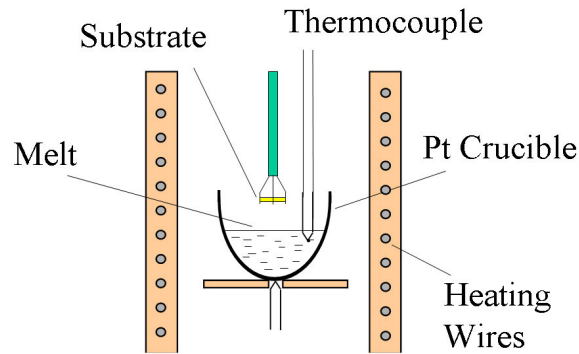


Fig. 3.1 Schematic of the LPE growth furnace. During the growth process, the substrate is horizontally dipped and rotated in the melt and the undercooling is measured with the thermocouple.

For the growth process, a 500 μm thick GGG crystal with crystallographic orientations [100] or [111], is used as a substrate. In order to prevent cracks and other crystalline defects in the films, the substrate has to be matched to the expected lattice parameter of the crystal to be grown. We used either GGG with $a_s = 1.2383\text{nm}$ or substituted GGG substrates with a lattice constant $a_s = 1.2497\text{nm}$.

The substrate is carefully cleaned by etching in hot phosphoric acid to remove any impurities from its surface, and then horizontally placed into the substrate holder. The temperature of the furnace is then lowered until the desired undercooling is reached. The solution is allowed to establish isothermal conditions. After this, the substrate is

lowered in the furnace and kept close to the melt surface. This is done because growing the film on a cold substrate induces transition layers which destroy the desired uniformity of the film. After this waiting period, the substrate is immersed in the undercooled solution, totally or partially, yielding either a one-sided or two-sided film. The sample can be rotated axially. The effect of this rotation rate on the material properties of the films has been studied and reported by our group, and will be discussed in Chapter 4.



Fig. 3.2 Photograph of the LPE growth furnace and adjacent control panel. Labview software is interfaced to the control panel to coordinate the growth process.

After a certain growth time which is usually chosen depending on the thickness that has to be achieved (usually between 2-10 min), the substrate is removed from the solution. In order to remove the melt remnants from the film surface we perform either spinning of the substrate at very high speeds (above 400 RPM) just above the

solution surface, or slowly removing the sample from the melt while tilting the furnace. In the first case the remnants are removed by the centripetal force and this is why this technique works better for large diameter substrates. In the latter case, if the sample is slowly removed from the melt, the liquid film on the substrate won't break into small drops and the adhesion forces from the melt surface will retain it thus yielding a cleaner film. The sample can then be chemically cleaned using a heated solution of nitric acid, acetic acid and water. After the deposition process the solution is homogenized again for several hours before the next growth process takes place.

3.2 Garnet Engineering

One of the most important parameters in the selection of the rare-earth used in the melt is the anisotropy induced by the pairing between the rare-earth and the bismuth. Studies have shown that the amount of growth-induced anisotropy between the rare-earth element and bismuth is dependent on the particular rare-earth element that is used.⁶²

Table III.2 shows the uniaxial anisotropy constant K_u^g and the magneto-crystalline anisotropy constant K_l of various rare-earth elements coupled with bismuth at room temperature. Since these numbers are highly dependent on the growth conditions, and on the concentration of bismuth and rare-earth elements in the film, the numbers in Table III.2 are only used for comparison. In addition, the films in the study that provided the data for Table III.2 are grown on (111) - oriented substrates, whereas the films for this study are grown on (100) - oriented substrates. As a result, the particular values for this experiment are expected to differ slightly from those in Table III.2.

Table III.2 K_u^g and K_l values for rare-earth elements when coupled with bismuth in (111) films at room temperature. [62]

Rare-earth	K_u^g ($\pm 10\%$) (10^3 erg/cm³)	K_l ($\pm 25\%$) (10^3 erg/cm³)
Pr	-140	
Nd	~0	-15
Sm	330	-13
Eu	200	-31
Gd	65	-7.8
Tb	156	-8.2
Dy	59	< -5
Y	69	-6
Ho	26	< -5
Er	12	-6.9
Tm	9	-7
Yb	21	-3.4
Lu	17	-5.2

Up to this point the basic growth process of epitaxial Bi substituted garnet thin films has been presented. The material properties requirements can be put together with the understanding of how these material properties can be controlled by chemical substitution of the garnet unit cell. The result is a complex picture involving the space of growth parameters (undercooling, melt composition, substrate rotation). This process has been termed by some as "molecular engineering" of garnets.⁶³ The most important garnets physical properties and means of controlling them by choosing the right chemistry are listed in Table III.3.

Table III.3 Garnet properties of importance for sensor applications

Property	Requirement	Means of control
Magneto-optical activity	Increase	Enhancing the Bi incorporation
Saturation magnetization ($4\pi M_s$)	Decrease	Substitution of d-sites with diamagnetic ions like Al and Ga
$\frac{dM_s}{dT}$	Zero or very low at operating temperature	c-site substitution with Gd
Optical absorption	Very low	Lead-free melts or growth at low undercoolings
Lattice mismatch	Complete match or compression	Proper choice of melt stoichiometry and substrates Increased Bi incorporation through large undercooling and/or RPM
Growth-induced anisotropy	negative	The (Bi-Lu) pairing induces a negative slope of the growth-induced anisotropy as a function of undercooling, while the (Bi-Gd-Lu) system is discussed in more detail in Chapter 4.

Chapter 4: Characterization of epitaxial single crystal garnet thin films

In the present chapter, a short review of the classical techniques used for magnetic material analysis is presented. Next, novel optical methods are described, that allow the measurement of magnetostriction and anisotropy constants in thin epitaxial garnet films. In the end, the results of all these measurements are combined and utilized to characterize in detail the influence of different growth parameters (e.g. melt composition, melt undercooling, substrate rotation rate) on the properties of epitaxial thin films.

4.1 X-ray measurement of lattice mismatch

Since the substrate thickness is very large compared to that of the grown films, the value of its lattice constant will not change under the strain. The film will grow in such a way that its lattice will match that of the substrate in the horizontal direction. Perpendicular to the film, there will be a lattice mismatch that can be measured experimentally using X-ray diffraction: As mentioned before, in order to grow high quality crystalline films, it is very important to control and measure this lattice misfit between the epitaxial film and the substrate:

$$\Delta a_{\perp} = a_s - a_f, \quad (4.1)$$

where a_s is the lattice constant of the substrate, and a_f is the lattice constant of the epitaxial film.

The lattice misfit plays an important role not only because it controls the quality of the grown films but also because it induces a uniaxial anisotropy:

$$K_u^\lambda = -\frac{3}{2} \frac{E}{1+\nu} \frac{\Delta a_\perp}{a_s} \lambda_{111} \quad (4.2)$$

for films grown on (100) oriented substrates, where $E = 2.055 \times 10^{11} J/m$ is the Young modulus, $\nu = 0.296$ is the Poisson ratio and λ_{111} the magnetostriction constant.⁶⁴ Depending on the chemical substitutions made, the substrate lattice a_s can have values ranging from $1.2382nm$ to $1.2511nm$.⁵⁶

If the lattice constant of the garnet film is smaller than that of the substrate ($\Delta a_\perp > 0$) the film is under tensile stress and this induces a positive uniaxial anisotropy that favors out-of-plane magnetization configuration.

If the lattice constant of the garnet film is larger than that of the substrate, the film is under compressive stress and this induces a negative uniaxial anisotropy that favors the in-plane magnetization state. According to Ref. 35 the range of Δa_\perp for which epitaxial growth of garnets is possible is limited by: $-7 \cdot 10^{-12} m < \Delta a_\perp < 3 \cdot 10^{-12} m$.

The diffractometer used in the measurements has an x-ray source emitting at the CuK_α lines with wavelengths $\lambda_1 = 0.15405nm$ and $\lambda_2 = 0.15444nm$. The beam is reflected off a GaAs crystal under the (400) direction. The sample is moved in such a way that the sample surface is at an angle θ and the detector at 2θ with respect to the incident beam. A typical rocking curve is shown below:

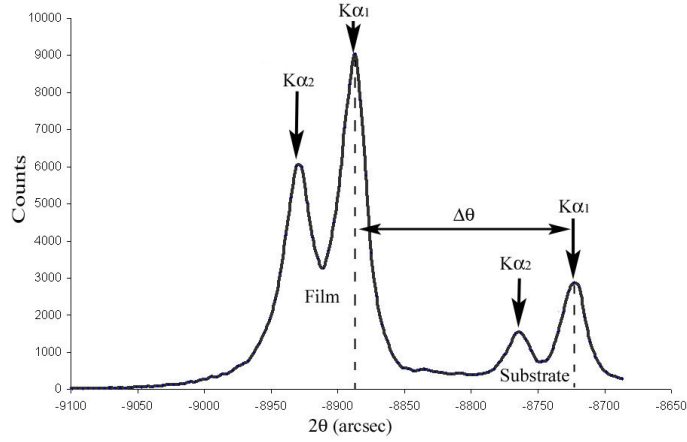


Fig. 4.1 X-ray rocking diffraction curve for a thin film grown in compression.

The misfit can be calculated according to:

$$\Delta a_{\perp} = \frac{\lambda_{\alpha} \sqrt{h^2 + k^2 + l^2}}{2} \left(\frac{1}{\sin \theta_s} - \frac{1}{\sin \theta_f} \right), \quad (4.3)$$

where (h, k, l) are the Miller indices, θ_s and θ_f are the angles of maximum intensity for the substrate and for the film respectively.

For (100) oriented substrates we used the (800) diffraction peak with $\theta_s = 59.7^{\circ}$, and for (111) oriented substrates we used the (444) diffraction peak with $\theta_s = 51.9^{\circ}$.

Since our diffractometer does not provide absolute values for the angles we could not use the above expression. Instead, since the peak separation $\Delta\theta$ is very small compared to θ_s we used the linear approximation:

$$\sin \theta_f = \sin(\theta_s + \Delta\theta) = \sin \theta_s + \cos \theta_s \cdot \Delta\theta. \quad (4.4)$$

Thus Eq. (4.3) becomes:

$$\begin{aligned}\Delta a_{\perp} &= \frac{\lambda_{\alpha} \sqrt{h^2 + k^2 + l^2}}{2} \left(\frac{1}{\sin \theta_s} - \frac{1}{\sin \theta_f} \right) = \frac{\lambda_{\alpha} \sqrt{h^2 + k^2 + l^2}}{2} \left(\frac{1}{\sin \theta_s} - \frac{1}{\sin(\theta_s + \Delta\theta)} \right) = \\ &= \frac{\lambda_{\alpha} \sqrt{h^2 + k^2 + l^2}}{2} \frac{\sin(\theta_s + \Delta\theta) - \sin \theta_s}{\sin \theta_s \sin(\theta_s + \Delta\theta_s)} = \frac{\lambda_{\alpha} \sqrt{h^2 + k^2 + l^2}}{2} \frac{\cos \theta_s \cdot \Delta\theta}{\sin^2 \theta_s} = a_s \frac{\Delta\theta}{\tan \theta_s},\end{aligned}\tag{4.5}$$

where $\frac{2a_0}{\sqrt{h^2 + k^2 + l^2}} \sin \theta_s = \lambda_{\alpha}$ is the Bragg condition. The above value has to be

corrected for the elastic strain yielding:

$$\frac{\Delta a_{\perp}}{a_s} = \frac{1 - \nu}{1 + \nu} \frac{\Delta\theta}{\tan \theta_s}.\tag{4.6}$$

4.2 Determination of film thickness

The measurement of the thickness is performed from wavelength dependent measurements of the reflection and transmission coefficients of the thin films using an ellipsometer. The physical principle behind this method is the interference between multiple reflections that take place at the film-air and film substrate interfaces. Light with different wavelengths will travel different paths through the material and for some wavelengths the constructive interference condition is satisfied while other wavelengths suffer destructive interference. A typical optical signal obtained for an angle of incidence $\theta_i = 45^\circ$ is shown in Fig. 4.2. For low dispersion, the following equation can be used to determine the thickness from the position of the maxima in the reflected signal:

$$t = \frac{\frac{1}{2}(N_1 - N_2) \sqrt{(n_f^2 - \sin^2 \theta_i)}}{n_f^2 \left(\frac{1}{\lambda_1} - \frac{1}{\lambda_2} \right)}\tag{4.7}$$

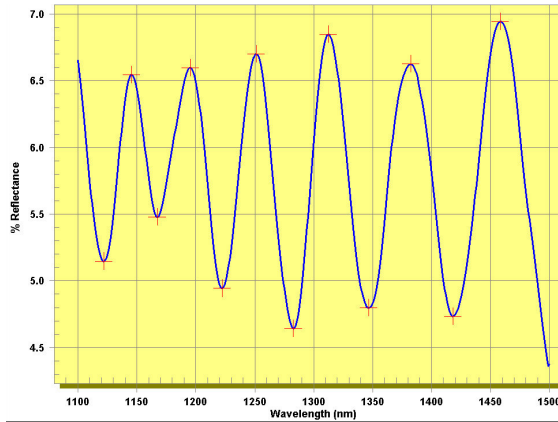


Fig. 4.2 Interference pattern due to multiple reflections inside an epitaxial thin film. The peak separation is related to the sample thickness.

If the dispersion effects are important (e.g. close to absorption wavelengths), and Bi incorporation is large, then the index of refraction used to fit the experimental ellipsometer data can be described by the following expression:⁶⁵

$$n(\lambda, x) = 2.174 + \frac{0.0593}{\lambda^2} + \left(0.103 + \frac{0.0371}{\lambda^2} \right) x, \quad (4.8)$$

where x is the Bi incorporation and λ is the wavelength.

4.3 Magnetic measurements of material properties

Two of the most used techniques to analyze magnetic materials are Vibrating Sample Magnetometry and Ferromagnetic Resonance. The discussion will include their working principles and applications in measuring properties of interest of thin epitaxial garnet films.

Vibrating sample magnetometry (VSM) is an important and widely used technique in magnetism, but it is a relative technique since the VSM has to be

calibrated before the measurements are performed. The calibration is performed by using a sample with a known magnetic moment (in our case a Ni sphere with $M_s=57.4$ memu).

We used VSM in order to measure the saturation magnetization, hysteresis loops and anisotropy constants of our samples. The working principle of the VSM is as follows. The sample material is placed in a Plexiglas (non magnetic) holder, centered in the uniform field region produced by the pole pieces of an electromagnet. A magnetic moment is induced in the sample by the electromagnet field. When the sample is vibrated by a transducer, an electric signal is induced in a stationary pickup coil pair due to the changing magnetic flux. By using a lock-in amplifier tuned to the vibration frequency, this signal can be related to the magnetization value of the sample.

At small fields the slope is higher because the sample is unsaturated. With increasing fields the sample starts to saturate, reducing the slope. Even after the sample becomes magnetically saturated, the slope does not go to zero. This is due to the paramagnetic behavior of the GGG substrate. This effect is especially important because the volume of the epitaxial films is just a small fraction of the substrate volume. In order to obtain the correct hysteresis loop for the sample, the substrate paramagnetic effect has to be removed. A typical corrected hysteresis loop of a magnetization measurement for a garnet thin films is shown in Fig. 4.3.

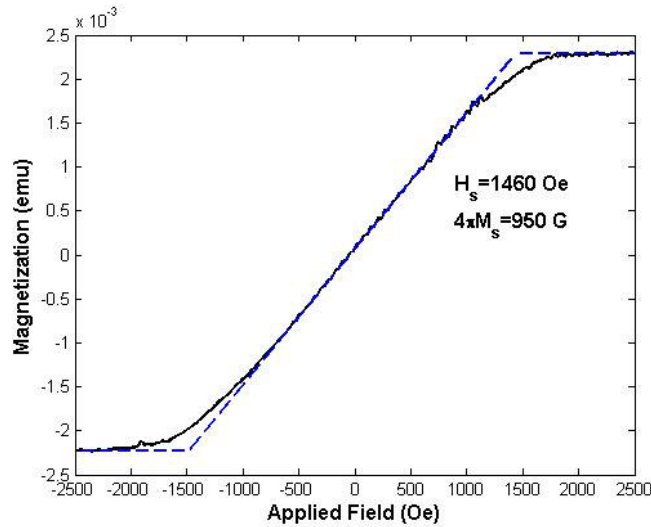


Fig. 4.3 Typical corrected VSM loop for garnet thin films with in-plane magnetization.

After the corrected hysteresis loop has been obtained, one could determine the saturation magnetization, the saturation fields and the slope of the magnetization curve at $B_{ext} = 0$, a parameter that is directly related to the film sensitivity. Previous experiments performed by our group showed that VSM measurements data can be used to infer the value of anisotropy constants of the material.⁶⁶

Ferromagnetic resonance is a reliable, widely used technique in magnetism.⁶⁷ For materials with narrow absorption bandwidth as garnets, many types of experiments can be performed using FMR: anisotropy measurements, spin waves studies, non linear effects. Our research group built an in-house FMR system as described by J. Zhang.⁶⁸ The FMR measurements can be used to determine the uniaxial and cubic anisotropy by performing angle dependent measurements of the resonance field.

The physical principle behind the FMR measurement is the precession of the magnetization vector around a strong DC field, when the sample is subject to an RF field. This process is described by the well-known Landau-Lifshitz equation.⁶⁷

$$\frac{d\vec{M}}{dt} = -\gamma(\vec{M} \times \vec{H}_{eff}) - \frac{\lambda}{|\vec{M}|} \vec{M} \times (\vec{M} \times \vec{H}_{eff}), \quad (4.9)$$

where γ is the gyromagnetic ratio, λ is the damping term and \vec{H}_{eff} is the resultant magnetic field that combines the applied external magnetic field and the internal fields resulting from the presence of material anisotropies and demagnetization factors.

The Landau-Lifshitz equation can be solved analytically in just a limited number of cases:

- when the amplitude of the RF field is very small compared to the applied DC field, perturbation techniques can be used;
- when the amplitude of the RF field is no longer negligible compared to the applied DC field (high microwave power), non linear effects start to appear and the equation cannot be analytically solved. Except for the case discussed by Mayergoyz *et. al.*,⁶⁹ where the RF field has rotational symmetry and an analytical solution can be determined and its mathematical properties analyzed.

For all other cases, only numerical solutions of the Landau-Lifshitz can be attempted.

For small excitation powers, the resonance frequency of the magnetization precession can be obtained using the concept of free energy density presented in Chapter 1, through the use of the Smit-Suhl formula:^{67,70,71}

$$\left(\frac{\omega}{\gamma}\right)^2 = \frac{1}{M_s^2 \sin^2(\theta_M)} \left(\frac{\partial^2 f}{\partial \theta_M^2} \frac{\partial^2 f}{\partial \varphi_M^2} - \left(\frac{\partial^2 f}{\partial \theta_M \partial \varphi_M} \right)^2 \right), \quad (4.10)$$

where ω is the resonant microwave frequency and f the free energy density. As shown in Chapter 1, the free energy density f includes many terms: the Zeeman energy, the demagnetizing energy, the exchange energy, the uniaxial energy and the cubic anisotropy.

Using a spherical coordinate system we can express the cubic anisotropy energy for the most common crystallographic directions as:³⁰

$$(100): f_{cubic} = K_1 (\cos^2 \theta \sin^2 \theta + \sin^4 \theta \cos^2 \varphi \sin^2 \varphi)$$

$$(111): f_{cubic} = K_1 \left\{ \frac{1}{3} \cos^4 \theta + \frac{1}{4} \sin^4 \theta - \frac{\sqrt{2}}{3} \sin^3 \theta \cos \theta \cos(3\varphi) \right\} \quad (4.11)$$

A schematic of our FMR system is shown below:⁶⁸

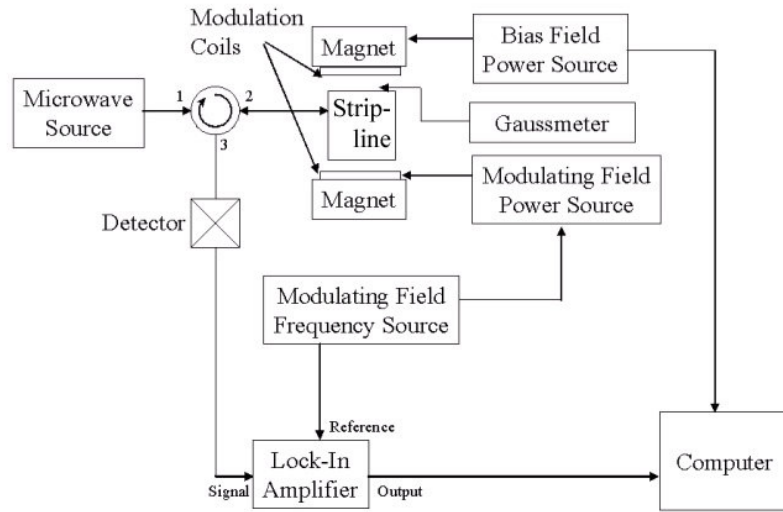


Fig. 4.4 Diagram of FMR system. The resonance spectra are obtained at constant frequency by changing the applied DC field.

The experiments are performed by placing the sample face-down on a microstrip line. The RF signal passing through the microstrip is reflected by a DC block component and a detector diode is used to convert the microwave intensity into a measurable DC voltage. The measurements are performed keeping the frequency of the RF source constant and changing the value of the applied magnetic field by

controlling the current through the electromagnet. A small modulation field is superposed on the DC field and the resulting signal is digitally processed using a lock-in amplifier. The output of the lock-in is proportional to the derivative of the microwave absorption coefficient in the sample. When the resonance condition is reached, the sample absorption increases. The value at which this resonance takes place can be related to the value of the gyromagnetic ratio and to the value of the cubic and uniaxial anisotropies.

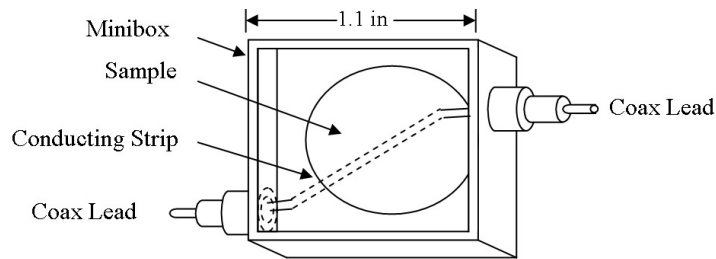


Fig. 4.5 Schematic of the microstrip line and encasing box for FMR experiments.

A typical variation of the reflectivity coefficient of the microstrip structure is shown in Fig. 4.6. We see that the main resonance peaks can be easily identified, but other absorption peaks are present suggesting that the microwave energy is also coupled into spin-wave or other surface modes.

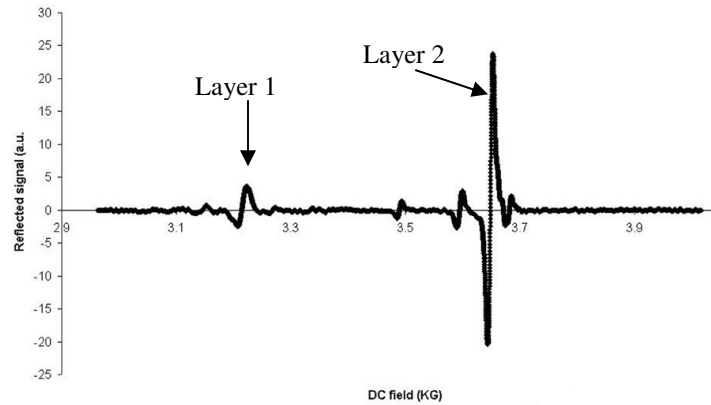


Fig. 4.6 Typical FMR spectra of a double layer epitaxial film showing two strong absorption peaks corresponding to the uncoupled layers.

4.4 Optical measurements of material properties

As seen above, some measurements, such as the measurement of the saturation magnetization of the sample and its dependence on temperature, the measurement of anisotropy constants of the material, can be performed using magnetic methods such as VSM and FMR. As we will see in Chapter 5, many of these material properties are essential to the functioning of the magnetic field sensors based on garnets. Thus, in order to understand how the sensor works and how to relate the measurements to the actual values to be measured, there is a need for characterizing the materials using as many methods and techniques as possible. Since the garnets are optically active and thus can be optically studied, most of these parameters can also be measured indirectly through optical methods. During the previous research stages, we have proven that we can measure optically the Faraday rotation, the magnetostriction constants, and the cubic and uniaxial anisotropies. These results are presented in three published papers.^{72,73,74} To the extent of our knowledge the only parameter that would

be more difficult to determine optically is the magnetization for which magnetic methods are still irreplaceable.

The optical methods are important for many reasons. First of all, they are local, which means that we can probe the sample using a small diameter laser beam and the output will give us information related only to the specific region of interest. By using a scanning stage, a map of the property of interest can be obtained for the entire surface. This is a strong advantage versus the magnetic methods, because the latter ones offer information averaged at the scale of the entire sample. Secondly, optical methods are much more sensitive than their magnetic counterparts and much more flexible. This motivates research aiming to replace some of the magnetic measurements. In the FMR measurements, the use of parts that have some level of magnetic activity (cables, connectors) cannot be prevented without investment in expensive parts. Usually, at the high values of magnetic fields used in these measurements, many parts will perturb the field inducing artifacts and errors in the measurements. However, if an optical FMR system would be built, the cables and connectors will be replaced by optical fibers and lenses thus greatly reducing this interference effects. But maybe the strongest advantage of the optical methods is that they are very fast, capable of distinguishing processes on the scale of GHz and higher. They are the only methods that currently offer reliable information about the temporal evolution of high speed phenomena like spin transport and magnetization dynamics. This is accomplished through the use of ultra-short laser pulses and optically transparent electrodes. These techniques provide the required driving electromagnetic force without affecting the optical path of the probing laser.⁷⁵

4.4.1 Faraday Rotation

Maybe the most relevant optical measurement is finding the Faraday rotation per unit length and its changes with the applied magnetic field. From here the sensitivity can be extracted. This measurement is of the **free space type**, because it does not involve the use of guiding structures. The light is sent perpendicular to the film surface and the sample is positioned in the uniform field region of a coil or pair of coils. A polarizer and analyzer are used to detect the rotation of the polarization plane when the light passes through the sample.

Typical optical responses at low frequencies of the applied magnetic field are shown in Fig. 4.7 and 4.8. We see that in the case of samples with out-of-plane magnetization, the sensitivity to magnetic fields applied perpendicular to the film surface is one order of magnitude higher than for in-plane fields. This type of behavior is desirable when aiming for magneto-optic indicator applications. For sensors it would be desirable to have a strong uniaxial anisotropy so that the sensitivity to perpendicular fields will be zero.

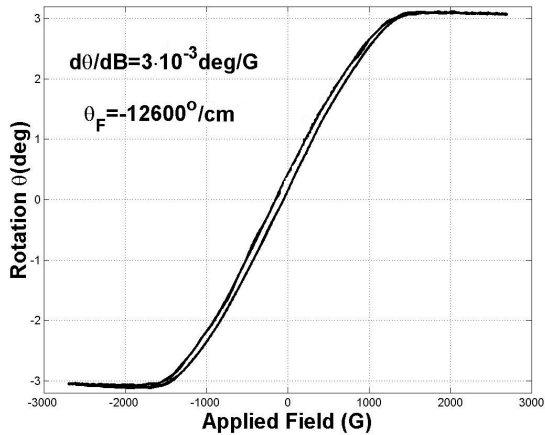


Fig. 4.7 Optical hysteresis loop for a garnet film with in-plane magnetization.

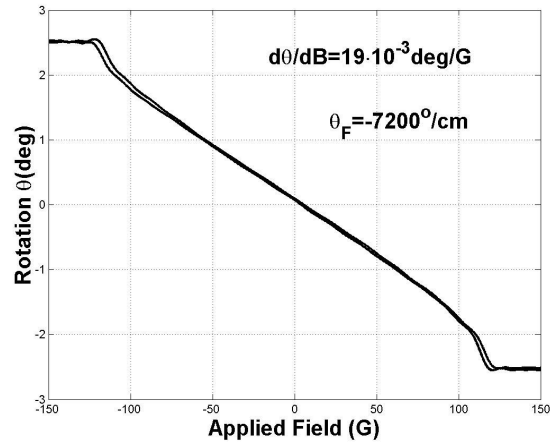


Fig. 4.8 Optical hysteresis loop for a garnet film with out-of-plane magnetization. Observe the x-scale difference vs. Fig. 4.7.

4.4.2 Magnetostriction constants in (111) – oriented garnets

Another successful optical measurement that we reported was the determination of the magnetostriction constant.⁷² As discussed in Chapter 1, any lattice mismatch between the substrate and the epitaxial film induces a mechanical stress. Through the magneto-elastic coupling coefficients, this mechanical stress is translated into a uniaxial anisotropy that can have significant values and thus can strongly influence the equilibrium position of the magnetization. Therefore it is important to accurately measure the value of the magnetostriction constant. For thin films grown on (111) oriented substrates we accomplished this by mimicking the effect of an external applied stress on the magnetic domain structure with an applied magnetic field perpendicular to the sample.

The evolution of magnetic domain structure under the influence of externally applied stresses has been studied by using a modified optical version of the strained-substrate method.⁷⁶ This method utilizes a polarized-light microscope to reveal magnetic domain structures through the Faraday rotation effect (see Fig. 4.9). This

modified method has the following advantages. First, it leads to direct observations of the magneto-elastic coupling through observations of stress-induced changes in domain structures. Second, a uniform pressure can be applied perpendicular to the sample surface and therefore, the amount of stress induced in garnet films can be readily estimated.⁷⁷ The substrate is mounted on an elastic membrane and on the top of it there is a Teflon ring with an inner radius of 6 mm. By bending the membrane, the substrate, and thus the epitaxially grown thin film can be stressed by a controlled amount. An air-cooled coil has been used to create a uniform magnetic field perpendicular to the film surface.

As seen in Fig. 4.10, as the applied stress is increased, the magnetization changes the equilibrium position going from the locally uniform (very important!) state 1 in the locally uniform state 2 through a series of intermediate positions. The same evolution of the stripe pattern has been reproduced using an increasing magnetic field applied perpendicular to the film (see Fig. 4.11). Since the initial and final magnetization equilibrium positions are identical in both cases, the magnetostriction constant is shown to be equal to:⁷²

$$\lambda_{111} = \frac{2}{3} \frac{M_s H_z \cos \theta}{\sigma \sin^2 \theta} \quad (4.12)$$

where H_z is the applied magnetic field perpendicular to the film surface, M_s is the saturation value of the magnetization, θ is the angle between the magnetization vector and the (111) direction (perpendicular to the film) and σ is the stress induced by bending in the plane of the film.

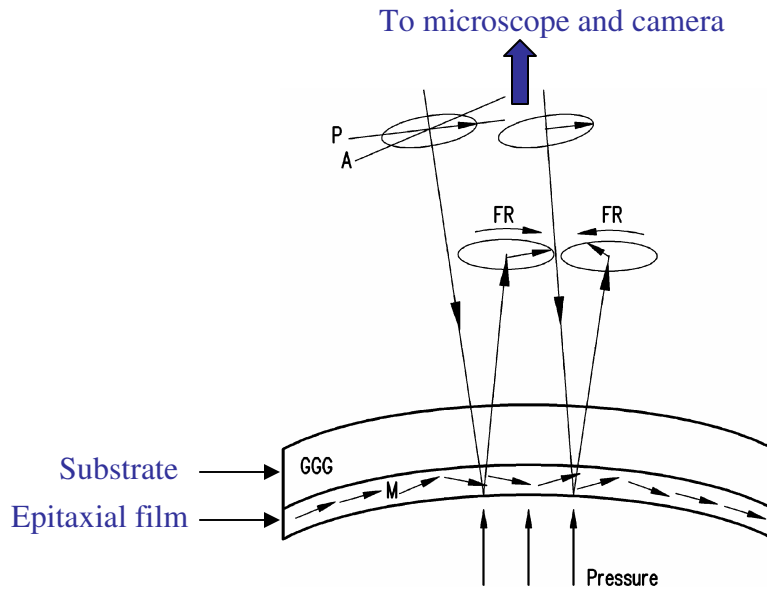


Fig. 4.9 The mechanical bending of the thin films induces stripe domain structures that can be observed with a polarized light microscope using the Faraday rotation effect (FR) (P - polarizer; A - analyzer).

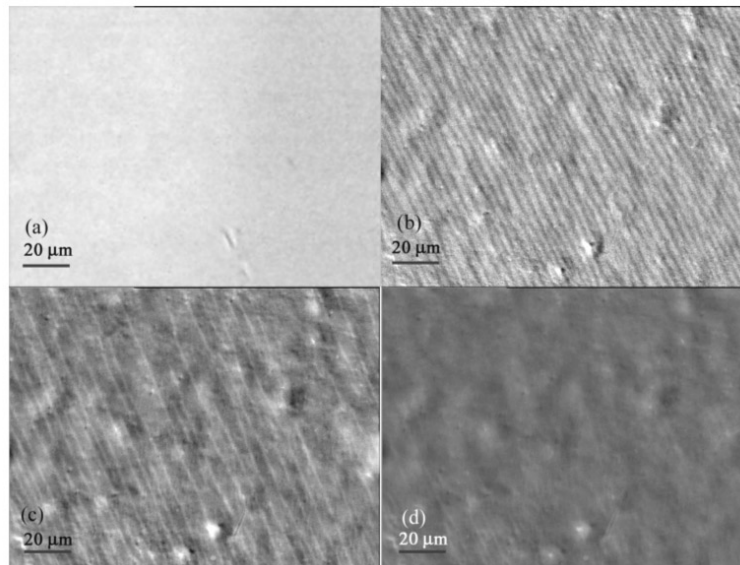


Fig. 4.10 Stripe domain structure nucleation and evolution under the perpendicular effective field induced by stressing the film. The in-plane field is $H_{c1} = 1.43 \cdot 10^3$ A/m (~ 18 Oe).

(a) $\sigma = 0$ dynes/cm², (b) $\sigma = 1.8 \cdot 10^6$ dynes/cm², (c) $\sigma = 3.2 \cdot 10^6$ dynes/cm² and (d) $\sigma = 4.27 \cdot 10^6$ dynes/cm².

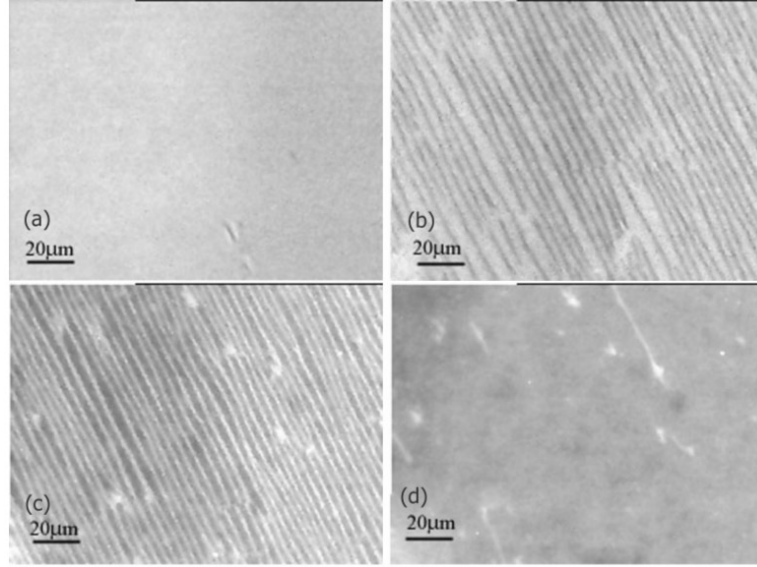


Fig. 4.11 Stripe domain structure nucleation and evolution under perpendicular applied magnetic field. The in-plane field is $H_{c1}=1.43 \cdot 10^3$ A/m (~ 18 Oe)
 (a) $H_{\perp}=0.06 \cdot 10^3$ A/m (~ 0.7 Oe), (b) $H_{\perp}=0.2 \cdot 10^3$ A/m (~ 2.5 Oe),
 (c) $H_{\perp}=0.43 \cdot 10^3$ A/m (~ 5.5 Oe) and (d) $H_{c2}=0.53 \cdot 10^3$ A/m (~ 6.7 Oe)

TABLE IV.1 Chemical content of $(\text{Lu}_{3-x}\text{Bi}_x\text{Fe}_{5-y}\text{Ga}_y\text{O}_{12})$ thin films and the M_s values

Sample	x	y	$4\pi M_s(\text{G})$
1	0.5	1.041	220
2	0.6	1.058	200
3	0.64	0.99	290
4	0.73	1.058	200
5	0.8	1.006	270

For samples with the stoichiometry shown in Table IV.1 we obtain the results presented in Table IV.2. As seen, the results obtained through this method compare very well with those reported in the literature for samples with similar stoichiometry. These results are important because they show that the magnetostriction constant and the uniaxial anisotropy both increase with the Bi incorporation in the film.

TABLE IV.2 Anisotropy constants of (111)-oriented thin films and the λ_{111} values

Sample	$K_1(\text{J/m}^3)$	$K_u(\text{J/m}^3)$	$\lambda_{111}(\cdot 10^{-6})$	$\lambda^*_{111}(\cdot 10^{-6})$	$K_u^\lambda(\text{J/m}^3)$	$K_u^g(\text{J/m}^3)$
1	-150	-345	-0.8	-1.00	-75	-270
2	-150	-340	-0.98	-1.03	-65	-275
3	-180	-380	-1.11	-1.16	-120	-260
4	-155	-240	-0.91	-1.10	-74	-166
5	-180	-290	-1.42	-1.22	-162	-128

4.4.3 Cubic anisotropy constant

Another optical measurement that we have successfully performed is finding the cubic anisotropy constant for Bi-substituted garnets.⁷⁴ The knowledge of this quantity and how to control it are very important aspects for obtaining good sensor films. When the uniaxial anisotropy is negative and the sample has in-plane magnetization, the equilibrium position is solely controlled by the cubic anisotropy (the demagnetizing field is zero). The cubic anisotropy induces 'easy', and 'hard' equilibrium axes for the magnetization. The motion of the magnetization in the plane of the sample will be controlled by these axes. Thus it is of great importance to accurately measure the cubic anisotropy constant for garnets with in-plane magnetization. The usual way to accomplish this is by FMR experiments where the shift in the resonance field is fitted for different angular orientations of the sample with respect to the applied DC field. This is a cumbersome measurement requiring many steps and numerical fitting. Our proposed optical method is much faster and does not involve complex numerical fitting.

This process can be modeled using the free energy density which in the case of (100) films with in-plane magnetization has this simple form:

$$f = K_1 \sin^2 \theta \cos^2 \theta - M_s H_{ap} \sin \theta \quad (4.13)$$

There will be four equilibrium magnetization states, which for negative K_1 are oriented along the four $\langle 110 \rangle$ in-plane axes, as shown in Fig. 4.12.

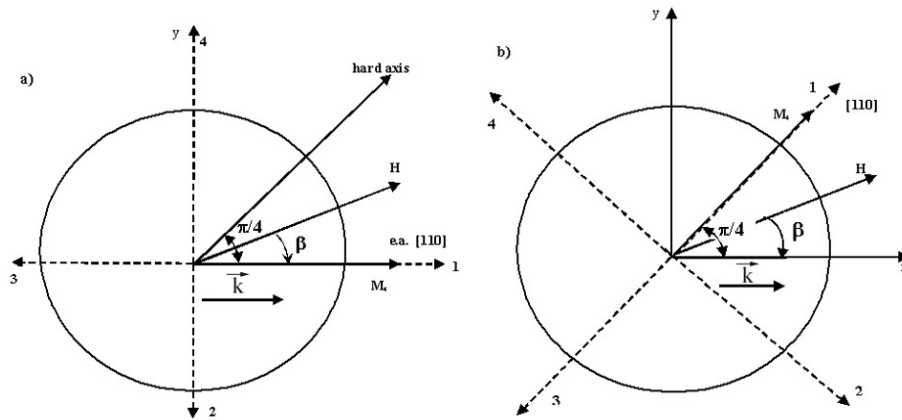


Fig. 4.12 Orientation of the magnetization equilibrium states when (a) the light propagates along an easy axis and (b) the light propagates along a hard axis.

The experimental apparatus consists of two pairs of orthogonal coils, wrapped around a soft ferromagnetic ring with the sample positioned at the center. These spatially orthogonal coils are excited by AC sinusoidal currents shifted in time by 90° to create a uniformly rotating magnetic field in the sample plane. A red HeNe polarized laser beam ($\lambda=632.8$ nm) is incident on the sample at a small angle.

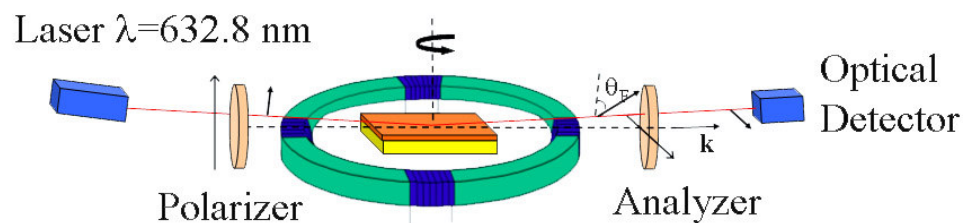


Fig. 4.13 Schematic of the experimental setup used to measure the cubic anisotropy constant of garnet thin films with in-plane magnetization.

In the simplifying case when the out-of-plane component of the magnetization is much smaller than the in-plane component, the amplitude of the Faraday rotation of the polarization plane is given by:

$$\theta_F = A \cdot M_s \cos \theta \cos \alpha_0 \quad (4.13),$$

where A is related to material properties and film thickness, M_s is the saturation magnetization, θ is the in-plane angle between the magnetization vector and \vec{k} , and α_0 is the out-of-plane angle between the magnetization and the direction of light propagation (\vec{k}) in the film. The angle α_0 is related to the incident angle of the probing laser beam by Snell's law and is close to $\pi/2$ in our experiments, thus $\cos(\alpha_0) = 1$.

Neglecting the Cotton-Mouton effect, the intensity of the light incident on the detector can be expressed as:

$$I = I_{\min} + I_0 \cos^2(\varphi_0 + \theta_F) \quad (4.14),$$

where φ_0 is the angle between the polarizer and the analyzer and I_{\min} is the intensity of the light at $\varphi_0 = \pi/2$. Our samples are 2-5 microns thick and θ_F on the order of 1° - 5° . For these small angles, neglecting the higher order terms, Eq. (4.14) can be rewritten as:

$$I = I_{\min} + I_0 \cos^2(\varphi_0) - I_0 \theta_F \sin(2\varphi_0) \quad (4.15).$$

Thus for φ_0 fixed, the change in the intensity of the light is linearly proportional to the Faraday rotation angle. Thus, the value of the magnetization component parallel to the light path can be directly probed through changes in the optical intensity of the reflected light.

The first step is to determine the orientation of the crystallographic axes in the plane of the sample (see Fig. 4.12). This is accomplished by studying the shape of the

optical response in the case of an applied rotating magnetic field in the plane of the thin films. When the samples are subject to rotating magnetic fields of small amplitude, the domain walls will move and locally the magnetization will switch to a new equilibrium state. This appears as jumps in the optical signal, e.g. those illustrated in Fig. 4.14.

In the first arrangement, when the light is parallel to one of the easy axes, the observed signal is shown in Fig. 4.14 (a). When the magnetization is in state 1, θ_F is positive. The first jump appears when the magnetization is switched to state 2. In this state there will be no Faraday rotation because the magnetization will be perpendicular to \vec{k} , as shown in Fig. 4.12 (a). As the magnetization switches to state 3, a second jump is observed because the in-plane magnetization becomes opposite to \vec{k} . A third jump is observed when the magnetization is switched to state 4. For this jump, the Faraday rotation changes from the previous negative value to zero. Finally, the last jump is observed when the magnetization is switched from state 4 back to state 1. In this case, θ_F is changed from zero to a maximum positive value, because in state 1 the in-plane magnetization is oriented along \vec{k} (Fig. 4.12 (a)). Therefore, during a complete rotation of the magnetic field, the output signal exhibits four jumps, two jumps between the zero level and a positive maximum value of θ_F , and two jumps between the zero level and a negative maximum value of θ_F .

In a second arrangement, the light propagates parallel to one of the hard axes. In this case, the optical response is shown in Fig. 4.14 (c). Here, only two intensity levels appear in the optical response. When the magnetization is in the states 1 or 2, θ_F will be positive. Moreover, θ_F will be the same, because the angles between the

states 1 or 2 and \vec{k} are the same, as seen in Fig. 4.12 (b). Similarly, the Faraday rotation will be the same when the magnetization is in the states 3 or 4. But since the direction of the in-plane magnetization will be opposite to \vec{k} , θ_F will be negative. Therefore, the switching of magnetization between states 1 and 2, and between 3 and 4 occurs without any jumps in the optical response.

The angle between the light path and a reference mark on the sample was changed, keeping the rotating field on. When the recorded output signal presented four distinct jumps and a zero level we concluded that at that angle the easy axis is parallel to the propagation vector \vec{k} and we marked it on the sample. When the signal presented only two distinct jumps, and had smaller amplitude, we concluded that the light propagated along a hard axis, and we marked the direction of the hard axis on the sample.

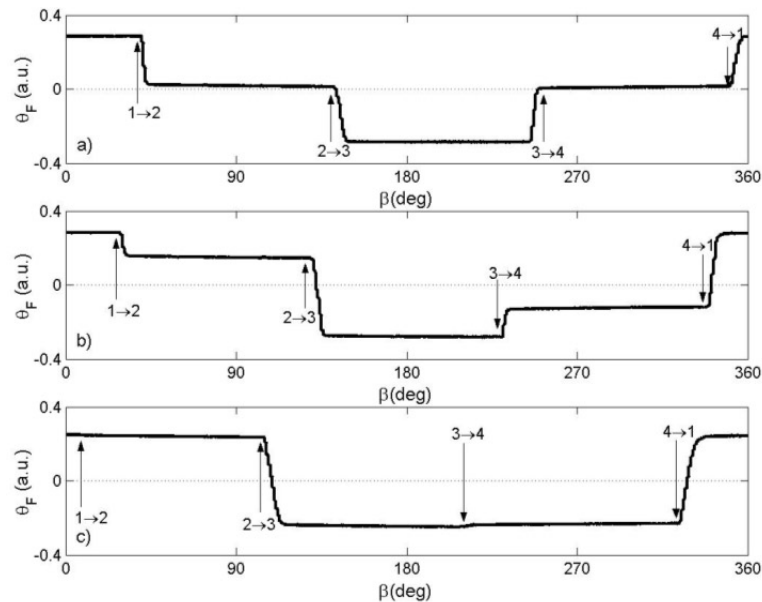


Fig. 4.14 Optical response induced by a rotating magnetic field in the plane of a (100) garnet film. (a) light propagates parallel to a (110) axis; (b) light propagates along an intermediate direction; (c) light propagates along a (100) axis.

To determine K_1 a unidirectional uniform magnetic field was used. The sample was positioned so that the light direction was parallel to one of the hard axes. A square wave modulated magnetic field was applied perpendicular to the light path. The choice of a square wave modulated field allows for a better identification of the optical intensity levels. In this case the magnetization was pinned in the same state for a longer time than in the case of a sinusoidal field. As a result, improved signal-to-noise ratio was achieved.

At very low fields, the samples have multidomain structures and the optical signals reveal artifacts due to Barkhausen jumps and incomplete switching of the magnetization. These artifacts gradually disappeared as the in-plane field was increased, usually to values higher than 10 Oe for most of our samples. Thus, it can be considered that a uniform magnetization state has been reached. Consequently, the free energy density for the in-plane magnetization case can be expressed as:³⁰

$$E = K_1 \sin^2 \theta \cos^2 \theta - M_s H_{ap} \sin \theta \quad (4.16),$$

where θ is the angle between the magnetization vector and \vec{k} . \vec{H}_{ap} is applied perpendicular to \vec{k} , in the plane of the sample.

At the magnetization equilibrium, we have the following relations: $\frac{\partial E}{\partial \theta} = 0$ and

$\frac{\partial^2 E}{\partial^2 \theta} > 0$. This is equivalent to $\theta = \frac{\pi}{2}$ if $H_{ap} \geq \frac{2K_1}{M_s}$ or whose

$$H_K = \frac{2K_1}{M_s} = \frac{H_{ap}}{\sin \theta \cos 2\theta} \quad (4.17)$$

for $H_{ap} < \frac{2K_1}{M_s}$.

The amplitude of the Faraday rotation will be highest when there is no applied field. In this case the magnetization will be oriented along the easy axis and specified by $\theta_0 = \pi/4$. As the field is increased, the magnetization is forced to rotate toward the direction of the field and the optical signal decreases as shown in Fig. 4.15. At this point θ is given by Eq. (4.17) with $H_{ap} = H$, the amplitude of the field modulation.

In order to find θ , we measured the Faraday rotation at $H_{ap} = 0$ and at $H_{ap} = H$ and we computed their ratio using Eq.(4.13):

$$\frac{\theta_F}{\theta_F^0} = \frac{\cos \theta}{\cos \theta_0} = \sqrt{2} \cos \theta \quad (4.18).$$

Since the optical signal is easily measured, the Faraday rotation can be related to the intensity of the light making θ discernable from Eq. (4.18). With θ known, the value of the cubic anisotropy field is obtained immediately from Eq. (4.17).

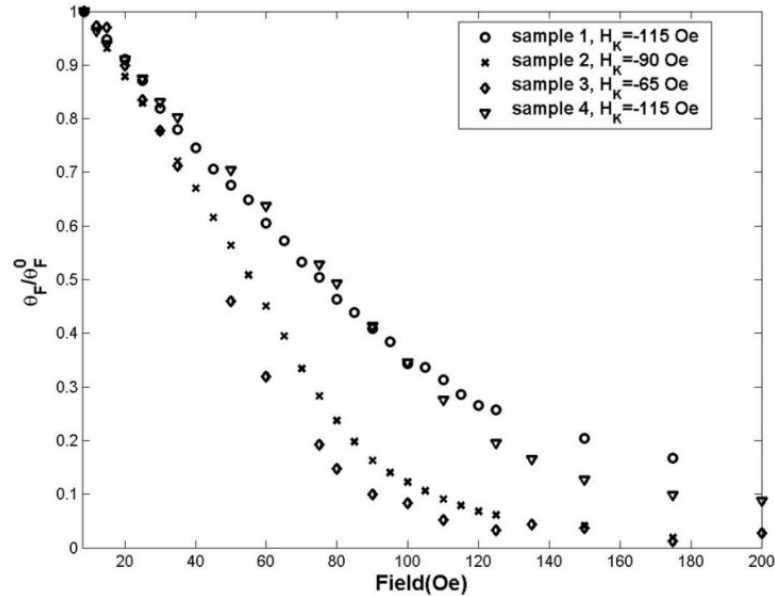


Fig. 4.15 Optical response of samples when the magnetic field is applied transverse to the light propagation direction. As expected, the Faraday rotation drops faster for samples with lower cubic anisotropy fields.

The results for a series of (100) oriented $(\text{Lu}_{3-x}\text{Bi}_x)(\text{Fe}_{5-y-z}\text{Pt}_y\text{Ga}_z)\text{O}_{12}$ are shown in the following plot compared with results from previous measurements (performed using FMR) on samples with similar stoichiometry. The increase in the saturation magnetization is due to a decrease in Ga substitution due to higher growth undercoolings. In the same time higher undercoolings mean more Bi substitution. Thus, as it is shown in Fig. 4.16, the cubic anisotropy decreases with decreasing Ga substitution and with increasing Bi substitution.

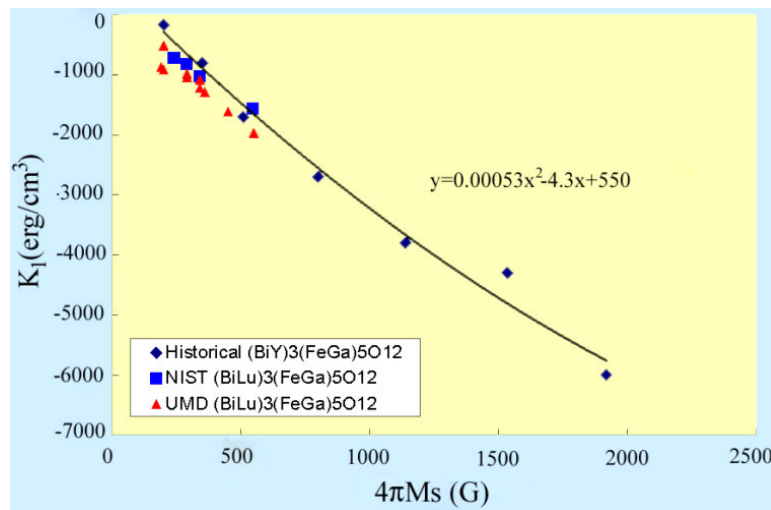


Fig. 4.16 Comparison of measured cubic anisotropy using the method in [74] with previous data reported in the literature.

4.5 Influence of melt chemistry and growth conditions on the properties of LPE - grown thin epitaxial garnet films

The above described measurement methods have been used extensively for analysis of our in-house grown samples. As described in the following subchapters, these measurements were instrumental in understanding in more detail the control of epitaxial films properties in the liquid phase epitaxy technique. First the influence of

melt chemistry and undercooling on the growth induced anisotropy, magnetization, and Faraday rotation will be discussed. The second subchapter discusses the effect of rotation rate (RPM), which together with the undercooling is another method used in LPE to control the growth of epitaxial films.

The advantage of the liquid phase epitaxy process described in Chapter 3 is that it yields single crystal samples. This is very important for our waveguide-based sensor application, since if the sample would be a multi crystal, there will be many reflection at the grain boundaries thus increasing the scattering and reducing the sensors' sensitivity. In order to grow samples with high quality and specific desired properties (a discussion about such properties and how they can be achieved has been presented in part Chapter 3.2), the LPE process offers three main control methods.

First, and the most important one, is choosing the right *melt chemistry*. The melt chemistry is usually expressed by using the different values for the cation oxide ratios shown in Chapter 3.1. This only offers a coarse modality of achieving the desired properties, and in addition it is not very practical to change the melt for every sample that has to be grown. The choice of the right melt chemistry usually starts from estimating a film composition that will yield desired values of parameters such as lattice mismatch, magnetization, and anisotropy. Subsequently, based on approximation related to the so called "segregation coefficients" which describe the ratio between the concentration of one element in the melt and its concentration in the film, the melt composition is calculated from the desired film composition. Additional calculation steps involved in the choice of melt chemistry are related to consideration of saturation points (the temperature at which no growth will take place

on the dipped substrate) and nucleation points (the temperature at which small garnet crystals start to form at the melt surface due to undercooling – these small crystals negatively affect the optical quality of the final epitaxial layer so it is desirable that the growth process take place at higher temperatures than the nucleation point). This complex interplay of melt chemistry and melt behavior is described in the excellent paper of Fratello *et. al.*⁷⁸ and will not be addressed here in detail.

As mentioned above, the melt chemistry offers only a coarse control over the epitaxial film properties. In order to more finely tune the film's properties, LPE makes use of undercooling and substrate rotation rate (RPM).

The undercooling has a strong impact on the film properties through its effect on bismuth incorporation and diamagnetic substitution levels. It has been shown that the Bi incorporation increases linearly with the undercooling. Since Bi is a large radius ion, this will affect other properties like the crystalline lattice and the uniaxial anisotropy: A detailed discussion on the effect of undercooling will be presented in the next subchapter.

The substrate rotation rate has a similar effect to the undercooling. If the RPM is increased, it is similar to actually increasing the melt undercooling. The effect of RPM on film properties will be discussed in subchapter 4.5.2.

Since the melt undercooling can be controlled within one degree, and the RPM can be also precisely chosen, this generally offers improved control over the film's properties.

4.5.1 Influence of melt chemistry and undercooling

The goal of this set of experiments (growth and material analysis) was to propose (Bi-Gd-Lu) - based melts to grow MOI films with in-plane magnetization and high Bi incorporation on (GGG) substrates with expanded crystallographic lattice. Such single crystal epitaxial garnet thin-films with in-plane magnetization and large Faraday rotation hold promise for potential applications in magneto-optical indicators (MOI) and photonic non-reciprocal devices because their magnetization responds to applied magnetic fields by uniform rotation. This results in the continuous variation of Faraday rotation and offers a true grayscale observation of magnetic flux and domain patterns in garnet-based MOIs used as non-destructive imaging devices for superconductors, magnetic tapes, checks, and banknote magnetic marks.^{79 80}

Previously, MOI epitaxial films with in-plane magnetization have been developed by growing garnets of composition $(\text{BiLu})_3(\text{FeGa})_5\text{O}_{12}$ on (100) and (111) – oriented gadolinium gallium garnet (GGG) substrates with a lattice constant $a_s = 1.2383$ nm.^{23,81} One of the shortcomings of this growth process has been the lattice constant of the GGG substrate which limits the Bi incorporation. In order to enhance the Bi substitution, substrates with larger lattices must be used. In our experiments (100)-oriented Ca-, Mg-, and Zr-substituted (GGG) substrates with a lattice constant $a_s = 1.2498$ nm have been used.

The reason for using a three ion combination (Bi, Gd and Lu) is the following. It has been shown that the growth induced anisotropy is related to the ionic differences between the radius of the rare earths which naturally go in the garnet structure (in our case the rare earths are Gd, and Lu),⁴⁶ and the radius of Bi ion, which is incorporated

in the film structure by the gradient of concentration in the melt. In order to estimate if such melts will yield garnet samples with negative anisotropy, it has been assumed as a first approximation that the three ion interaction affects garnet film anisotropy in a pair-wise additive manner. Thus, the Bi that is a large ion [ionic radius $r_i = 1.13 \text{ \AA}$] will yield a positive K_u^g with Gd [$r_i = 1.053 \text{ \AA}$] and a strong negative K_u^g with Lu which is a smaller ion [$r_i = 0.977 \text{ \AA}$].^{82 83} This suggests the possibility of growing garnet samples with zero or even negative K_u^g by controlling the Lu substitution levels, that is without resorting to high non-equilibrium growth conditions. Assuming a pair-wise additive interaction, this suggests the possibility of growing garnet samples with zero or even negative K_u^g by controlling the Lu substitution levels, and without resorting to high non-equilibrium growth conditions. Recently published results seem to support this approach. For instance, in the work of Fratello *et. al.*⁸⁰ it is shown that thick epitaxial garnet films with in-plane magnetization have been grown by using a Bi-Gd-Lu garnet system at small melt undercoolings (20-40 °C). The present study expands these results to the case of thin epitaxial films.

To help with the interpretation of the results, we removed the variability of one of three growth process control parameters used in LPE. Mainly the rotation rate of the substrate has been kept constant at 64 rpm for every sample. The film compositions and the saturation temperatures T_s for the melts are shown in Table IV.3. Due to its large ionic radius, Gd has been used to accomplish the LPE growth of single crystals on the larger lattice substrate as well as to decrease the saturation magnetization and stabilize its temperature dependence. In order to decrease the growth-induced

anisotropy of the Bi-Gd pair, Gd has been partially substituted by Lu. To study the changes in the uniaxial anisotropy, the Lu content has been increased in several steps, as indicated in Table IV.3. Ga has been used for diamagnetic dilution of Fe to further decrease the magnetic moment. The grown epitaxial layers were single crystals, and their composition has been controlled by the melt undercooling ΔT_s . Any additional phase formation in our samples has been ruled out based on both visual inspections of the samples under an optical microscope, as well as on X-ray measurements.

TABLE IV.3 Chemical analysis of epitaxial garnet films grown from (BiGdLu) melts. The melt saturation temperature, and the α and β parameters have been determined by a least squares fit of the growth rate to the van Erck's function.[84,85]

Melt	Film composition	x (atom/f.u.)	z (atom/f.u.)	α ($\mu\text{m}\cdot\text{K}/\text{s}$)	β (10^3 K)	T_s ($\pm 5^\circ\text{C}$)
A	$\text{Lu}_{0.3}\text{Bi}_x\text{Gd}_{2.7-x}\text{Fe}_{5-z}\text{Ga}_z\text{O}_{12}$	0.35-0.87	0.44-0.5	304	5.86	850
B	$\text{Lu}_{0.5}\text{Bi}_x\text{Gd}_{2.5-x}\text{Fe}_{5-z}\text{Ga}_z\text{O}_{12}$	0.44-0.93	0.46-0.52	312	6.67	830
C	$\text{Lu}_{0.65}\text{Bi}_x\text{Gd}_{2.35-x}\text{Fe}_{5-z}\text{Ga}_z\text{O}_{12}$	0.68-0.9	0.4-0.47	323	9.85	805
D	$\text{Lu}_{0.65}\text{Bi}_x\text{Gd}_{2.35-x}\text{Fe}_{5-z}\text{Ga}_z\text{O}_{12}$	0.7-1.08	0.41-0.48	346	9.06	796

The thickness of the films has been measured by using interferometric reflectance and has ranged between 1 and 6 μm . The growth rate has been calculated and is presented in Fig. 1 as a function of the growth temperature T_g . By using the van Erk theory of solubility and growth rate, the data have been fitted with a simple Arrhenius exponential dependence, as suggested by Fratello *et. al.*:^{62,84}

$$f = \alpha \cdot \left(\frac{1}{T_g} - \frac{1}{T_s} \right) \cdot \exp \left[-\beta \cdot \left(\frac{1}{T_g} - \frac{1}{T_s} \right) \right], \quad (4.19)$$

where f is the growth rate, and α and β are fitting parameters. The saturation temperatures of the melts have been determined by extrapolating the growth rate dependence to zero value and are shown in Table IV.3.

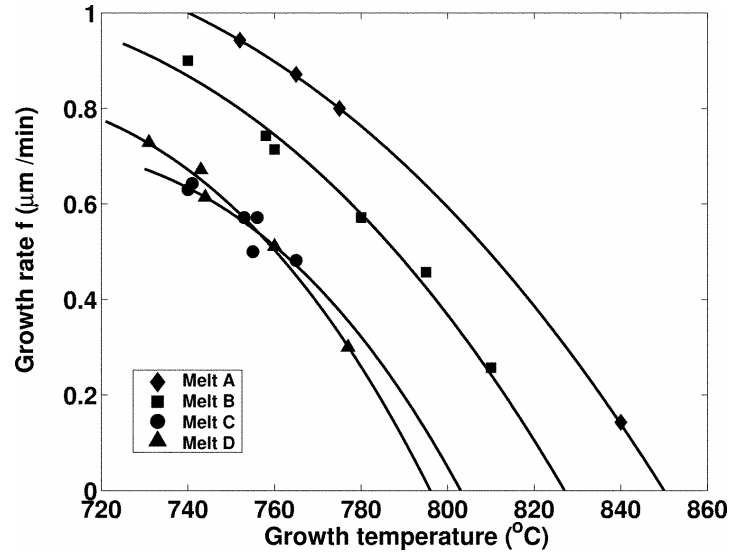


FIG. 4.17 Growth rate f vs. growth temperature for different melts. The experimental data are interpolated by using van Erk's model as described in the text.

The accurate fitting of the experimental data with the van Erk model suggests that the growth kinetics can be described as a diffusion process involving a single garnet particle,^{62,84} in spite of the fact that we have dealt with a multicomponent garnet system with two rare earths (Gd and Lu) and Bi competing for the dodecahedral site and Fe and Ga for the octahedral and tetrahedral sites. Since the garnet to flux ratio ($G/F = 0.18$), boron to flux ratio ($C_B = 0.11$), bismuth to flux ratio ($C_{Bi} = 0.39$) and the molar ratio of Fe and Ga to Lu and Gd in the melt ($R_1 = 25$) remained unchanged for melts **A**, **B**, and **C**, the growth rates at the same undercooling have been nearly identical, while the saturation temperature of the melts has shifted towards lower values with the increase in the Lu concentration in the melt.

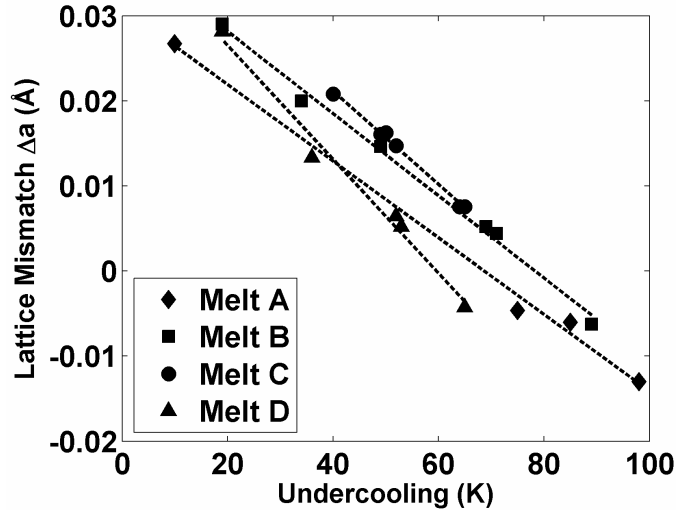


FIG. 4.18 Lattice mismatch vs. growth temperature for different melts. As the undercooling is increased, more Bi is incorporated in the films inducing an increase of the lattice mismatch.

The chemical composition of the garnet samples has been determined by electron probe microanalysis (EPMA). The data has been used to study the bismuth incorporation in the films. This has been accomplished by means of the Bi segregation coefficient (K_{Bi}) defined as:^{78,85}

$$K_{Bi} = \frac{y}{3-y} \frac{[RE]}{[Bi]}, \quad (4.20)$$

where y represents the number of Bi atoms in the chemical composition of garnet films, and $[RE]$ and $[Bi]$ are the rare-earth (Lu and Gd) and Bi concentrations in the melt, respectively. The dependence of K_{Bi} on melt undercooling is shown in Fig. 4.19, which indicates that K_{Bi} increases as more Gd is substituted by Lu, although the Bi concentration in the melt has been constant.

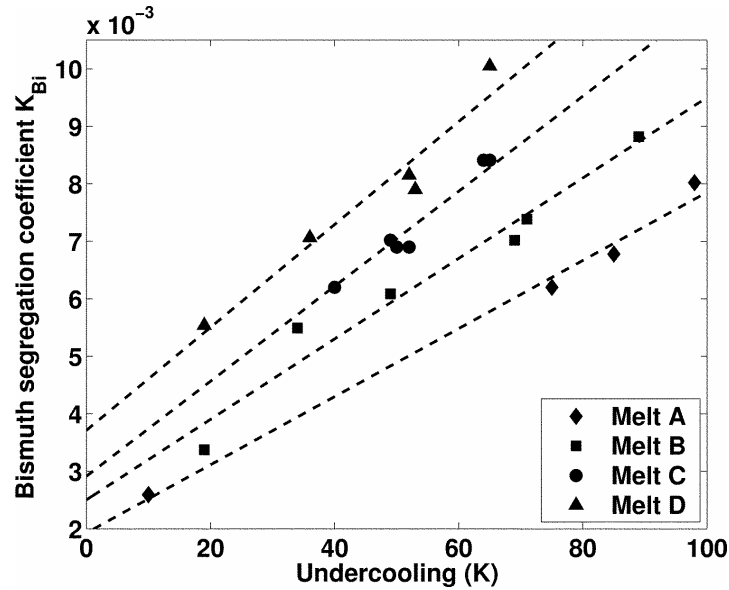


FIG. 4.19 Bismuth segregation coefficient K_{Bi} vs. melt undercooling for different Gd/Lu ratios in the melt. The lines are for guidance purposes only.

All these observations lead to the suggestion that in our (Bi-Gd-Lu) garnet system the growth process is mainly controlled by Gd. Moreover, since Lu and Gd both compete for the dodecahedral site, the increase in the Lu concentration in the melt decreases the Gd activity. This, in turn, enhances both the garnet solubility and the Bi segregation coefficient. At the same time, as expected, the saturation temperature of melt **D** is decreased by approximately 10°C since only the C_{Bi} ratio has been increased while the other molar ratios of melt C have remained constant.⁷⁸

Next the saturation magnetization M_s has been measured at 25°C by using a vibrating sample magnetometer (VSM). The values of M_s as a function of melt undercooling are plotted in Fig. 4.20. The accuracy of this measurement is about $\pm 20\text{G}$, and it is limited by the magnetometer accuracy as well as by the precision in determining the sample volume and uniformity ($\pm 5\%$). Since the diamagnetic Ga substitution has remained nearly the same and equal to 0.45 atoms/f. u., the increase

in M_s with undercooling for different melts can be attributed to the decrease in the Gd content due to increasing Bi incorporation. Fig. 4.20 shows that most of the garnet samples have compensation temperatures below room temperature. However, for melts with high Gd concentrations, (e.g. **A** and **B**), we have grown garnet samples that have the compensation temperatures above or close to the room temperature. Such films are not desirable for room temperature applications with stringent requirements of temperature stability.

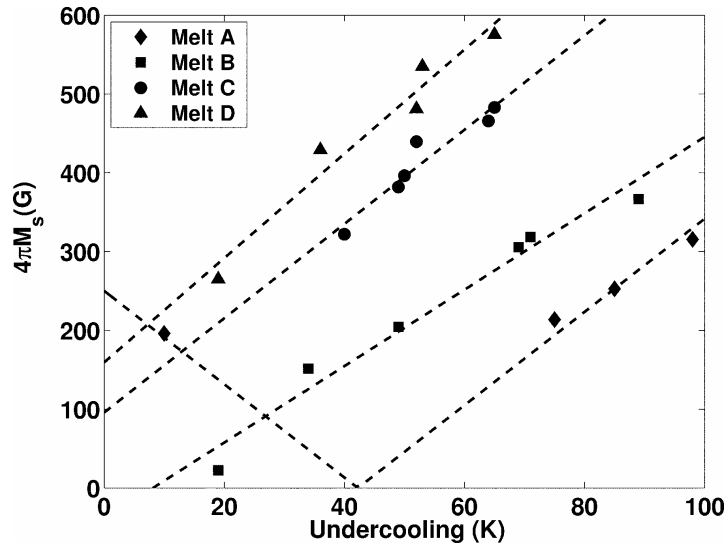


FIG. 4.20 Saturation magnetization vs. growth temperature for different melts. As the undercooling is increased less Ga and Gd are incorporated in the films, thus the M_s increases.

The effective uniaxial anisotropy field $H_{K_u,eff} = H_{K_u} - 4\pi M_s$ and the cubic anisotropy field $H_{K_1} = \frac{2K_1}{M_s}$ have been determined from ferromagnetic resonance (FMR) experiments as described in subchapter 4.3. The frequency of the microwave field has been kept constant and the value of the resonance field has been measured for different angles θ between the applied magnetic field and the film normal within the crystallographic [011] plane. The H_{K_1} and $H_{K_u}^{eff}$ fields have been determined by

numerical fitting of the data. From these anisotropy fields, the anisotropy constants have been calculated according to the following equations:

$$K_1 = M_s \cdot H_{K_1} / 2 \text{ and } K_u = M_s \cdot (H_{K_u} + 4\pi M_s) / 2. \quad (4.21)$$

The uniaxial anisotropy is actually the sum between a stress-induced part and a growth-induced part. To determine the growth-induced part, the stress-induced anisotropy had to be calculated and subtracted from the value of K_u . The stress-induced part K_u^λ depends on the magnetostriction coefficient λ_{100} and on the lattice mismatch Δa_\perp between the film and the substrate. For $(\text{BiGdLu})_3(\text{FeGa})_5\text{O}_{12}$ compositions, the magnetostriction coefficient λ_{100} at room temperature has been interpolated by using the values for $\text{Gd}_3\text{Fe}_5\text{O}_{12}$ ($\lambda_{100} \approx 0$) and $\text{Lu}_3\text{Fe}_5\text{O}_{12}$ ($\lambda_{100} \approx -1.25 \cdot 10^{-6}$).⁸⁶ Then, the effect of Bi and Ga substitutions on the magnetostriction values has been then taken into account by using the technique outlined in Hansen *et. al.*⁸⁷ The result of the calculation of λ_{100} is shown in Fig. 4.21 below.

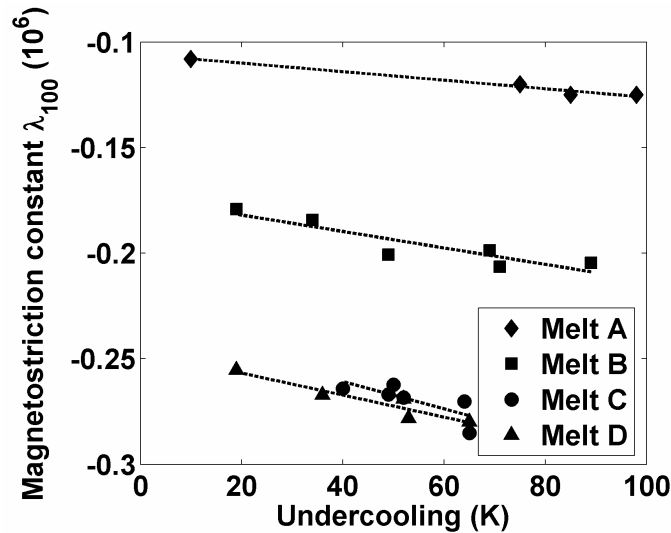


FIG. 4.21 Magnetostriction constant vs. growth temperature for different melts according to [86].

The calculated growth-induced anisotropy $K_u^g = K_u - K_u^\lambda$, where $K_u^\lambda = -\frac{3}{2} \frac{E}{1+\nu} \frac{\Delta a_\perp}{a_s} \lambda_{100}$ is shown as a function of undercooling in Fig. 4.22. With the increase in Lu incorporation from 0.3 to 0.7 atoms/f.u., the slope $dK_u^g/d(\Delta T_s)$ changed from about $50 \text{ erg/cm}^3 \text{ K}$ to about $-60 \text{ erg/cm}^3 \text{ K}$. At the same time, the extrapolated values of K_u^g at $\Delta T_s = 0$ (equivalent to $f = 0$) continually decreased from 3200 erg/cm^3 for melt A down to 1300 erg/cm^3 for melt D. This decrease combined with the negative slope of K_u^g yielded samples with the desired in-plane magnetization state. It is worthwhile to mention that some groups reported that the linearly extrapolated values of K_u^g at zero growth rate are equal to zero, while the linear extrapolation of our experimental observations leads to non-zero positive values of K_u^g . A possible explanation of this discrepancy can be based on the fact that the chemical analysis of our samples indicate that at very small growth rates, the garnet films would have the composition $(\text{GdLu})_{3-x}\text{Bi}_x(\text{FeGa})_5\text{O}_{12}$ with x increasing from 0.3 to 0.55 atoms/f.u. for melts A to D. Since Bi incorporation induces a strong positive growth anisotropy, this would explain why our extrapolated values of K_u^g at zero growth rates are shifted towards positive values.

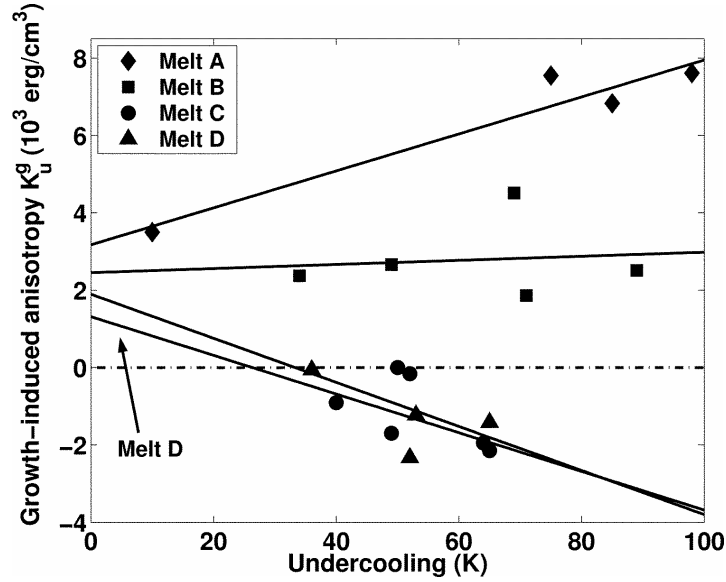


FIG. 4.22 Experimental growth-induced uniaxial anisotropy K_u^g as determined by FMR measurements vs. melt undercooling.

For the cubic anisotropy, the measured values of K_1 are negative, which is characteristic of (Lu,Gd)-substituted garnets. In contrast with the strong variability of K_u^g as a function of undercooling, the changes in K_1 are appreciably smaller and $dK_1/d(\Delta T_s)$ is between 0 and $-30 \text{ erg/cm}^3 \text{ K}$. As previously reported, K_1 has a very small dependence on the Bi substitution and a stronger dependence on diamagnetic substitutions.⁸⁷ Since the Ga content is practically the same in our samples, the observed changes in the cubic anisotropy can only be attributed to the decrease in Gd content simultaneously with the increase in Bi incorporation.

The Faraday rotation θ_F has been measured at 633 nm with applied fields up to 2500 Oe by using the in-house optical hysteresisgraph. In order to obtain the Faraday rotation associated only with the Bi content, the Faraday rotation per unit length was corrected for Ga incorporation using the method proposed by Helseth *et. al.*²³ The results are plotted as a function of the melt undercooling in Fig. 4.23 It can be seen

that for the same undercooling the magneto-optical activity has been increased by more than 50% due to the increase in Bi incorporation. According to our data, θ_F is linearly proportional to the Bi incorporation and for different melts, the measured contribution of Bi to the rotation $\Delta\theta_F/y$ ranged between -22580 and -26450 deg/cm, comparable with results previously reported in Refs. 82 and 83.

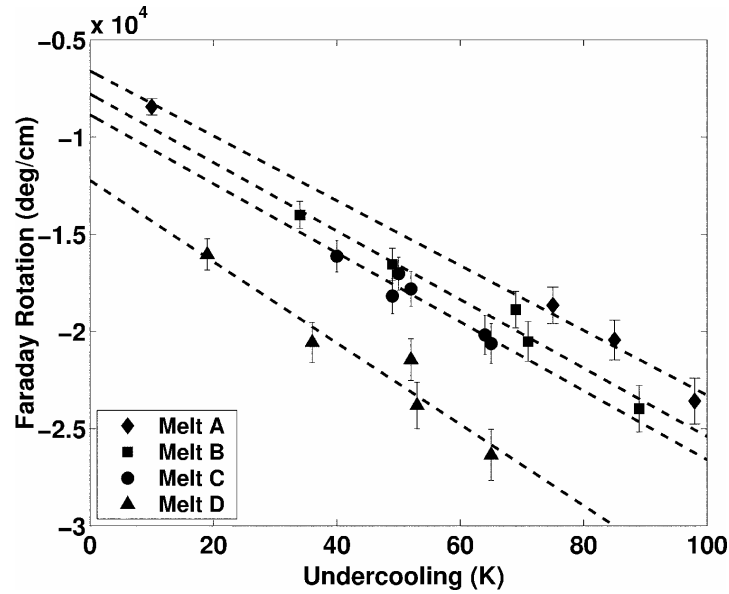


FIG. 4.23 Faraday rotation per unit length vs. undercooling at $\lambda=633$ nm and $T=295$ K.

4.5.2 Influence of the substrate rotation (RPM) on single crystal properties

Another method to control the final properties of epitaxial garnet films, besides melt chemistry and undercooling, is to use the rotation rate of the substrate. In the past Giess *et al.*⁸⁸ and Ghez *et al.*⁸⁹ have studied the effects of substrate rotation rate on growth rate and lattice mismatch for (EuY)FeGa garnet films, but the effects on optical properties were not considered. We have focused on investigating the rotation rate effects on the properties of (Bi:Lu)FeGa garnets, including also how it affects the optical properties that would be of interest for thin film magneto-optic waveguides.

The composition of the LPE films in our research was $\text{Bi}_x\text{Lu}_{3-x}(\text{FeGa})_5\text{O}_{12}$, with a small amount of lead from the flux and platinum from the crucible also incorporated into the films. The substrates used were $\text{Gd}_3\text{Ga}_5\text{O}_{12}$ (GGG) wafers, with a diameter of 25 mm, oriented in the $\langle 111 \rangle$ direction. The films were grown on only one side of the wafer. The flux used for the melt was $\text{PbO-Bi}_2\text{O}_3$. The melt saturation temperature was approximately of 800 °C and the undercooling for growing the films was 28 °C. This amount of undercooling did not produce spontaneous nucleation on the melt surface during growth. The temperature was controlled to within 1 °C during growth. Growth times were kept fixed at 7 min for all films.

The rotation rate ω has a strong effect on the growth rate and the lattice mismatch for the particular melt system studied. We were able to almost double the growth rate by increasing ω from 25 to 256 rpm, as can be seen in Fig. 4.24. The results also show the linear behavior of the growth with $\omega^{1/2}$ which is consistent with the model described by Ghez *et al.*⁸⁹ Although, as it was discussed by Giess and Kuptsis,⁹⁰ this $\omega^{1/2}$ dependence is not expected to follow to lower rotations rates (25 rpm), where the interfacial growth kinetics leads to a different growth rate - $\omega^{1/2}$ dependence.

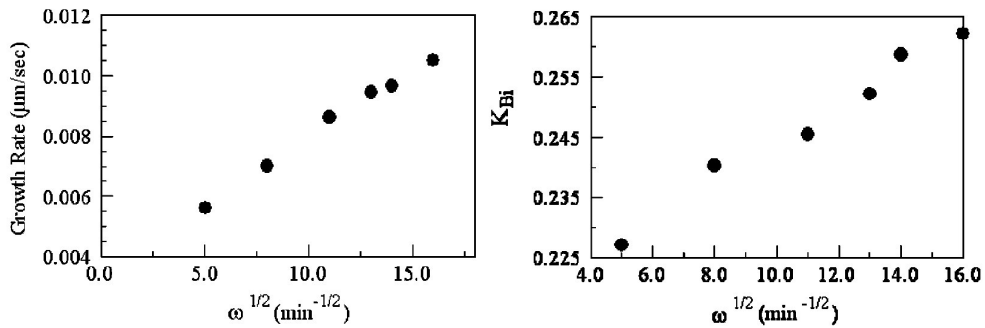


FIG. 4.24 Growth rate vs. rotation rate (a) and Bi-segregation coefficient (defined in Eq. 4.20) vs. rotation rate, at the same melt undercooling.

One further aspect about the use of ω to control garnet growth parameters, is that for very high rotation rates a limit is approached where the growth rate starts to decrease. We have observed this with some of our melts, and Giess *et al.*⁹⁰ have mentioned that the probable cause for this decrease is the transition from laminar to turbulent flow close to the growth interface.

Another parameter of interest in the dynamics of film growth is the relative concentration of the different components in the film compared to the concentration in the melt. Similarly to the case of growth rate, the curve for the bismuth segregation coefficient $K_{Bi} = \frac{y}{3-y} \frac{[RE]}{[Bi]}$, where y represents the number of Bi atoms in the chemical composition of garnet films, and $[RE]$ and $[Bi]$ are the Lu and Bi concentrations in the melt respectively,⁹¹ shows a close to linear behavior with the square root of the rotation rate. To try to explain this dependency we assumed that K_{Bi} follows the basic behavior for the segregation coefficient given in the classic Burton–Prim–Slichter-(BPS) paper.⁹² For our particular case we substitute in the model the concentration of Bi at the liquid-crystal growth interface divided by the concentration in the liquid bulk away from the interface (K^*) by a linear function of the fluid velocity v inside the viscous boundary layer. This velocity, as derived by Ghez *et al.*⁸⁹ is itself a function of $\omega^{1/2}$, the fluid parameters, such as kinematic viscosity and diffusion coefficient and the difference $(C_L - C_e)$, where C_L is the concentration of Bi in the bulk and C_e is the concentration at the growth interface at equilibrium. It can be shown that with this assumption for K^* ($K^* = K' \omega^{1/2}$), the relative distribution for Bi is given by:

$$K_{Bi}(\omega) = \frac{K' e^{(C_L - C_e)/\rho} \omega^{1/2}}{1 + K' (e^{(C_L - C_e)/\rho} - 1) \omega^{1/2}} \quad (4.22)$$

The constant K' depends on the fluid parameters and an empirical factor. For most practical situations, as reported by Giess and Kuptsis,⁹⁰ the exponent $(C_L - C_e)/\rho$ is in the range of 10^{-4} – 10^{-5} . Then, the second term in the denominator is small and can be dropped, which results in $K(\omega)$ being proportional to $\omega^{1/2}$.

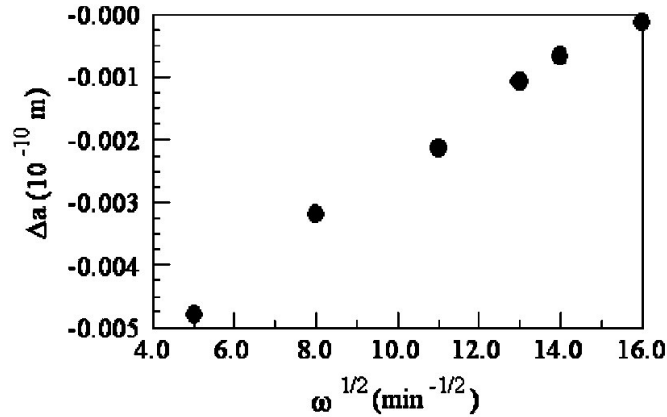


FIG. 4.25 Lattice mismatch vs substrate rotation rate.

Figure 4.25 shows the decrease in the lattice mismatch as we increase ω . This dependency of the lattice mismatch with rotation rate follows the change with $\omega^{1/2}$ of the concentration for the different elements in the film. In the case of Bi, being a larger atom than Lu, its increase in concentration also contributes to a smaller lattice mismatch. On the other hand, the decrease in Ga concentration increases the lattice mismatch. From the results in Table IV.4, we can see that the Bi concentration change is larger than the one for Ga, and thus Bi will have a more pronounced effect on the lattice mismatch variation. One advantage of being able to reduce the lattice mismatch with the rotation rate is that it brings the film from tension to zero mismatch helping to oppose the uniaxial anisotropy and, consequently, to increase the

possibility of an in-plane domain orientation which is fundamental for waveguide devices.

TABLE IV.4 Microprobe analysis of Bi:LuFeGa garnet films for different substrate rotations rates (in atoms per formula unit).

$\omega^{1/2}$	Lu	Bi	Pb	Fe	Pt	Ga
5	2.322	0.652	0.016	3.923	0.053	1.024
8	2.283	0.689	0.017	3.936	0.050	1.014
11	2.268	0.704	0.028	3.946	0.051	1.002
13	2.249	0.724	0.027	3.949	0.048	1.002
14	2.231	0.743	0.026	3.953	0.048	0.999
16	2.225	0.754	0.021	3.956	0.047	0.997

In the past Tolksdorf *et al.*⁹³ mentioned the case of fabricating waveguides made of magneto-optic thin film garnets using different undercoolings for the different layers. But, as they also mentioned, the need to make successive dips to deposit the different layers was prone to create defects and nonuniformities due to flux residues. These issues can be overcome by using rotation rate as a method of growing layers with slightly different indices of refraction required for waveguiding. The index of refraction variation with rotation rate is shown in Fig. 4.26 (a) at 1550 nm. We can see a variation of about 1.6×10^{-2} or 0.7% between the films made at 25 rpm and 256 rpm. This variation is large enough to allow a wide range of sizes of single-mode waveguides.

We have also measured the Faraday rotation and the saturation magnetization of the epitaxial films. The results, shown in Fig. 4.26 indicate the same linear dependence with $\omega^{1/2}$ because both Bi and Ga incorporation change linearly with $\omega^{1/2}$.

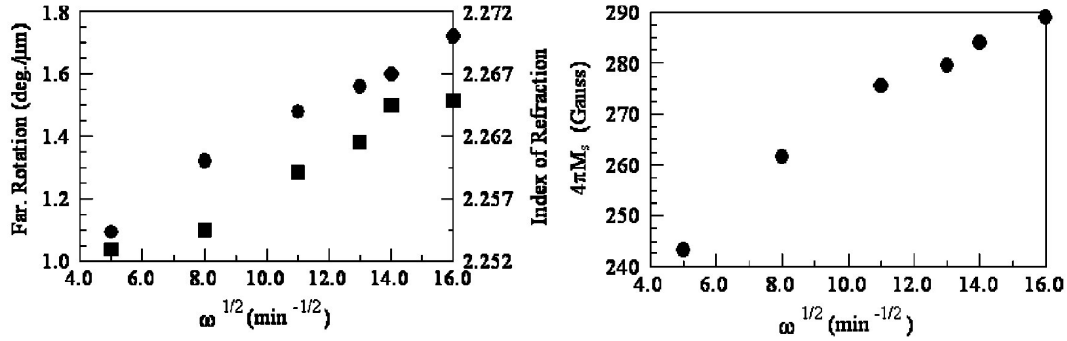


FIG. 4.26 Faraday rotation (squares) and index of refraction (circles) vs. substrate rotation rate (a), and magnetization vs substrate rotation rate (b).

Finally, in Fig. 4.27 and 4.28 the optical microscope images are shown for epitaxial films grown at different RPM on substrates with different orientations. Although, as we have seen above, many material properties are changing simultaneously with RPM, optical observation of the samples indicate the final result of the energy balance minimization on magnetization equilibrium positions. These optical images show that the domain structure of the epitaxial films can be greatly affected by RPM for both (100) and (111) substrate orientations.

For the <100> orientation shown in Fig. 4.27, it can be seen that at low rotation rates the sample presented stripe domains. This is a clear indication of a positive uniaxial anisotropy, which stems from a low Bi substitution level. This translates into a small number of (Bi-Lu) pairs and usually tension in the epitaxial films (thus the cracks in the image). By increasing the rotation rate of the substrate to 196 RPM, the Bi substitution is enhanced, thus the number of (Bi-Lu) pairs increases, in parallel with a shift of the epitaxial film from the tension state to compression. Due to the fact that on (100) oriented substrates the Bi-Lu pairing induces a negative growth anisotropy, the total uniaxial anisotropy becomes negative and the film presents large domains, characteristic to in-plane magnetization.

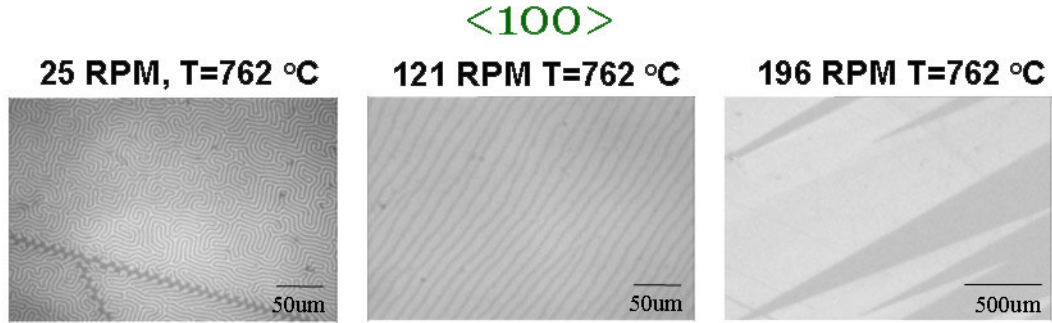


FIG. 4.27 Optical microscope images showing the change in magnetization equilibrium position in epitaxial films grown on $\langle 100 \rangle$ -oriented substrates for different increasing RPM. At the highest RPM, the Bi incorporation is largest, thus the sample has in-plane magnetization.

For the $\langle 111 \rangle$ orientation shown in Fig. 4.28, the situation is similar. At low rotation rates, the sample presented a pattern of bubble domains. This is a clear indication of a strong positive uniaxial anisotropy, due to a small number of (Bi-Lu) pairs and tension in the epitaxial film. By increasing the rotation rate of the substrate to 256 RPM, the Bi substitution is enhanced. But unlike the case of $\langle 100 \rangle$ oriented substrates discussed previously, it can be seen that the stripe domains are still present in the film grown at the highest RPM. This is because in $\langle 111 \rangle$ films, Bi-Lu induces a slightly positive growth anisotropy that the stress-induced uniaxial anisotropy is not large enough to overcome.

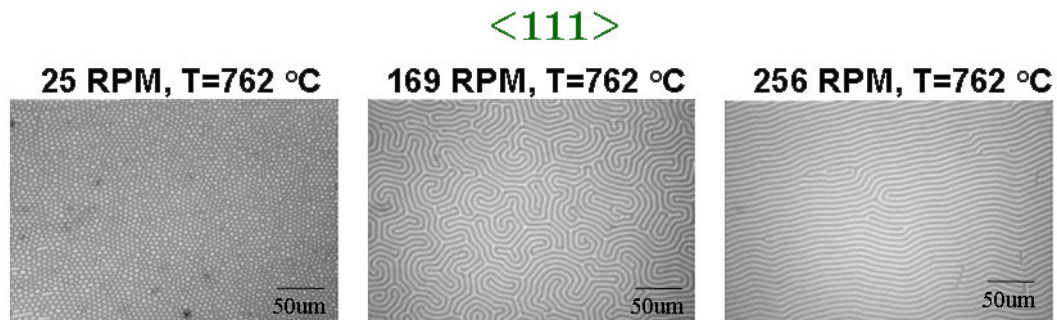


FIG. 4.28 Optical microscope images showing the change in magnetization equilibrium position in epitaxial films grown on $\langle 111 \rangle$ -oriented substrates for different increasing RPM. At the lowest RPM, the Bi incorporation is smallest, the uniaxial anisotropy is positive and the film presents bubble domains. As the RPM is increased, the Bi-Lu pairing reduces this positive growth anisotropy, but not enough to yield samples with in-plane magnetization.

Chapter 5: Magnetic field optical sensors based on garnet thin films

In this chapter, three types of sensors will be discussed: magnetic field sensors based on single and multilayer waveguide devices, and magneto-optical imagers, a type of sensors used to image the fringing fields of magnetic patterns. The organization of the chapter proceeds as follows. First, the principle of operation of magneto-optical sensors based on garnet thin films is presented. Then, the design of waveguide devices and the experimental measurement setup are described in detail. The discussion continues with describing magneto-optical imagers that allow imaging magnetic patterns with sub-micron resolution. Next, optical sensors based on single layer garnet thin films are described along with noise measurements performed on actual devices. The discussion of sensors based on multi-layer garnet films is preceded by describing a method that allows simultaneous measurements of layer specific material properties for every layer in such a multi-layer garnet structure. The chapter ends with considerations on the thermal stability of the sensors and on-chip integration capabilities and methods.

5.1 Principle of operation of the magneto-optical sensors

The proposed extrinsic magnetic field sensor is based on the Faraday effect in garnets. For uniformly magnetized garnets, the bulk Faraday rotation per unit length is related to the angle between the magnetization and the light propagation direction by the following equation:

$$\theta_F = V \cdot \vec{M} \cdot \frac{\vec{k}}{|\vec{k}|}, \quad (5.1)$$

where V is the garnet's Verdet constant, \vec{M} is the magnetization vector, and \vec{k} is the propagation vector of the light. The variation in the Faraday rotation as the function of the angle between \vec{M} and \vec{k} can be optically measured and used for magnetic field sensing applications as demonstrated below.

As discussed in Chapter 2, the initially proposed designs of magneto-optical sensors were based on garnets with out-of-plane magnetization with light propagating perpendicular to the sample. This is because such films have the lowest saturation field and thus the highest field sensitivity. As discussed in Chapter 2, the problem with them is two-fold. First, the domain structure creates a diffraction grating that destroys the linearity of the sensor response. Second, the sensor being based on domain structure expansion under applied fields is affected by the coercive field of the samples, a coercive field that can be sometimes many orders of magnitude larger than the maximum claimed sensitivity. Hysteretic effects become equally important.

Garnets with in-plane magnetization can also be used for sensing. The probing light beam is again perpendicular to the sample. Initially, there was knowledge that allowed the growth of in-plane fields with low saturation fields (a few Oe), thus high sensitivity, but after the collapse of bubble memory industry, this knowledge has been lost.⁹⁴ Recently, the in-plane garnet films reported in the literature and grown in our own facility have perpendicular saturation fields on the order of hundreds of mT (thousands of Oe) and consequently very low sensitivity. There is hope that by using special substrate orientations like (210) or (211), garnet films can be grown with in-

plane magnetization and low saturation fields, unlike in the case of more common (100) and (111) oriented substrates.⁹⁵

In the following subchapters, magnetic sensors for two different applications will be described in detail. One direction deals with imaging applications. In this case, the goal is to image the fringing fields of 2D magnetic patterns without using scanning techniques. The second direction is using waveguide like structures as sensing elements in optical fiber magnetic field sensors. In the former case the ideal device is a single-crystal thin epitaxial garnet film, while in the latter case single- or multi-layered structures are more desirable.

The designs of our exemplary sensor described herein are based on the peculiar magnetic properties of garnet films. For example, even films that are the magnetically hardest in the perpendicular direction (i.e., with high perpendicular saturation fields) often exhibit low in-plane saturation fields (as will be shown below). The in-plane saturation field is often below 20mT and sometimes is below 1mT. Hence, if a light beam is sent through the film parallel to the hard axis of the material, the projection of the magnetization on this in-plane hard axis can provide very good magnetic field resolution.

For the extrinsic sensor, our proposed sensing element is a waveguide obtained from a thin epitaxial garnet film with giant magneto-optical effect grown on a (100) oriented substrate. The Faraday effect is not simply characterized as a rotation of the polarization plane of the light, but rather as a mode conversion. The phenomenon of mode conversion refers to the transfer of energy between two orthogonal propagating modes in a gyrotropic waveguide and has been discussed in detail described in

Chapter 2.3. It can be shown that if only the fundamental TE mode of the waveguide is excited, the fraction of the power that is converted into the fundamental TM mode is given by the mode conversion efficiency:⁴¹

$$F = \frac{1}{1 + (\Delta\beta/2\kappa)^2} \sin^2\left(\sqrt{\kappa^2 + (\Delta\beta/2)^2} \cdot z\right) \quad (5.2),$$

where z is the distance along the propagation direction, $\Delta\beta$ is the difference between the propagation constants of the fundamental TE and TM modes and κ is the coupling constant, which is equal to the Faraday rotation in the bulk case. It is then obvious that in order to obtain a good conversion efficiency, $\Delta\beta$ has to be much smaller than κ . This can be achieved by using thicker waveguides or by reducing the difference in the index of refraction between the garnet film and the cover as well as the substrate.

It can be seen from Eqs. (5.1) and (5.2) that in order to fully characterize the sensor response, the Faraday rotation must be determined. This implies that the equilibrium position of the magnetization as a function of applied fields has to be known for every value of the applied field. In micromagnetics, the magnetization equilibrium states realized under applied magnetic fields are derived from the minimum of the free energy density, which for (100)-oriented garnets can be written as follows:

$$f = -\vec{M} \cdot \vec{H} + K_u \sin^2(\theta) - 2\pi M_s^2 \cos^2(\theta) + K_1 [\sin^4(\theta) \sin^2(\varphi) \cos^2(\varphi) + \sin^2(\theta) \cos^2(\theta)], \quad (5.3)$$

where M_s is the saturation magnetization, K_u is the uniaxial anisotropy constant, K_1 is the cubic anisotropy constant and \vec{H} is the applied external magnetic field. The

angle θ is measured between the film normal and \vec{M} , while φ is the angle between the magnetization projection on the film plane and the planar [001] direction. In the case of negative values of K_1 (which is typical for garnet films) and in the absence of external magnetic fields, the easy axes of the magnetization are defined by the angles $\varphi_n = n \frac{\pi}{4}$, ($n = 1, 3, 5, 7$). In addition, if the sample has planar magnetization ($\theta = \pi/2$), the response of \vec{M} to applied in-plane magnetic fields depends only on the values of K_1 , M_s and the direction φ_H of the applied field with respect to the [001] direction.

5.2 Design of the optical waveguide and experimental setup

Here only the case of the waveguide garnet structures is discussed. The imager applications mentioned above are detailed in the following subchapter. The garnet waveguides are suggested as sensing elements in the design of magnetic field sensors. The structures can be etched out of liquid phase epitaxy (LPE) - grown iron garnet thin-films of composition $(\text{Bi,Lu})_3(\text{Fe,Ga})_5\text{O}_{12}$. The growth process and conditions to obtain such epitaxial films are described in detail in Chapter 3. These garnet films have negative uniaxial anisotropy, which results in an equilibrium position of the magnetization within the film plane.

The first step in designing the sensor is to identify the orientation of the in-plane easy axes of the material. This is accomplished by using the method outlined in Ref. 74. Next, rectangular slab waveguides oriented along the magnetic hard axis have been cut with different lengths from the sample. Finally, the front and end faces are

mechanically polished to enhance the optical coupling between the optical fiber used to deliver the light and the waveguides.

In order to measure the optical response of the sensor, the setup shown in Fig. 5.1 has been used. The sample has been placed inside a 5 cm diameter Helmholtz coil generating low frequency magnetic fields with amplitudes up to 30 mT. The waveguide has been butt-coupled with an optical fiber providing linearly polarized light of $\lambda=1370$ nm from a semiconductor laser. This wavelength lies well above the threshold of the garnet absorption which is near 1 μm , yet still in the region where the specific Faraday rotation is sufficiently high.⁹⁶ The direction of light propagation has been chosen to be parallel to the direction of the applied magnetic field. At the waveguide output, a microscope objective has been used to collect the light and focus it on a GaAs photodiode. The response of the detector has been recorded by using a digital oscilloscope.

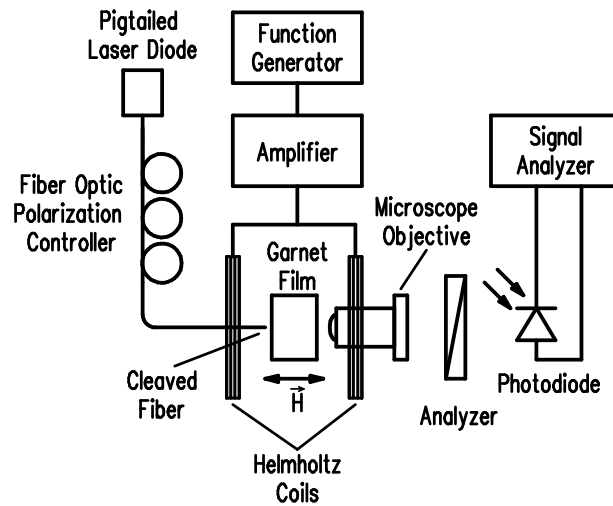


Fig. 5.1 Schematic of the experimental setup used to measure the response of the sensor.

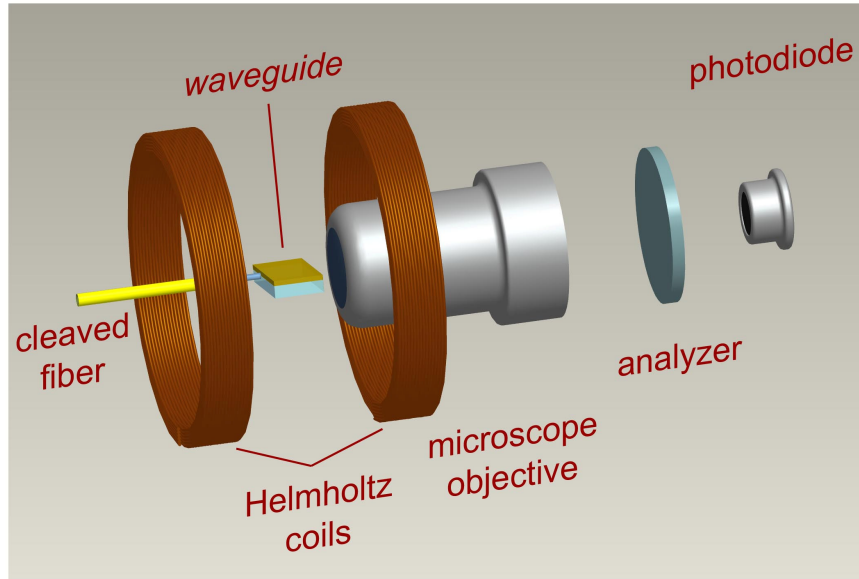


Fig. 5.2 Experimental Setup used to measure the response of garnet-based waveguide magnetic field sensor. TE-polarized light of wave-length $\lambda=1370$ nm is butt-coupled from a cleaved fiber into the garnet film. An ac magnetic field is generated by a pair of Helmholtz coils and the emerging TM-polarized light component is detected with a photodiode.

5.3 Optical sensors based on single layer garnet films

5.3.1 Magneto-optical indicators

In this subchapter will be discussed the application of Bi-substituted garnets as sensing elements for imaging purposes. Magneto-optical imagers based on epitaxially grown iron garnet films provide the possibility to detect in real time two-dimensional magnetic patterns, such as magnetic flux in superconductors, magnetic tracks on audio and video tapes, security features on bank notes, and currents in microelectronic circuits.^{53,79,97} In this sense, these garnet films can be used for direct (non-scanning) imaging of two-dimensional magnetic patterns. Unlike scanning techniques, the spatial resolution is limited by the optical diffraction limit and not by the size or step of the scanning probe.

The results presented herein were obtained using thin garnet films of generic composition $(\text{BiGdLu})_3(\text{FeGa})_5\text{O}_{12}$ grown by liquid phase epitaxy (LPE) on (100) oriented Ca, Mg and Zr substituted gadolinium gallium garnet (CMZ-GGG) substrates with an expanded lattice constant of $a=12.498\text{\AA}$. Two of the samples were films with out-of-plane magnetization, while the third one had in-plane magnetization. The properties of interest are shown in Table V.1. As discussed in Chapter 4.5.1, these films are single-crystal Bi-substituted ferrite garnets exhibiting giant Faraday effect. A polarized light microscope setup as the one in Fig. 4.9 has been used together with these films to image magnetic patterns on audio and digital data storage (DDS) tapes. For imaging of analog recordings, garnets with in-plane magnetization show great promise because they offer a true gray-scale imaging and the potential to calibrate the imaging system to actually determine the values of the imaged magnetic fields. Their spatial resolution is limited by the thickness of the MOI layer.⁹⁸

For digital recordings, garnets with out-of-plane magnetization have more potential due to their superior contrast. In this case the major issue is the inherent stripe domain structure that overlaps the pattern to be imaged and limits the spatial resolution to a size comparable with the domain size.⁹⁹ It is worthwhile mentioning here that the resolution needed to image state of the art DDS tapes is below 400nm. The present paper describes a method of achieving submicron spatial resolution of magneto-optical imagers.

Bismuth substitution has been proposed to enhance the contrast and sensitivity of garnet-based MOIs, by increasing the Faraday rotation. However, Bi induces a strong

positive uniaxial anisotropy in films, thus yielding samples with out-of-plane magnetization. In this case, the garnets show the presence of magnetic domains that interfere with the image of the magnetic pattern.⁶⁴

The mechanism of magneto-optic image formation in domain films is displacement of the domain walls. The perpendicular component of the tape fringing field will increase the domain width of domains with magnetization orientation parallel to the fringing fields and decrease the domain width of the domains with antiparallel magnetization. If the magnetic field is smaller than the saturation field of the imaging film, the magnetic features will still be overlapped with the domain structure. If the magnetic features are much smaller than the magnetic domains, too much energy is needed to reduce the domain size of the garnet film and thus the magnetic pattern can not be resolved. If the domain period of the unbiased film is almost of the same size as the recording wavelength, nearly no additional energy will be required to change the domain size. Thus, the last case is the most desirable, especially for the case of digital data recordings.⁹⁹

The domain period can be calculated by minimizing the free energy density of a domain film as shown in Ref. [99]:

$$E = 8h \frac{\sqrt{AK_u}}{\lambda} + \frac{2\mu_0 M_s^2 \lambda}{\pi^3} \sum_{n=1,3,\dots} \frac{1}{n^3} \left[1 - \exp\left(\frac{-2n\pi h}{\lambda}\right) \right] \quad (5.4)$$

where h is the film thickness, A is the micromagnetic exchange constant, K_u is the uniaxial anisotropy constant, M_s is the saturation magnetization, and λ is the domain period. As Bi incorporation is increased, the uniaxial anisotropy becomes larger and

consequently the domain size is increased, thus limiting the spatial resolution of the MOI.⁶⁴

In films with in-plane magnetization, the image formation takes place by uniform rotation of the magnetization out of the plane due to the fringing field of the samples to be imaged. The sensitivity of a garnet film with in-plane magnetization is given by:⁵³

$$S = d\Theta_F / dH_z = \Theta_F^{sat} / H_a, \quad (5.5)$$

where Θ_F^{sat} is the maximum Faraday rotation of the film and H_a is the anisotropy field. In order to obtain a high sensitivity, a large Faraday rotation and a small anisotropy field are necessary. For in-plane films the anisotropy field is decreased by reducing the absolute values of K_u and M_s . Unfortunately, the latter also decreases the Faraday rotation and therefore the contrast.

The spatial resolution of MOIs using in-plane garnet films is limited by the

Table V.1 Properties of in-house grown MOI films

Sample	h_0 (μm)	θ_F (deg/cm)	$4\pi M_{sat}$ (G)
1	6.1	-23000	620
2	4.6	-17000	360
3	5.1	-18500	330

* h_0 represents the initial thickness before etching.

thickness of the sample. In order to achieve resolutions of 500 nm and less, the thickness has to be reduced to similar values. Since the decrease in the thickness means a decrease in the maximum Faraday rotation, this will reduce the film sensitivity.

LPE can yield samples with a variety of properties by controlling the growth conditions and melt compositions. Unfortunately LPE is a complex process and

identifying the optimum composition suitable for MOI applications can be an even more complicated task. This is because in LPE, as discussed in Chapter 4.5.1 many properties of the epitaxial films grown from the same melt but under different growth conditions will simultaneously change the Faraday rotation, the cubic anisotropy, the saturation magnetization and the uniaxial anisotropy.

In order to speed up the process of achieving MOIs with submicron size, and to add an additional degree of flexibility to the classical LPE process, we proposed a post-growth process that allows fine tuning of only one property of interest (in our case the stripe width) without causing any additional changes in other parameters of the film. This method is based on growing epitaxial garnet layers with Faraday rotation as high as possible and a desired saturation magnetization. As mentioned above, such Bi- substituted garnet samples are very likely to have out-of-plane magnetic domains. Subsequently, these samples will be etched in hot phosphoric acid, thus reducing their thickness. According to Eq. (5.4), when the thickness is reduced, the domain size will decrease accordingly. In addition, the stripe domain widths can be continuously decreased to the required values without growing additional samples. Since the etching time can be precisely selected, this control on the stripe domain widths can be quite effective.

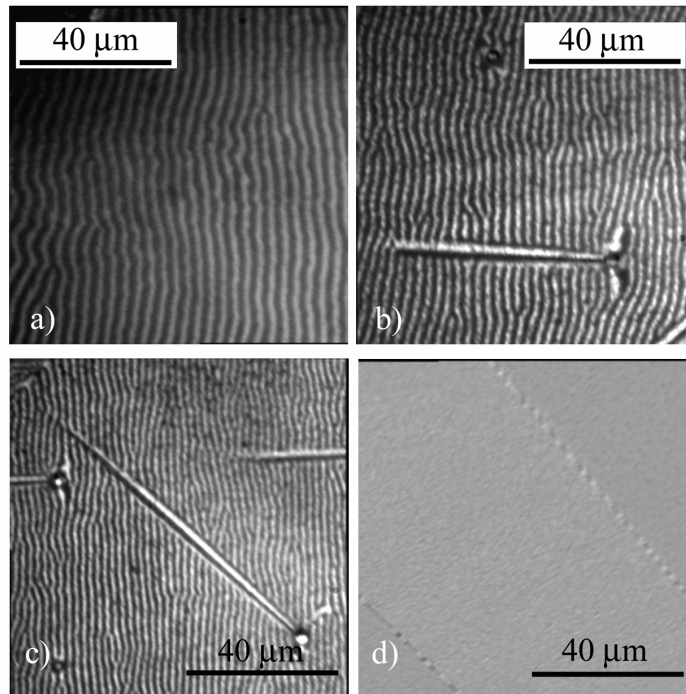


Fig. 5.3 Changes in magnetic domain size in epitaxial garnet film with out-of-plane magnetization after etching in phosphoric acid: (a) initial; (b) after $t=2$ min; (c) after $t=3$ min and (d) after $t=4$ min.

In order to study the influence of the film thickness on the domain width, the garnet films were etched in hot phosphoric acid for different periods of time, and λ was measured optically. Fig. 5.3 shows the change in domain width with etching time for sample 1. Initially, the period of domains was $1.78 \mu\text{m}$ for a film thickness of $6.1 \mu\text{m}$. As seen from Fig. 5.3, subsequent etching steps reduced the domain width so that when the film thickness was of $1.1 \mu\text{m}$, the stripe domains became practically undetectable under the optical microscope (Fig. 5.3(d)). The corresponding DDS tape images for Case (a) and (d) are shown in Fig. 5.4, and Fig. 5.5 respectively. A drastic increase in spatial resolution was evident, because in Fig. 5.5 one could easily distinguish data recordings with bit size of about $0.4 \mu\text{m}$. This enhancement in the

spatial resolution was obtained by using the same sample, without the need for growing additional samples.

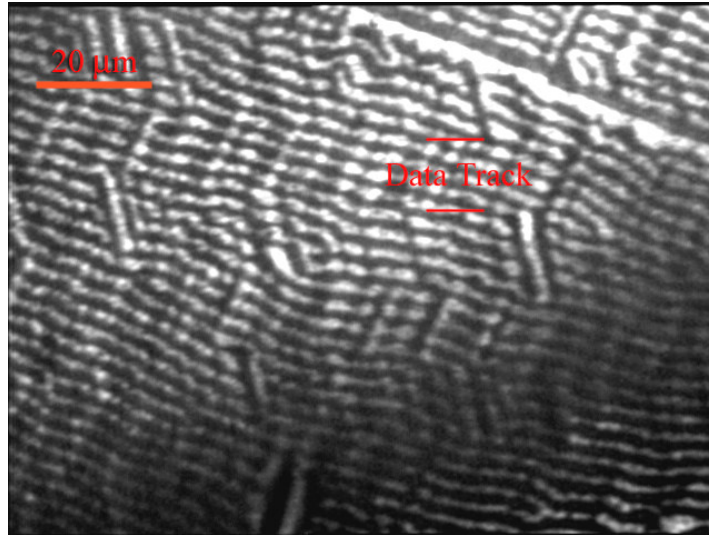


Fig. 5.4 Magneto-optic imaging of data tracks from a DDS tape using sample 1. Initially, the sample shows large domains that overlap the pattern to be imaged.

Similar experiments were performed for sample 2. The change of λ with the sample thickness for both of these out-of-plane films is presented in Fig. 3. In order to estimate the highest theoretical spatial resolution that can be obtained by using this etching method, we have fitted the experimental data by a theoretical curve obtained from the minimization of Eq. (1). Here, K_u has been measured using ferromagnetic resonance (FMR), and M_s has been obtained from vibrating sample magnetometer (VSM) measurements. For every sample, the only fitting parameter was the exchange constant A . For sample 1 we have obtained a best fit for $A = 11 \cdot 10^{-12} \text{ J/m}$, while for sample 2 a fit was not as good.

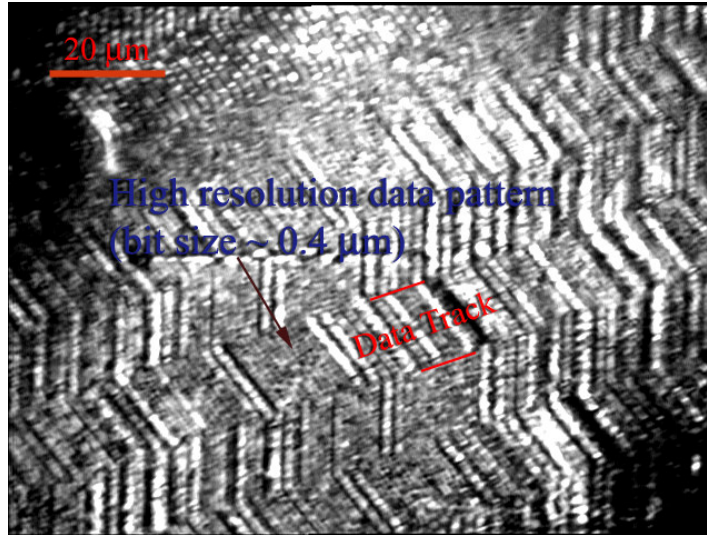


Fig. 5.5 Magneto-optic imaging of data tracks from a DDS tape using sample 1. After etching the film for 4 min, the domain size is reduced and submicron resolution can be achieved.

It is worthwhile to mention here that the effect of increasing the magnetization of garnet films is the decrease in stripe domain width. This means that the same spatial resolution can be obtained by using domain films with larger M_s . At the same time, this larger M_s will increase the Faraday rotation, consequently enhancing the image contrast.

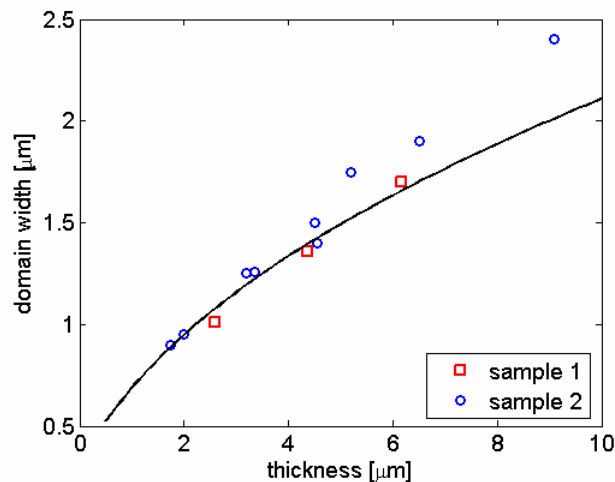


Fig. 5.6 Theoretical simulation (continuous line), and experimental data (points) showing the change in domain width with sample thickness. The experimental points have been obtained by chemically etching the samples, and measuring the domain width for different etching times.

DDS tapes have also been imaged using thin garnet films with in-plane magnetization. The advantage of these MOIs is that a true gray scale image is obtained and that no domain artifacts appear in the demagnetized areas. Unlike films with out-of-plane domains, the disadvantage of in-plane imagers is that in order to increase the spatial resolution, the thickness has to be proportionally decreased. Thus, for a resolution of 500 nm or less, the thickness has to be reduced to 0.5 μm or less which will greatly reduce the Faraday rotation and consequently the image contrast. It is also useful to discuss that usually the growth of out-of-plane garnet films is more straightforward task than the growth of in-plane garnet films. This fact combined with the controllability of stripe domains width in out-of-plane garnets through etching makes them the garnets of choice for MOI applications.

5.3.2 Noise and sensitivity measurements for sensors based on single layer garnet thin films

The previous subchapter discussed the case of a single layer garnet sensor used for 2D imaging of fringing magnetic fields. In this subchapter, we will analyze the case of waveguide garnet as sensing elements in extrinsic sensors for measuring magnetic fields.

Initially, we have focused our efforts towards creating a sensing element in the form of a slab of single-layer garnet material. In this case, as discussed in Chapter 2.3, it is possible to completely characterize the wave propagation through the gyrotropic waveguide starting from the purely dielectric waveguide (with dielectric properties identical to those of the garnet layer, but without magneto-optical activity), and then considering the magneto-optical activity as a small perturbation. For the

typical garnet slab structure, the corresponding dielectric slab waveguide is shown in Fig. 5.7, where the index of refraction for the substrate is 1.95 and for the cover (air)

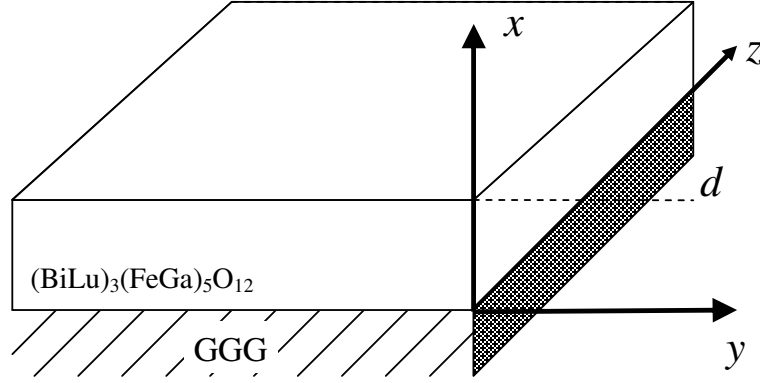


Fig. 5.7 Single-layer garnet slab waveguide used as sensing element.

is 1. The index of refraction for the guiding garnet layer can be controlled by growth conditions, as discussed in Chapter 4.5.

With the notations from Chapter 2.3, the Maxwell equations for the TE and TM modes for a dielectric slab waveguide are, respectively:

$$\begin{aligned} \frac{\partial^2 E_y}{\partial x^2} + (k_0^2 \varepsilon - \beta_{TE}^2) E_y &= 0 \\ \frac{\partial^2 H_y}{\partial x^2} + (k_0^2 \varepsilon - \beta_{TM}^2) H_y &= 0 \end{aligned} \quad (5.5)$$

For the **TE mode**, we have the following continuity relations:

$$E_y(0) = E_y(d), H_z(0) = \frac{-j}{\omega \mu_0} \frac{\partial E_y}{\partial x}(0) = H_z(d), \quad (5.6)$$

thus we obtain the following expressions for the E_y component of the TE mode:

$$\begin{aligned} \text{In Air :} \quad E_y &= A \cos(\gamma_f d + \varphi) e^{\gamma_a(d-x)}; & y_a^2 &= \beta_{TE}^2 - k_0^2 n_a^2; & d < x \\ \text{In Film :} \quad E_y &= A \cos(\gamma_f x + \varphi); & y_f^2 &= k_0^2 n_f^2 - \beta_{TE}^2; & 0 \leq x \leq d \\ \text{In Substrate :} \quad E_y &= A e^{\gamma_s x}; & y_s^2 &= \beta_{TE}^2 - k_0^2 n_s^2; & x < 0 \end{aligned} \quad (5.7)$$

where $\tan \varphi = \gamma_s / \gamma_f$.

Next, it is straightforward to prove that the eigenvector and eigenvalue problems (5.5) can be reduced to the following transcendental equation for β_{TE} :

$$\gamma_f d + \arctan\left(\frac{\gamma_s}{\gamma_f}\right) + \arctan\left(\frac{\gamma_c}{\gamma_f}\right) = m\pi , \quad (5.8)$$

where $m=0,1,\dots$ represents the order of modes.

A similar approach can be used for the case of **TM mode** propagation. In this case, we have the following continuity relations:

$$H_y(0) = H_y(d), E_z(0) = j\omega\epsilon_0\epsilon \frac{\partial H_y}{\partial x}(0) = E_z(d), \quad (5.9)$$

and the following transcendental equation for β_{TM} :

$$\gamma_f d + \arctan\left(\frac{\epsilon_f \gamma_s}{\epsilon_s \gamma_f}\right) + \arctan\left(\frac{\epsilon_f \gamma_c}{\epsilon_c \gamma_f}\right) = m\pi . \quad (5.10)$$

To analyze these theoretical predictions, we have grown a single layer garnet film from which we have cut slab waveguides of different lengths. The chemical composition and magneto-optical parameters of interest for the sample used in our experiments are presented in Table V.2. The waveguide was cut so that the light propagation direction would be parallel to the hard axis of the material, as shown in Fig. 5.8.

TABLE V.2 Characteristics of the thin epitaxial garnet film used as optical magnetic field sensor.

Film parameter	Value
Composition	$\text{Lu}_{2.08}\text{Bi}_{0.91}\text{Pb}_{0.01}\text{Fe}_{3.88}\text{Ga}_{1.08}\text{Pt}_{0.04}\text{O}_{12}$
Thickness	2.3 μm
Faraday rotation (θ_F) at $\lambda=633$ nm	-13300 deg/cm
Saturation magnetization	13.5 kA/m
Uniaxial anisotropy (K_u)	-436 (J/m ³)
Cubic anisotropy (K_l)	-99 (J/m ³)
Index of refraction at $\lambda=1319$ nm	2.275

For a sample with similar physical properties, Fig. 5.9 shows the theoretical dependence of the effective index of refraction of the waveguide as a function of waveguide thickness. It can be seen that the initial thickness of our sample ($2.3 \mu\text{m}$) was large enough so more modes were propagating in the same time. For the fundamental mode $\Delta\beta$ is on the order of $8 \cdot 10^3 \text{ m}^{-1}$, which is much smaller than the

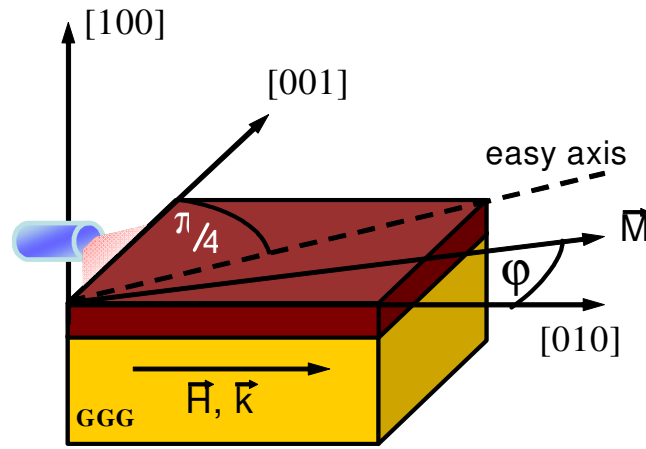


Fig. 5.8 In the proposed sensing element design, the propagation of light is along a magnetic hard axis.

approximated coupling coefficient (Faraday rotation) between the modes at $\lambda = 1370 \text{ nm}$, which is $\kappa \approx 1.3 \cdot 10^5 \text{ m}^{-1}$.

This looks encouraging, because the conversion factor will be large; unfortunately, the interpretation of the results is complicated when there are more propagating modes. In this case, it will be extremely complicated to use Eqs. (5.1) and (5.3) to recover the field that induced the measured changes in the output detector voltage.

In order to reduce the number of propagating modes, we have performed an etching experiment, where the waveguide was etched in phosphoric acid for different periods of time. As seen in Fig. 5.9, in order to get single mode behavior, the single-layer thickness has to be reduced down to $0.75 \mu\text{m}$.

In order to understand the effect of etching on waveguide birefringence, a more in depth discussion is required. Three phenomena contribute to the total birefringence:¹⁰⁰ $\Delta\beta_{total} = \Delta\beta_s + \Delta\beta_g + \Delta\beta$, where $\Delta\beta_s$ is the stress-induced optical birefringence due to the lattice mismatch between the substrate and the waveguide; $\Delta\beta_g$ is the growth-induced anisotropy, and the shape anisotropy $\Delta\beta$ has been discussed above. $\Delta\beta_s$ is negative for films in compression and independent of wavelength.¹⁰¹ Its magnitude is about 0.55 times the strain in the film.¹⁰² $\Delta\beta_g$ has a sign dependent on the film composition and can be reduced to zero by annealing the samples, which also reduces the growth-induced anisotropy.¹⁰³

By etching we reduced the thickness of the waveguide, but as can be seen from Fig. 5.10 this increased strongly the shape birefringence $\Delta\beta$ to $2 \cdot 10^5 m^{-1}$ which in turn reduces the conversion factor. As a consequence, the amplitude of the response for the etched waveguide is around 30mV vs. 100mV at the initial thickness. This decrease in the response amplitude also suggests that etching has not affected the values of $\Delta\beta_s$ and $\Delta\beta_g$ enough to obtain phase matching. In order to solve this issue we will discuss the case of multi-layer garnets in the next chapter.

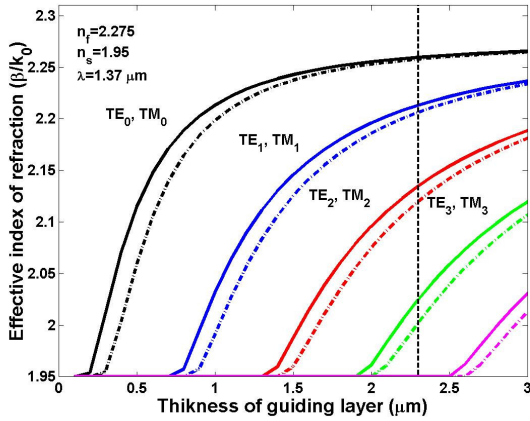


Fig. 5.9 Theoretical dependence of the effective index of refraction for a single layer garnet waveguide.

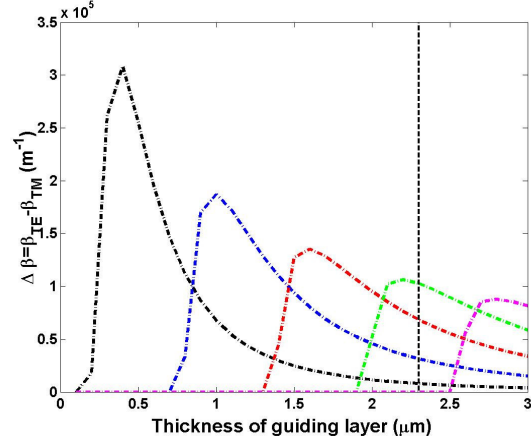


Fig. 5.10 Theoretical dependence of the difference between the propagation constants of the TE and TM modes (shape birefringence).

The response of the sensor is thus dependent on the value of the Faraday rotation per unit length, the length of the sensor, as well as its thickness. We have also seen that once a film is grown, the Faraday rotation is constant, but we have flexibility in choosing the waveguide length and the value of $\Delta\beta$ (by etching the sample). The conversion factor as a function of these two quantities is presented in Fig. 5.12, and it can be seen that as $\Delta\beta$ is increased, the conversion factor decreases, while if the length is increased, there is a sinusoidal dependence of the conversion factor. It is important to understand these changes in the conversion factor, in order to be able to select the correct length of the waveguide.

The linearity of the sensor response depends greatly on the value of the Faraday rotation per unit length, the length of the sensor as well as the angle α between the transmission axes of the polarizer and analyzer. For a given sensor length and $\alpha = \pi/2$, a range of fields can be identified where the response of the sensor is linear. This has been proven through experiments in which the applied magnetic field was varied sinusoidally with constant amplitude of 1.9 mT around an offset DC value B_0 .

The results for different values of B_0 are presented in Fig. 5.13. It can be seen that the highest linearity was measured around a field value of 6.4 mT for a field range of 3.8 mT.

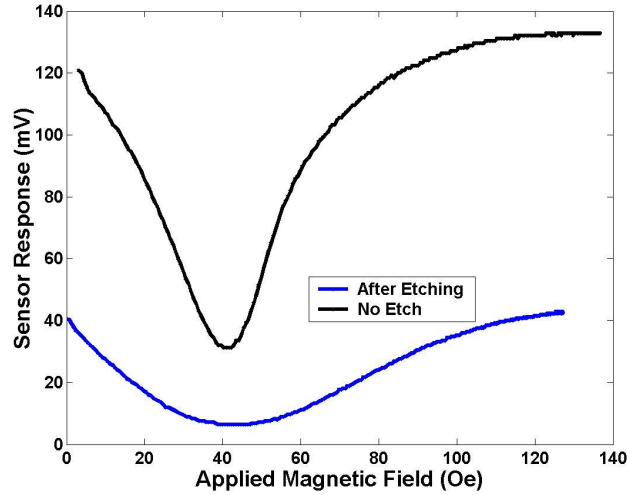


Fig. 5.11 The magnetic field sensor response changes after etching the garnet waveguide in hot phosphoric acid.

This does not mean that our sensor needs a biasing field in order to work in the linear region. In order to support this conclusion, the expected conversion efficiency was computed as a function of the applied magnetic field in the absence of any biasing fields. First, Eq. (5.3) was used to determine the equilibrium position of the magnetization for each value of the applied field. Then Eq. (5.1) was utilized to calculate the Faraday rotation and thus the coupling coefficient κ . Finally, the conversion efficiency was calculated from Eq. (5.2) for different waveguide lengths. The results are shown in Fig. 5.13. From these results it can be concluded that if the other material properties are fixed, the linearity range and the slope of the sensor response can be tailored by modifying the sensor length. This introduces an additional flexibility at the sensor design stage. Once a film has been epitaxially grown, and its properties measured in bulk form, simulations can be performed in order to determine

how the sensor will behave for different lengths. Once the length is theoretically selected, the final cutting and polishing stages can be performed to obtain the desired waveguides.

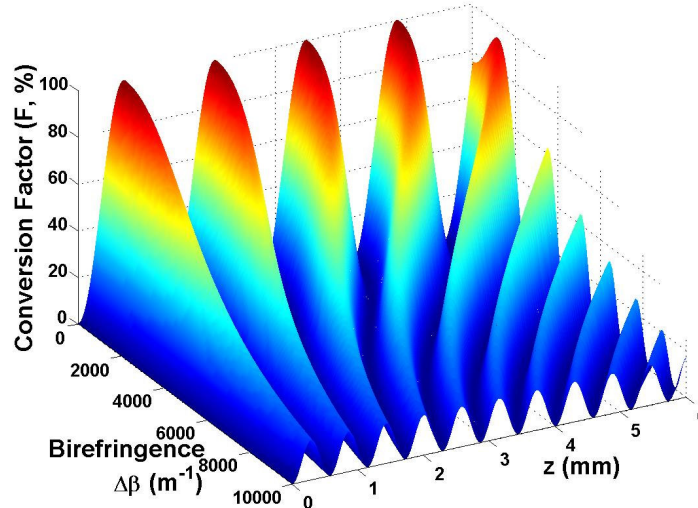


Fig. 5.12 Variation of the conversion efficiency F with waveguide length as a function of waveguide birefringence $\Delta\beta$.

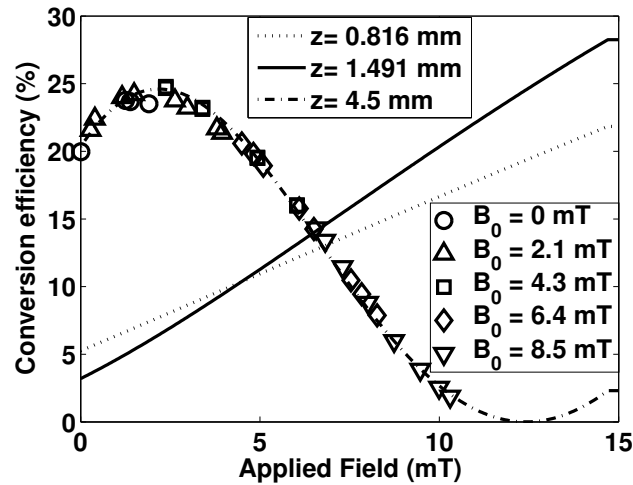


Fig. 5.13 Conversion efficiency vs. applied field for different waveguide lengths. The lines represent theoretical simulations while the symbols correspond to experimental data.

It can be seen from Fig. 5.13 that sensor lengths of either $z=0.82$ mm or $z=1.49$ mm result in linearization of the sensor response for the entire range of measurable fields with the difference that the slope of the response would be smaller in the first case. Moreover, Fig. 5.13 indicates that the highest field that can be measured with

this sensor is 14.7 mT, equal to the value of the cubic anisotropy field that controls the in-plane saturation of the sample. In order to expand the range of measurable fields, the cubic anisotropy field can be increased by increasing the Ga substitution in the epitaxial film.

We have also measured the sensitivity of our sensor using the same parameters as in Ref. 2. The value of the sensitivity is controlled by the noise within the system such as optical shot noise, electronic noise, mechanical vibrations of the system, as well as variations in the laser output power. Experimentally, a magnetic field with an amplitude of 10^{-4} T (rms) and frequency 80 Hz has been applied in the film plane parallel to the light propagation direction. The signal was averaged for different periods of time and a spectrum analyzer has been used to obtain the frequency spectra of the response as shown in Fig. 5.14. The results indicate that for a noise bandwidth of 0.078 Hz, the noise floor is approximately $1.5 \mu\text{T}/\sqrt{\text{Hz}}$.

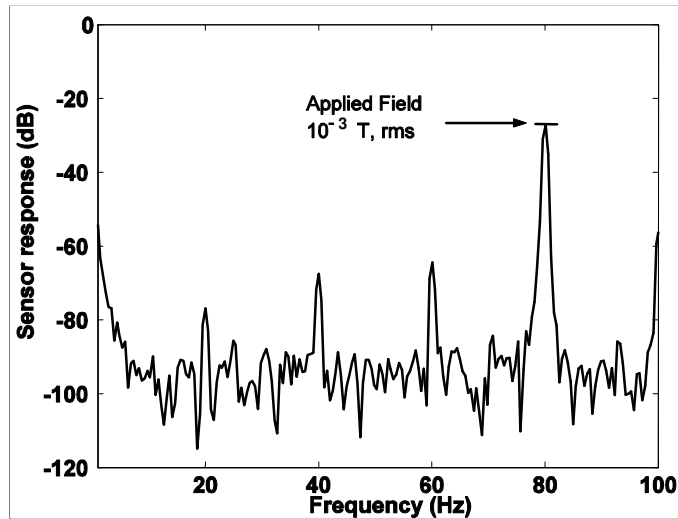


Fig. 5.14 Noise spectra of the sensor response for an applied magnetic field of 0.1 mT and a frequency of 80 Hz. The noise bandwidth was equal to 0.078 Hz.

5.4 Optical sensors based on symmetric layer garnet films

5.4.1 Determination of layer specific magnetic properties in multi-layer garnets

As discussed in the previous chapter, the use of one layer garnets for sensing elements is complicated by the phase shift difference between the fundamental TE and TM modes, as well as by the multimode regime when the film is thicker. In order to circumvent these difficulties, we have grown multi-layer structures that have cladding layers between the substrate and the guiding layer, as well as between the guiding layer and air. As investigated in detail in Chapter 4.5, in order to obtain layers with different magnetic and optic properties so as to insure guiding effect through the waveguide, we changed the substrate rotation rate from 64 rpm to 196 rpm during the growth process. This slightly changes the index of refraction between the cladding and guiding layers and results in different anisotropy fields and different saturation magnetizations.

Before we describe the results obtained with such a structure as a sensing element, it is important to discuss how to precisely and completely characterize the magnetic properties (magnetic anisotropies, magnetization) of every layer. Ferromagnetic resonance (FMR) measurements are well suited for this purpose, but their disadvantage is that they only yield the effective anisotropy fields and additional magnetization measurements are required to fully separate the terms involved in these fields. For multiple layer structures the magnetometer measures only an average of the magnetizations of the entire sample, thus the magnetization of each layer can not be directly obtained. To overcome this limitation, we proposed a new method to

simultaneously recover the saturation magnetization (M_s) for multiple layers by using just one vibrating sample magnetometer (VSM) measurement combined with several FMR measurements to determine the anisotropy fields.

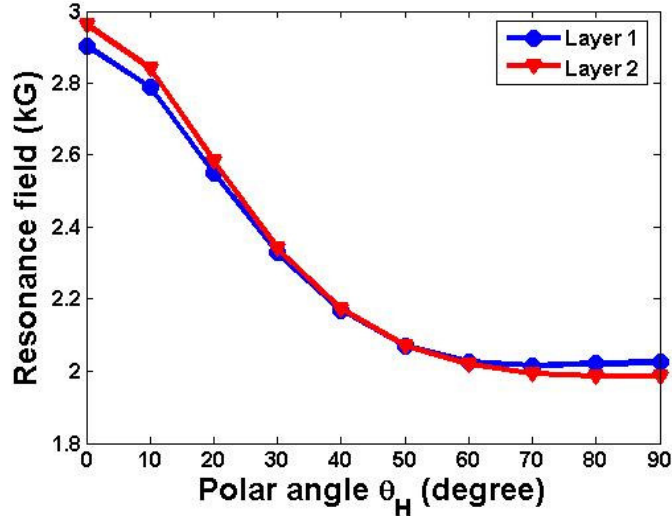


Fig. 5.15 In multi-layer garnets, FMR-resonance peaks can be resolved and the corresponding resonance fields change as a function of the polar angle θ_H .

A double layer garnet film with a size of 10 ×10 mm and total thickness of 4.8 μm was grown by using liquid phase epitaxy. The layers were grown on a (Ca,Mg,Zr)-substituted gadolinium gallium garnet (CMZ-GGG) substrate with a lattice constant of $a=12.498\text{\AA}$ and have a generic composition of $(\text{Bi,Lu,Gd})_3(\text{Fe,Ga})_5\text{O}_{12}$. In order to fully characterize each layer, FMR experiments were performed to find the anisotropy fields. Due to the narrow FMR linewidth of (Bi,Lu,Gd) - substituted garnets, the resonant peaks of multiple layers can be effectively resolved. The resonance field for each layer was measured as a function of the angle θ_H between the normal to the sample surface and the applied DC field for a fixed microwave frequency of 6 GHz.¹⁰⁴ The angle θ_H was changed by placing the multi-layer film perpendicular to the DC field, and then rotating it around one of the in-plane material hard axes. The result of the FMR measurements for a double layer garnet film is shown in Fig. 5.15.

As the resonance fields are well above the saturation fields of the garnet films, it can be assumed that the magnetization is homogenous and the free energy density can be written as:

$$f = M_s \left\{ \frac{H_{u,eff}}{2} \sin^2 \theta + \frac{H_1}{2} [\sin^4 \theta \sin^2 \varphi \cos^2 \varphi + \sin^2 \theta \cos^2 \theta] - H [\cos \theta_H \cos \theta + \sin \theta_H \sin \theta \cos(\varphi - \varphi_H)] \right\}, \quad (5.11)$$

where $H_{u,eff} = 2K_u / M_s - 4\pi M_s$ is the effective uniaxial anisotropy field with the uniaxial anisotropy constant K_u , $H_1 = 2K_1 / M_s$ is the cubic anisotropy field with the cubic anisotropy constant K_1 , and H is the applied field.

The angle θ_H is, as before, the angle between the applied field and the film normal and the angle φ_H is the angle between the projection of the applied field onto the film plane and the [001] direction. The angles θ and φ denote the equivalent equilibrium angles for the magnetization. It is important to mention that in the case of garnets, FMR measurements allow only to determine the anisotropy fields and not the value of the magnetization, or the anisotropy constants separately.

For the double layer garnet used in this experiment, by fitting the measured data to the Smit-Suhl formula (4.10), the anisotropy fields were determined to be $H_{u,eff1} = -600$ Oe and $H_{1,1} = -237$ Oe for the layer grown at the rotation of 64 RPM, and $H_{u,eff2} = -660$ Oe and $H_{1,2} = -230$ Oe for the layer grown at the rotation of 196 RPM.

VSM measurements were then performed with the field perpendicular to the double-layer film. In order to determine the equilibrium angles of the magnetization

vectors for each layer for different applied fields (see Fig. 5.16), a series of simplifying assumptions were made. First, if the area of the samples is much larger than their thickness, the fringing field will be localized at the edges of the sample, thus no coupling was induced between the layers. Second, although some exchange coupling might take place at the interfaces, if the layers have thicknesses in the microns range, there will be no exchange coupling between them.

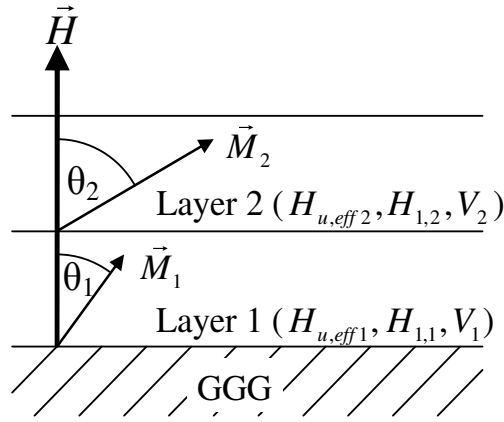


Fig. 5.16 Schematic showing the magnetization equilibrium position in layers with different properties in a VSM experiment where the field is applied perpendicular to the film surface.

Under these assumptions, the two layers act like independent single layers. Thus, if the field is applied perpendicularly to the garnet surface, the in-plane component of the magnetization is always along one of the easy axes ($\varphi = \pi/4, 3\pi/4, 5\pi/4$ or $7\pi/4$). Consequently, Eq. (5.11) can be simplified and differentiated with respect to $\cos(\theta)$ yielding the equilibrium condition for the equilibrium polar angle of \vec{M} in each layer:

$$H = -H_{u,eff,i} \cos \theta_i + \frac{H_{1,i}}{2} \{ \cos \theta_i - 3 \cos^3 \theta_i \}, \quad (5.12)$$

where $i=1,2$ and $H_{u,eff,i}$, $H_{1,i}$ are the effective and cubic anisotropy fields for each layer.

As seen from Eq. (5.12), it is worthwhile to mention here that the usefulness of our method is that for any applied field, the magnetization equilibrium angles $\theta_1(H)$ and $\theta_2(H)$ can be expressed only as functions of the anisotropy fields measured by FMR ($H_{u,eff}$ and H_1), that is without requiring the previous knowledge of the saturation magnetization.

In the VSM measurement, the pick-up coils generate a signal proportional to the component of magnetic moment perpendicular to the film surface. Thus, in the case of the double layer garnet film, the result of the VSM measurement will be the magnetic moment given by the following formula:

$$m_{VSM}(H) = M_{s,1}V_1 \cos \theta_1(H) + M_{s,2}V_2 \cos \theta_2(H), \quad (5.13)$$

where V_1 and V_2 are the volumes of the first and second layer respectively, and θ_1 and θ_2 are the equilibrium polar angles of the magnetization in layer 1 and 2.

In order to recover the saturation magnetizations ($M_{s,1}$ and $M_{s,2}$) of each layer, Eq. (5.13) was fitted by using the least-squares method for different values of the applied field. The results of the fit are $4\pi M_{s,1} = 460 \text{ G}$ and $4\pi M_{s,2} = 560 \text{ G}$. With these values, and using the anisotropy fields obtained from FMR measurements, the anisotropy constants can also be determined for every layer.

5.4.2 Noise and sensitivity measurements for sensors based on multi-layer garnet films

After we can completely characterize multi-layer structures, as described above, we revisited our sensor element idea as shown in Fig. 5.17. Instead of using a single-layer garnet for waveguiding, which suffers from problems mentioned above in terms

of phase shift and multi-mode behavior, we decided on using a multi-layer structure, as that indicated above. Such a structure was grown by keeping the LPE melt at the same undercooling and changing the RPM of substrate during the growth process.

The bottom and top cladding layers with an index of refraction n_c were grown by LPE at an RPM rate of 25. The waveguiding layer with an index of refraction n_f was grown at a much higher 196 RPM. The indices of refraction of each of the layers were measured by using the prism coupling method. At $\lambda = 1319nm$, the closest wavelength available for measurements to our experimentally used laser source with $\lambda = 1370nm$, we have obtained that $n_c = 2.265$ and $n_f = 2.275$, thus a difference of $\Delta n = 10^{-2}$ enough to insure the guiding effect through our layer. This is not a good waveguide, but we do not consider losses at this stage because they are not important in our system. Remember, one of our goals is to use materials with Giant Magneto-optical Effect in order to reduce the length of the sensing element, thus even if there are losses in our system, they are not very important to the outcome.

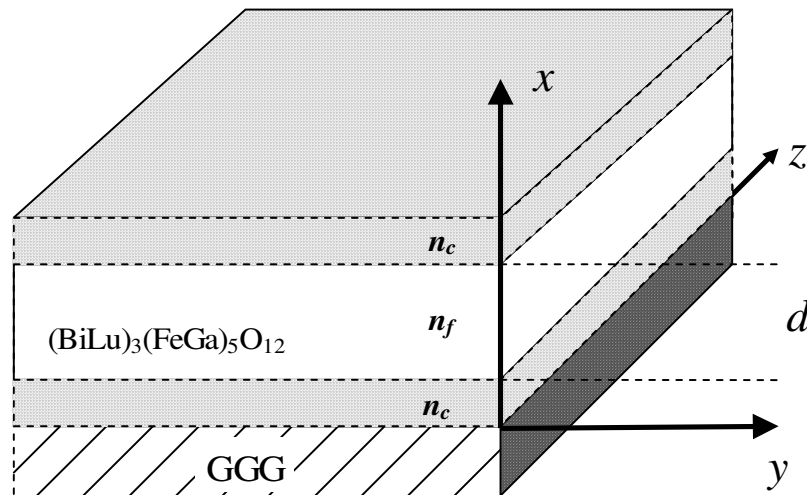


Fig. 5.17 Symmetric-layer garnet slab waveguide used as sensing element.

For the TE and TM propagation modes, we have studied such a symmetric waveguide structure by using Eqs. (5.7)-(5.9). In Fig. 5.18, the reduced propagation constants β_{TE}/k_0 and β_{TM}/k_0 are plotted as a function of the thickness d , while in Fig. 5.19 the shape birefringence $\Delta\beta = \beta_{TE} - \beta_{TM}$ is shown as a function of the thickness d of the guiding layer. It is easy to see that the maximum $\Delta\beta$ value is less than 150 m^{-1} , which is very small when compared to Faraday rotation that can reach 10^5 m^{-1} . From this point of view, the use of such cladding waveguide structures is beneficial.

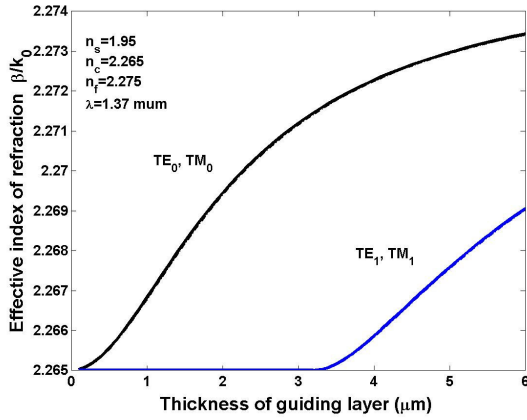


Fig. 5.18 Theoretical dependence of the effective index of refraction for a symmetric layer garnet waveguide.

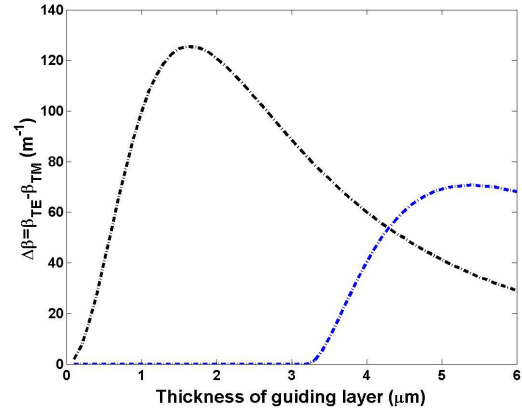


Fig. 5.19 Theoretical dependence of the shape anisotropy for a symmetric cladding structure.

In order to test these theoretical predictions, we have used the three layer garnet structure described above, by cutting wavelengths at different lengths. The thickness of the garnet guiding layer was chosen to be $5.5 \text{ }\mu\text{m}$, large enough to improve the coupling between the tapered fiber tip and the waveguide. The measured sensor response for both types of waveguides is shown in Fig. 5.20. It can be seen that the voltage change is even smaller than in the case of the single layer waveguide, in contradiction with what was theoretically predicted. This decrease in voltage change is due to a decrease in the conversion factor of these waveguides. This discrepancy

can be explained by the fact that the modes will have a strong intensity in the cladding layers (see Fig. 5.22), because of the small difference in the index of refraction between the guide and cladding. Also, additional modes can appear from reflections at the cladding-air and cladding-substrate interfaces. All these additional modes will couple with the fundamental TE and TM modes, decreasing thus the conversion efficiency. The noise measurements indicate a sensitivity of between 3.5 to 5 $\mu\text{T}/\sqrt{\text{Hz}}$ at an applied field frequency of 80 Hz.

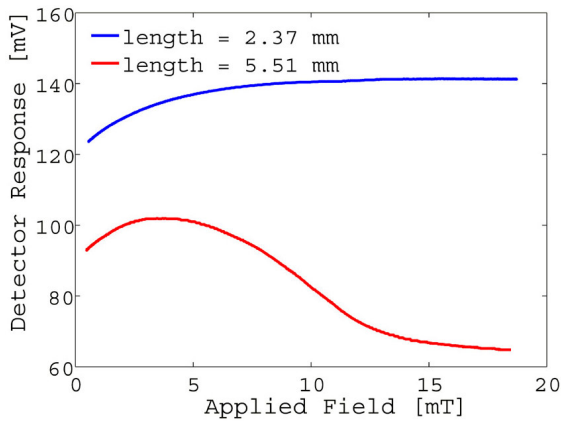


Fig. 5.20 Sensor response for a triple layer waveguide for two different waveguide lengths.

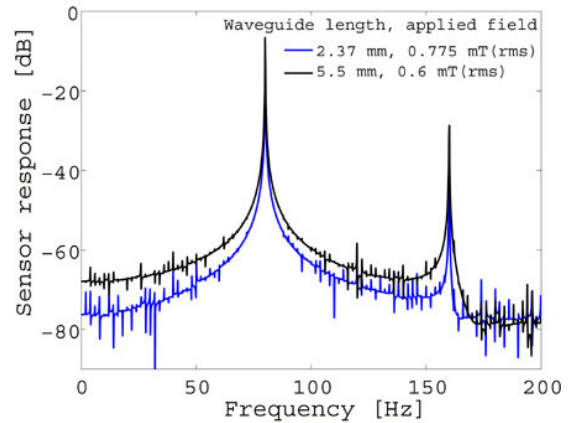


Fig. 5.21 Noise spectra of the sensor response for two symmetric slab waveguides. The frequency of the applied field was 80 Hz and the noise bandwidth was 0.0156 Hz.

A solution to the multi-mode propagation problem was suggested by Dammann *et. al.*¹⁰⁰, and consists of using a highly absorbing layer between the guiding structure and the substrate. In this way, any additional modes besides those propagating through the guide will be attenuated. This approach requires the use of 2 melts for garnet growth. One melt has to be designed to yield garnet films with high absorption coefficients (i.e. by using Pr or Co substitution), while the other melt is required to yield garnets with low absorption (i.e. using Bi, Lu, Gd).

Since we are using the butt coupling method instead of prism coupling, we propose a different approach to reduce the number of modes propagating through a multi-layer structure. For reasons related to material growth, it is more convenient to grow the highly absorbing layer on top of the structure. In order to see whether or not such a structure will reduce the number of propagating modes, we have simulated the effect of an absorbing layer deposited on top of our structure. The results are shown in Fig. 5.23. We see that most of the intensity of the fundamental TE and TM modes is concentrated in the guiding layer, while the bulk of the intensity for additional propagating modes is concentrated in the absorbing layer. This means that these additional modes will be attenuated thus yielding the required single-mode behavior of the sensing element.

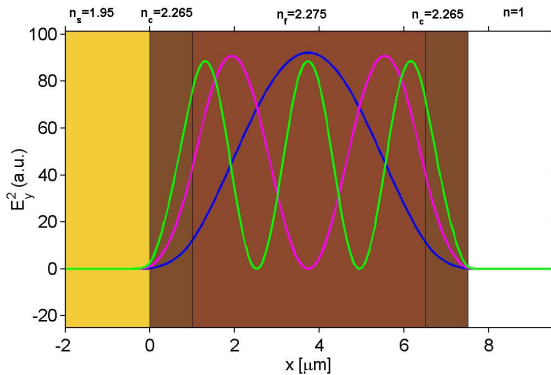


Fig. 5.22 Intensity profiles of the first 3 of 10 possible propagating TE modes for a triple symmetric layer waveguide.

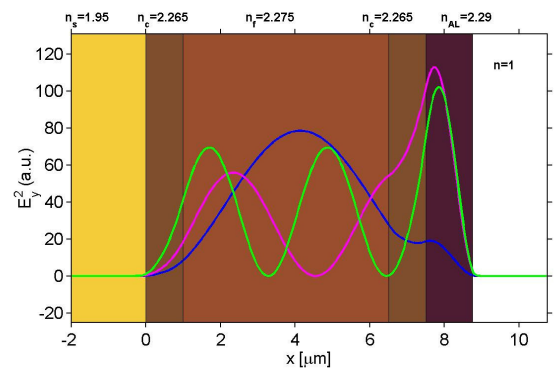


Fig. 5.23 Intensity profiles of the first 3 of 11 possible propagating TE modes for a triple symmetric layer waveguide with an additional absorbing layer (AL) on top.

5.5 Temperature dependence of sensor films

One of the most important characteristics that will affect the sensor performance is the temperature stability. The proposed solution is based on modifying the material

properties at the molecular level. In order to tackle this issue we performed numerical calculations based on the molecular field theory.¹⁰⁵

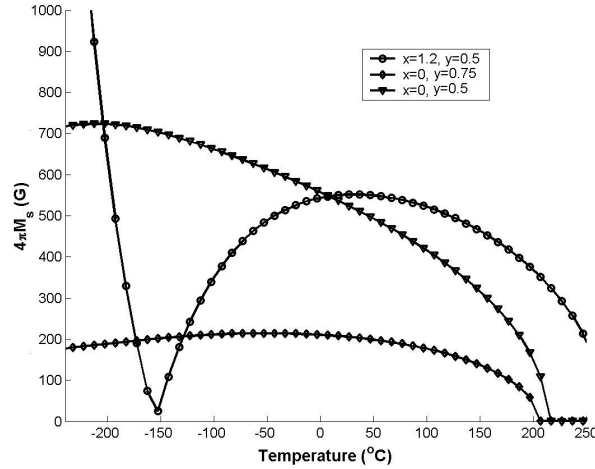


Fig. 5.24 The sensor stability vs. temperature changes with different substitution elements.

One of the reported methods was using substitution of Fe ions with diamagnetic ions like Al and Ga.^{106,107} From Fig. 5.24 one can see that if in a (BiLu) substituted garnet 0.75 f.u. of Fe are substituted by Ga., a constant magnetization from $-200^{\circ}C$ to approximately $100^{\circ}C$ is obtained. It might seem that this is the best solution for ensuring the temperature stability of the sensor. But the amplitude of the resulting saturation magnetization is very small. This in turn means that a lower Faraday rotation per unit length is obtained which is the opposite of the effect that we are looking for. If the Ga substitution is decreased to 0.5 f.u., the saturation magnetization increases (as expected), but another issue is raised. The slope of the temperature variation $\frac{dM_s}{dT}$ increases, which means that the sensor will be very sensitive to the temperature. The solution was proposed in terms of using a magnetic ion like Gd as substitution on the dodecahedral site.^{32,63} As shown in Fig. 5.24 the Gd substitution will increase the magnetization. In the same time it can be seen that the

saturation magnetization passes through zero at a temperature lower than the Curie point (T_c is somewhere in the 560-600 K range for these materials). This temperature is called a compensation point and is due to the fact that the magnetization on the dodecahedral site will cancel the resultant magnetization of the antiferromagnetically coupled octahedral and tetrahedral sublattices. The existence of this compensation point is essential for our purpose. We can see that the magnetization increases again passing through a maximum before falling to zero at the Curie temperature T_c . Therefore above the compensation point there is a temperature range over which the magnetization is approximately constant. The materials displaying maxima in the range -100°C to 100°C are of particular interest for our sensor application.

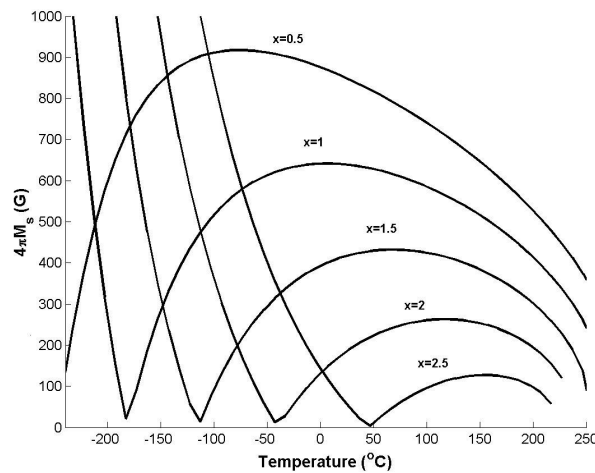


Fig. 5.25 Gd-substituted garnets are proposed as garnet materials with good temperature stability and high saturation magnetization.

It has been measured experimentally that by changing the Gd substitution from .7 to 3 formula units gives a linear variation of the compensation temperature T_{cp} from 0 to 290 K.⁶³ The magnetization against temperature characteristics of Gd substituted garnets are shown in Fig. 5.25. We can see that a Gd incorporation of 1 f.u.

determines a useful sensor temperature range of -50°C to 100°C and a magnetization of around 650 G.

Yet the use of Gd does not come only with advantages. Gd induces almost no magnetostriction⁴⁶ which means that using the lattice mismatch to grow epitaxial films in compression (which will favor the in-plane magnetization) is not a solution anymore. Alternative melt chemistries have to be used in order to modify the growth induced anisotropy. One of these possible melts is based on Bi, Gd and Lu substitutions and has been discussed in Chapter 4. Finally, since Gd is a large ion, large lattice substrates have to be used in order to ensure that the film grows without suffering cracks from mechanical stresses. In terms of sensor behavior, high Gd substitutions have an adverse effect on the FMR resonance line widths, thus influencing the sensor frequency response.

5.6 On-chip integration of magneto-optic field sensors

Most of the sensor prototypes explored over the years have used magnetic garnets, such as yttrium iron garnet (YIG), bismuth-substituted YIG (BiYIG) and various other rare-earth iron garnets, because of their nonreciprocal optical properties and low loss in the near infrared but in the bulk form. In this dissertation, thin (μ -thick) single-crystal films grown by liquid-phase epitaxy (LPE) on garnet templates, such as GGG, cation doped GGG [(CaMgZrGdGa) O] (CMZGGG), are suggested as new materials for sensor development. RF sputtering has also been used to grow high-quality epitaxial films on GGG and other substrates as discussed in Ref. 108-116.

In fact, sputtering techniques have been particularly successful in achieving very high bismuth and cerium substitution contents, hence large Faraday rotations, where LPE has been restricted by solubility limits. Absorption losses as low as 0.5 dB/cm have been reported for LPE films.¹¹⁷

But the development of on-chip waveguide sensors, and more general the development of any integrated garnet components (isolators) faces the following challenge. The deposition of magnetic garnets on other technologically important platforms (silicon, polymers, and glasses), of considerable importance for integrated photonic circuits, is less developed and novel ways need to be found to produce low-loss films with strong magneto-optical properties in such substrates. Garnet sputtering in glass and silicon has been developed mostly in connection with magneto-optic recording and produced films with large perpendicular uniaxial magnetic anisotropy and large coercivities. More recently, Stadler and Gopinath have reported the sputter deposition of cerium-substituted YIG on magnesium oxide substrates.¹¹⁸ These films have in-plane magnetization and small coercive fields, conditions that are generally needed for waveguide Faraday rotation devices. The deposition of barium hexaferrite on sapphire and other materials is also being investigated for use in magneto-optical applications.^{119,120,121,122} And recent work on III-V diluted magnetic semiconductors shows promise for the fabrication of magneto-optical devices in certain limited spectral bands.^{123,124}

In recent years, ion implantation film-transfer techniques have been developed with great success in silicon and various oxide materials including single-crystal magnetic garnets.^{125,126,127} These techniques rely on the formation of an underlying

sacrificial layer in the bulk for the release of single-crystal films of very high quality. Thermally induced crack propagation or high wet-etch selectivity have been used to separate the films. The development of these technologies has benefited from advances in materials bonding techniques, such as direct wafer bonding, to yield thin-film heterostructures in growth-incompatible materials. The separation of single-crystal YIG and BiYIG films from bulk and LPE-grown films on GGG has been demonstrated by Levy *et al.*¹²⁷ and the results were encouraging. Fig. 5.26 shows a cross-sectional view of a partially detached single-crystal YIG film as a result of wet etch removal of a sacrificial layer formed by ion implantation. The implantation of 3.8-MeV He ions nearly normal to the top surface at a dosage of cm engender a fast-etching sacrificial layer 10 μm beneath the surface. The scanning-electron micrograph (SEM) in Fig. 5.26 illustrates the undercut formed upon etch removal of the damaged layer leading to the formation of a freestanding single-crystal film. Tests on these films showed no significant changes in domain structure or magnetic anisotropy as a result of the ion implantation and liftoff process. Slab waveguide insertion loss measurements performed on implanted BiYIG films under the same conditions yielded no significant degradation in optical transmission after thermal treatment to repair residual implantation damage.

The ion implantation technique offers thus great hope that soon, the garnet materials will not be regarded as exotic magnetic materials any more, but will take their rightful place among other materials with great importance for the magnetic industry, as integrated sensors to measure magnetic fields, imagers to visualize

magnetic patterns and material defects, as well as integrated modulators and isolators for the optical communications industry.

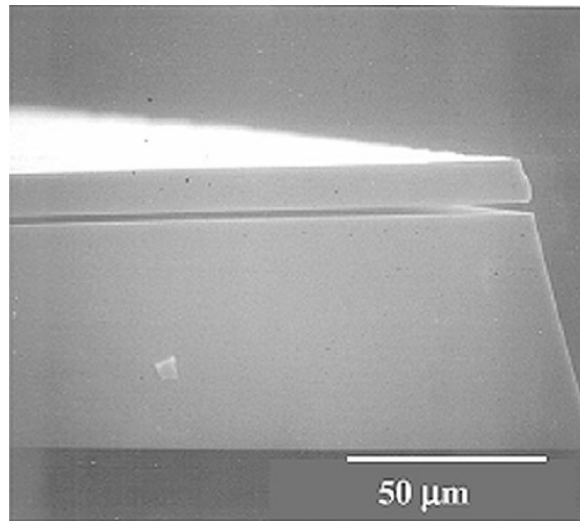


Fig. 5.26 SEM of partially detached single-crystal YIG film by selective etching (from [127]).

Conclusions and Future Work

This dissertation discusses the use of magnetic single crystal Bismuth - substituted iron garnet thin-films with giant magneto-optical effect as optical sensors for measuring high frequency (up to 1GHz), low intensity magnetic fields. The design of these sensors is based on a guiding structure using a single crystal thin film grown by the liquid phase epitaxy method. The advantages of these sensors are high intrinsic sensitivity and the possibility of tailoring the field range for linear response. Actual optical sensors have been obtained from in-house grown garnets, and their response has been measured. Study of the sensor response to magnetic fields yielded noise equivalent magnetic fields of $1.5 \mu T / \sqrt{Hz}$ and a signal-to-noise ratio of 68dB. In order to enhance the sensitivity, additional research is needed to understand the sources of noise and to improve the coupling efficiency in the optical fiber and garnet waveguide system.

Until now, a great deal of experience and specific knowledge has been accumulated in the material growth part of the project. The melt compositions that are investigated in this dissertation demonstrate that the growth of films with in-plane magnetization, giant Faraday rotation per unit length, and large negative uniaxial anisotropies has been accomplished successfully and in a repeatable manner.

As discussed in Chapter 5, additional future work has to be performed in the device fabrication area, to insure single mode behavior of the garnet waveguide. One of the envisaged methods is to use an absorbing layer as a cladding layer. An additional method is to use stress to control the waveguide birefringence.

Finally, to help promote these devices as a viable alternative to the more established Hall and fiber optic sensors, more work is needed towards accomplishing on-chip integration of garnet devices with semiconductor based platforms. This would greatly reduce the production costs and would motivate research in the area of these fascinating materials, the substituted rare-earth iron garnets.

Appendix A: Jones Calculus

A convenient method to describe the polarization in optics is the mathematical approach of Jones calculus.¹²⁸ Jones calculus represents a polarized light wave as a vector (Jones vector), and linear optical elements by matrices (Jones matrices). To describe the effect of an optical element on the polarization state of a passing light wave, the Jones vector corresponding to the initial polarization state is simply multiplied by the Jones matrix corresponding to the optical element. With this method, the effect of a system of consecutive elements on the polarization state can be calculated by multiplication of the respective matrices.

Jones vectors

An arbitrary polarized plane wave propagating in the z direction can be expressed as:

$$\vec{E} = \begin{pmatrix} E_{x0} \\ E_{y0} e^{j\delta} \\ 0 \end{pmatrix} e^{j(\alpha - k_1 z)} \quad (\text{A.1})$$

In this case, Jones calculus method describes the plane wave using the following Jones vector:

$$\vec{J} = \begin{pmatrix} E_{x0} \\ E_{y0} e^{j\delta} \end{pmatrix} = A \begin{pmatrix} \cos \alpha \\ e^{j\delta} \sin \alpha \end{pmatrix}, \text{ with } \tan \alpha = \frac{E_{y0}}{E_{x0}}, 0 \leq \alpha \leq \frac{\pi}{2}, \text{ and } -\pi \leq \delta \leq \pi. \quad (\text{A.2})$$

A graphical representation for the polarization is the polarization ellipse in Fig. A.1. The ellipse is unambiguously determined by two parameters, e.g. Θ and Ψ , or α and δ . To convert between the two sets of parameters the following relations can be used:

$$\tan 2\Theta = \tan 2\alpha \cdot \cos \delta, \quad \sin 2\Psi = \sin 2\alpha \cdot \sin \delta \quad (\text{A.3})$$

and

$$\cos 2\alpha = \cos 2\Psi \cdot \cos 2\Theta, \quad \cot \delta = \cot 2\Psi \cdot \sin 2\Theta \quad (\text{A.4})$$

with $-\pi \leq 2\Theta \leq \pi$ and $-\frac{\pi}{2} \leq 2\Psi \leq \frac{\pi}{2}$.

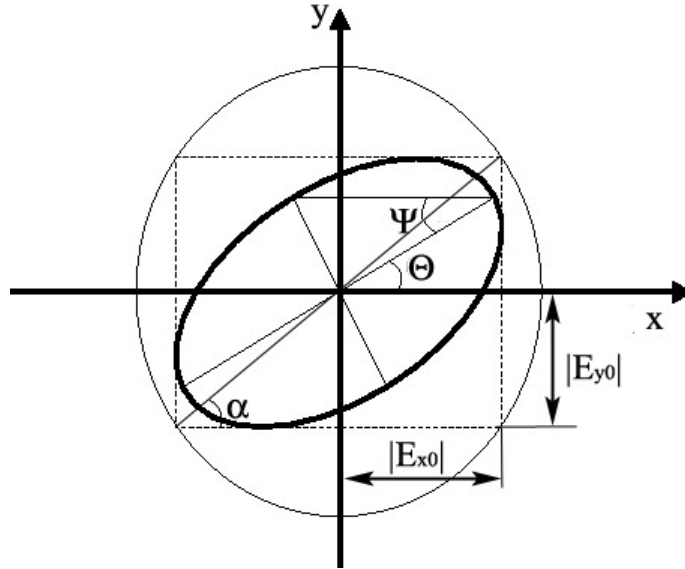


Fig. A.1 Polarization ellipse used to describe the polarization state of a wave.

The following types of elliptically polarized waves are most common in practical applications and can be expressed in an elegant fashion using Jones vectors as shown below:

Parameters	Jones vectors	Polarization State
$\delta = 0$, E_{x0} , and E_{y0} arbitrary	$\begin{pmatrix} E_{x0} \\ E_{y0} \end{pmatrix}$	Linearly polarized light
$\delta = \pm \frac{\pi}{2}$, $E_{x0} = E_{y0} = E_0$	$E_0 \begin{pmatrix} 1 \\ \pm j \end{pmatrix}$	Right / left circular polarized light wave

$\delta = \pm \frac{\pi}{2},$ $E_{x0} \neq E_{y0}$	$\begin{pmatrix} E_{x0} \\ \pm jE_{y0} \end{pmatrix}$	Right / left elliptically polarized light wave
---	---	--

Jones Matrices

Below is a list of Jones matrices associated to most commonly used optical elements in magneto-optical measurements.

Parameters	Jones vectors
Polarizer rotated by an angle β with respect to the x-axis –used for converting the polarization change into a measurable light intensity change effect.	$T_{Pol} = \begin{pmatrix} \cos^2 \beta & \cos \beta \cdot \sin \beta \\ \cos \beta \cdot \sin \beta & \sin^2 \beta \end{pmatrix}$
Photoelastic modulator – used to determine the maximum Faraday rotation (at saturation) of the samples. The index of refraction is modulated by Δn at a frequency $\Delta\omega_p$.	$T_{PEM} = \begin{pmatrix} \exp(jk_0 d \Delta n \cdot \sin \omega_p t) & 0 \\ 0 & \exp(-jk_0 d \Delta n \cdot \sin \omega_p t) \end{pmatrix}$

<p>Magneto-optical crystal with Faraday rotation θ_F, thickness d, and circular dichroism ϕ_F</p>	$T_{Pol} = \exp(-\alpha_0 d/2 - jk_0 n_0 d) \cdot$ $\begin{pmatrix} \cos \theta \cosh \phi + i \sin \theta \sinh \phi & -\sin \theta \cosh \phi + i \cos \theta \sinh \phi \\ \sin \theta \cosh \phi - i \cos \theta \sinh \phi & \cos \theta \cosh \phi - i \sin \theta \sinh \phi \end{pmatrix},$ <p>with $\theta = \theta_F \cdot d, \phi = \phi_F \cdot d, \alpha_0 = \frac{(\alpha^+ + \alpha^-)}{2}$, and</p> $n_0 = \frac{(n^+ + n^-)}{2}$
---	--

Bibliography

-
- ¹ R. Wolfe, E. M. Gyorgy, R. A. Lieberman, V. J. Fratello, S. J. Licht, M. N. Deeter, and G. W. Day, "High frequency magnetic field sensors based on the Faraday effect in garnet thick films", *Appl. Phys. Lett.* **60** (17), 2048 (1992).
- ² M. N. Deeter, A. H. Rose, and G. W. Day, "Fast, Sensitive magnetic field sensor based on the Faraday effect in YIG", *Journal of Lightwave Technology* **8** (12), 1838 (1990).
- ³ C. Menadier, C. Kissinger, and H. Adkins, "The fonic sensor", *Instruments & Control Systems* **40**, 114 (1967).
- ⁴ J. A. Powell, "A simple two-fiber optical displacement sensor", *Rev. Sci. Instrum.* **45** (2), (1974).
- ⁵ D. E. N. Davies, and S. Kingsley, "Method of phase-modulating signals in optical fibers: Application to optical telemetry systems", *Electronics Letters* **10**, 21 (1974).
- ⁶ J. A. Bucaro, H. D. Dardy, and E. F. Carome, "Fiber optic hydrophone", *Journal of Acoustical Society of America* **62**, 1302 (1977).
- ⁷ J. P. Dakin, and D. A. Kahn, "A novel fiber optic temperature probe", *Optical and Quantum Electronics* **9**, 540 (1977).
- ⁸ C. D. Butter, and G. B. Hocker, "Fiber optics strain gauge", *Applied Optics* **17** (18), 2867 (1978).
- ⁹ K. A. James, W. H. Quick, and V. H. Strahan, "Fiber Optic sensors for military, industrial and commercial applications", *Proc. of the International Telemetering Conference, Instrument Society of America*, 777 (1978).
- ¹⁰ J. N. Fields, C. K. Asawa, O. G. Ramer, and M. K. Baronski, "Fiber optic pressure sensor", *J. Accust. Soc. Am.* **67** (3), 816 (1980).
- ¹¹ M. Krieh, O. Steijer, O. Pers, and G. Edwall, "Fiber optic dark-field micro-bend sensor", *SPIE Proc. Fiber Optic Sensors* **586**, 216 (1985).
- ¹² W. W. Morey, G. Meltz, and W. H. Glenn, "Fiber optic Bragg grating sensors", *SPIE Proc. Fiber Optic and Laser Sensors VII* 1196, 98 (1989).
- ¹³ J. P. Dakin, and D. J. Pratt, "Distributed optical fiber Raman temperature sensor using a semiconductor light source and detector", *Electronics Letters* **25**, S56 (1989).
- ¹⁴ G. P. Hancke, "A fiber optic density sensor for monitoring the state-of-charge of a lead acid battery", *IEEE Trans. on Instrumentation and Measurement* **39** (1), 247 (1990).
- ¹⁵ D. A. Jackson, and J. D. C. Jones, "Interferometers", *Optical Fiber Sensors 2; Systems and Applications*, B. Culshaw and J. Dakin, 329, Artech House, Norwood, (1989).
- ¹⁶ W. J. Bock, T. R. Wolinski, and A. Barwicz, "Development of a polarimetric optical fiber sensor for electronic measurement of high pressure", *IEEE Trans. on Instrumentation and Measurement* **39** (5), 715 (1990).

-
- ¹⁷ M. N. Charasse, M. Turpin, and J. P. Le Pesant, "Dynamic pressure sensing with a side hole birefringent optical fiber", *Optics Letters* **16** (13), 1043 (1991).
- ¹⁸ H. Sohlström, and U. Holm, "A fiber optic displacement sensor", *Acta IMEKO*, 183 (1982).
- ¹⁹ I. Kajtano, and A. T. Friberg, "A silicon based fiber optic temperature sensor", *J. Phys. E: Sci. Instrum.* **21**, 652 (1988).
- ²⁰ S. Stueflotten, T. Chrisensen, S. Iversen, J. O. Hellvik, K. Almås, and T. Wien, "An infrared fiber optic gas detection system", *Proc. Second. Int. Conf. on Optical Fiber sensors (OFS'2)*, **87**, VDE-Verlag, Berlin, (1984).
- ²¹ A. R. Davis, S. S. Patrick, A. Dandridge, and F. Bucholtz, "Remote fiber optic AC magnetometer", *Electronics Letters* **28** (3), 271 (1992).
- ²² H. Sohlström, "Fiber optic magnetic field sensors utilizing iron garnet materials", PhD Dissertation Thesis, Royal Institute of Technology, Stockholm (1993).
- ²³ L. E. Helseth, R. W. Hansen, E. I. Il'yashenko, M. Baziljevich, and T. H. Johansen, "Faraday rotation spectra of bismuth –substituted ferrite garnet films with in plane magnetization", *Phys. Rev. B* **64**, 174406 (2001).
- ²⁴ G. F. Dionne, G. A. Allen, "Spectral origins of giant Faraday rotation and ellipticity in Bi-substituted magnetic garnets", *J. Appl. Phys.* **73**, 6127 (1993).
- ²⁵ A. V. Zenkov, and A. S. Moskvina, "Bismuth induced increase of the magneto-optical effects in iron garnets: a theoretical analysis", *J. Phys.: Condens. Matter* **14**, 6957 (2002).
- ²⁶ V. Doorman, J. P. Krumme, and H. Lenz, "Optical and magneto-optical tensor spectra of bismuth-substituted yttrium iron garnets films", *J. Appl. Phys.* **68** (7), 3544 (1990).
- ²⁷ K. Shinagawa, L. F. McAven, H. J. Ross, and P. H. Butler, "A note on the Faraday rotation in Bi³⁺-substituted magnetic garnets", *IEEE Trans. Magn.* **35** (5), 3136 (1999).
- ²⁸ A. K. Zvezdin and V. A. Kotov, "Modern magneto-optics and magneto-optical materials", Institute of Physics Publishing, (1997).
- ²⁹ R. Hergt, H. Pfeiffer, P. Görnert, M. Wendt, B. Keszei, and J. Vandlik, *Phys. Stat. Sol. (A)* **104**, 769 (1987).
- ³⁰ G. Gubbiotti, G. Carlotti, and B. Hillebrands, "Spin waves in ultrathin (111)-oriented cubic films", *J. Phys.: Condens. Matter* **10**, 2171 (1998).
- ³¹ J. E. Mee, G. R. Pulliam, J. L. Archer, and P. J. Besser, "Magnetic Oxide Films", *IEEE Trans. Magn.* **5** (4), 717 (1969).
- ³² P. Hansen, K. Witter, and W. Tolksdorf, "Magnetic and magneto-optical properties of bismuth-substituted gadolinium iron garnet films", *Phys. Rev. B* **27** (7), 4375 (1983).
- ³³ W. Wetting, "Magneto-optics of ferrites", *J. Magn. Magn. Mat.* **3**, 147 (1976).
- ³⁴ J. F. Nye, *Physical Properties of crystals*, Clarendon Press, Oxford, (1985).
- ³⁵ C. Holthaus, "Development of sensitive indicators for magneto-optical pattern recognition", PhD Dissertation Thesis, University of Osnabrück, (2004).

-
- ³⁶ J. Warner, "Nonreciprocal magneto-optic waveguides", *IEEE Trans. Microwave Theory Tech.* **23** (1), 70 (1975).
- ³⁷ D. I. Sementsov, A. M. Shutyi, O. V. Ivanov, "Optical mode conversion in a gyrotropic waveguide", *Pure Appl. Opt.* **4**, 663 (1995).
- ³⁸ C. Vassallo, *Optical Waveguide Concepts*, Elsevier Science Publishers, (1991).
- ³⁹ L. R. Walker, "Orthogonality relation for gyrotropic waveguides", *J. Appl. Phys.* **28**, 377 (1957).
- ⁴⁰ P. Diament, "Wave Transmission and Fiber Optics", Macmillan Publishing Company, New York (1990).
- ⁴¹ H. Dötsch, N. Bahlmann, O. Zhuromskyy, M. Hammer, L. Wilkens, R. Gerhardt, P. Hertel, and A. Popkov, "Applications of magneto-optical waveguides in integrated optics", *J. Optical Society of America B* **22** (1), 240 (2005).
- ⁴² N. Bahlmann, "Finite element simulations of integrated optical isolators and circulators in magnetic garnet films", PhD Dissertation Thesis, University of Osnabrück, (2004).
- ⁴³ T. Aichele, A. Lorenz, R. Hergt, and P. Görnert, "Garnet layers prepared by liquid phase epitaxy for microwave and magneto-optical applications – a review", *Cryst. Res. Technol.* **38** (7-8), 575 (2003).
- ⁴⁴ Y. Ikezawa, K. Nishimura, H. Uchida, M. Inoue, "Preparation of two-dimensional magneto-photonic crystals of bismuth substituted yttrium iron garnet materials", *J. Magn. Magn. Mat.* **272–276**, 1690 (2004).
- ⁴⁵ S. Kahl, "Bismuth iron garnet films for magneto-optical photonic crystals", PhD Dissertation Thesis, Royal Institute of Technology, Stockholm (2004).
- ⁴⁶ A. H. Eschenfelder, "Magnetic Bubble Technology", Springer-Verlag (1981).
- ⁴⁷ A. A. Polyanskii, X. Y. Cai, D. M. Feldmann, and D. C. Larbalestier, "Visualization of Magnetic Flux in Magnetic Materials and High Temperature Superconductors using the Faraday Effect in Ferrimagnetic Garnet Films," in proceedings of NATO Advanced Research Workshop, Sozopol, Bulgaria, I. Nedkov and M. Ausloos, eds., 353 (1999).
- ⁴⁸ J.E. Lenz, "A Review of Magnetic Sensors", *Proceedings of the IEEE*, **78** (6), 973 (1990).
- ⁴⁹ Y. N. Ning, B. C. B. Chu, and D. A. Jackson, "Miniature Faraday current sensor based on multiple critical angle reflections in a bulk-optic ring," *Opt. Lett.*, **16** (12), 1996 (1991).
- ⁵⁰ R. B. Wagreich and Christopher C. Davis, "Magnetic Field Detection Enhancement in an External Cavity Fiber Fabry-Perot Sensor", *J. Lightwave Technol.* **14** (10), 2246 (1996).
- ⁵¹ M. N. Deeter, G. W. Day, T. J. Beahn, and M. Manheimer, *Electron. Lett.* **29**, 993 (1993).
- ⁵² T. Numata, M. Yao, S. Inokuchi, and Y. Sakurai, "Improved sensitivity in novel scheme of magneto-optical field sensor", *IEEE Trans. Magn.* **27**, 5393 (1991).
- ⁵³ R. W. Hansen, L. E. Helseth, A. Solovyev, E. Il.Yashenko and T. H. Johansen, "Growth and characterization of (100) garnets for imaging", *J. Magn. and Magn. Mat.* **272-276**, 2247 (2004).

-
- ⁵⁴ V. J. Fratello, I. Mnushkina and S. J. Licht in *Magneto-Optical Imaging*, edited by T. H. Johansen and D. V. Shantsev, 311, Kluwer (2004).
- ⁵⁵ B. Keszei, Z. Vértesy and G. Vértesy, "Growth of Bi and Ga Substituted YIG and LuIG Layers by LPE Method", *Crystal Res. Tech.* **36**, 953 (2001).
- ⁵⁶ D. Mateika, and C. Rusche, "Coupled substitution of gallium by manganese and zirconium in single crystals of gadolinium gallium garnet", *J. Cryst. Growth*, **42**, 440 (1977).
- ⁵⁷ P. C. Dorsey, S. E. Bushnell, R. G. Seed, and C. Vittoria, "Epitaxial yttrium iron garnet films growth by pulsed laser deposition", *J. Appl. Phys.* **74** (2), 1242 (1993).
- ⁵⁸ S. Kahl, and A. M. Grishin, "Evolution of properties of epitaxial bismuth iron garnet films with increasing thickness", *J. Magn. and Magn. Mat.* **278**, 244 (2004).
- ⁵⁹ T. Okuda, N. Koshizuka, K. Hayashi, H. Kobani, and H. Yamamoto, *IEEE Trans. Magn.* **5**, 3491 (1987).
- ⁶⁰ R. Gerhardt, "Channel Waveguide Lasers in Epitaxial Garnet Films", PhD Dissertation Thesis, University of Osnabrück, (2001).
- ⁶¹ S. L. Blank, and J. W. Nielsen, "The growth of magnetic garnets by liquid phase epitaxy", *J. Cryst. Growth*. **17**, 302 (1972).
- ⁶² V.J. Fratello, S. E. G. Slusky, C.D. Brandle and M.P. Norelli. "Growth-Induced Anisotropy in Bismuth-Rare Earth Iron Garnets." *J. Appl. Phys.* **60**, 2488 (1986).
- ⁶³ A. S. Hudson, "Molecular engineering in the design of microwave ferrimagnetic garnets", *J. Phys. D: Appl. Phys.* **3**, 251 (1970).
- ⁶⁴ P. Hansen, K. Witter, and W. Tolksdorf, "Magnetic and magneto-optic properties of bismuth- and aluminum-substituted iron garnet films", *J. Appl. Phys.* **55** (4), 1052 (1984).
- ⁶⁵ P. Hansen, C.-P. Klages, J. Schuldt, and K. Witter, "Magnetic and magneto-optical properties of bismuth- substituted lutetium iron garnet films", *Phys. Rev. B* **31** (9), 5858 (1985).
- ⁶⁶ P. Andrei, M. Dimian, C. Krafft, I. D. Mayergoyz, D. I. Mircea, "Anisotropy characterization of garnet films by using VSM measurements", *J. Appl. Phys.* **93** (10), 7065 (2003).
- ⁶⁷ S.V. Vonsovskii, "Ferromagnetic resonance", Pergamon Press, (1966).
- ⁶⁸ J. Zhang, "Growth and FMR characterization of in-plane magnetization garnet thin films", Master Thesis, University of Maryland (2004).
- ⁶⁹ G. Bertotti, I. D. Mayergoyz, and C. Serpico, "Analysis of instabilities in nonlinear Landau-Lifshitz-Gilbert dynamics under circularly polarized fields", *J. Appl. Phys.* **91**, 7559 (2002).
- ⁷⁰ R. F. Soohoo, "Theory and application of ferrites", Prentice-Hall, (1960).
- ⁷¹ A. J. Baden-Fuller, "Ferrites at microwave frequencies", Peter Peregrinus London, (1987).
- ⁷² I. Nistor, C. Krafft, R. Rojas, and I. D. Mayergoyz, "Measurement of the magnetostriction constant of Bi-doped garnets by optical observation of stress-induced stripe domains", *IEEE Trans. Magn.* **40** (4), 2832 (2004).

-
- ⁷³ I. Nistor, I. D. Mayergoyz, R. Rojas, and C. Krafft, "Optical study of magnetostriction in (Bi, Ga) - substituted garnet thin films", *J. Appl. Phys.* **98**, 073901 (2005).
- ⁷⁴ I. Nistor, C. Krafft, R. Rojas, and I. D. Mayergoyz, "Magneto-optic studies of garnets subject to rotating magnetic fields", *J. Appl. Phys.* **97**, 10R302 (2005).
- ⁷⁵ M. R. Freeman, and J. F. Smyth, "Picosecond time-resolved magnetization dynamics of thin-film heads", *J. Appl. Phys.* **79** (8), 5898 (1996).
- ⁷⁶ G. A. Gehring, M. Ali, M. D. Cooke, and R. Mattheis, "Determination of magnetostriction in thin films using strained substrate techniques ", *J. Magn. Magn. Mat.* **257**, 15 (2003).
- ⁷⁷ W. C. Young and R. G. Budynas, "Roark's Formula for Stress and Strain", McGraw-Hill, New York, (2002).
- ⁷⁸ V. J. Fratello, S. J. Licht and M. P. Norelli, "Effect of melt composition on Bi incorporation in iron garnets", *J. Cryst. Growth* **97**, 657 (1989).
- ⁷⁹ R. M. Grechishkin, M. Yu. Goosev, E. Il'Yashenko, and N. S. Neustroev, "High-resolution sensitive magneto-optic ferrite-garnet films with planar anisotropy", *J. Magn. Magn. Mat.* **157**, 305 (1996).
- ⁸⁰ V. J. Fratello, I. Mnushkina and S. J. Licht, "Growth and Characterization of Magneto-optic Garnet Films with Planar Uniaxial Anisotropy", *Mater. Res. Soc. Symp. Proc.* **834**, Paper J6.2.2, (2005).
- ⁸¹ R. Rojas, C. Krafft, I. Nistor, D. Zhang, and I. D. Mayergoyz, "Growth effects (rotation rate) on the characteristics of Bi-substituted lutetium iron garnets", *J. Appl. Phys.* **95**, 6885 (2004).
- ⁸² P. Hansen, K. Witter, and W. Tolksdorf, "Magnetic and magneto-optical properties of bismuth-substituted gadolinium iron garnet films", *Phys. Rev. B* **27**, 4375 (1983).
- ⁸³ P. Hansen, C.-P. Klages, J. Schuldt, and K. Witter, "Magnetic and magneto-optical properties of bismuth-substituted lutetium iron garnet films", *Phys. Rev. B* **31**, 5858 (1985).
- ⁸⁴ W. van Erk, "The growth kinetics of garnet liquid phase epitaxy using horizontal dipping", *J. Cryst. Growth* **43**, 446 (1978).
- ⁸⁵ W. van Erk, and J. M. Robertson, "Segregation in liquid phase epitaxy of garnets ", *J. Cryst. Growth* **59**, 543 (1982).
- ⁸⁶ P. Hansen, "Anisotropy and magnetostriction of gallium-substituted yttrium iron garnet", *J. Appl. Phys.* **45**, 3638 (1974).
- ⁸⁷ P. Hansen, K. Witter, and W. Tolksdorf, "Magnetic and magneto-optic properties of bismuth- and aluminum-substituted iron garnet films", *J. Appl. Phys.* **55**, 1052 (1984).
- ⁸⁸ E. A. Giess, D. C. Cronmeyer, R. Ghez, E. Kloholm, and J. D. Kuptsis, *J. Amer. Ceram. Soc.* **56**, 593 (1973).
- ⁸⁹ R. Ghez and E. A. Giess, *Mater. Res. Bull.* **8**, 31 (1972).
- ⁹⁰ E. A. Giess, J. D. Kuptsis, and E. A. D. White, "Liquid phase epitaxial growth of magnetic garnet films by isothermal dipping in a horizontal plane with axial rotation", *J. Cryst. Growth* **16**, 36 (1972).

-
- ⁹¹ I. Nistor, C. Holthaus, C. Krafft, and I. D. Mayergoyz, "Development of LPE-grown (Bi, Gd, Lu)-substituted thin film iron garnets", *To appear in J. Appl. Phys.* **99**, (2006).
- ⁹² J. Burton, R. Prim, and W. Slichter, *J. Chem. Phys.* **21**, 1987 (1953).
- ⁹³ W. Tolksdorf, H. Dammann, E. Pross, B. Strocka, H. J. Tolle, and P. Willich, "Growth of Yttrium iron garnet multi-layers by liquid phase epitaxy for single mode magneto-optic waveguides ", *J. Cryst. Growth* **83**, 15 (1987).
- ⁹⁴ Vetoshko, P.M. et al., "Measuring low alternating magnetic fields by means of Bi-Containing rare-earth ferrite-garnet films with planar anisotropy," *J. Appl. Phys.*, **70** (10), 6298 (1991).
- ⁹⁵ Klank, M. et al., "Sensitive magneto-optical sensors for visualization of magnetic fields using garnet films of specific orientations," *J. of Appl. Phys.* **92** (11), 6484 (2002).
- ⁹⁶ H. Takeuchi, S. Ito, I. Mikami, and S. Taniguchi, "Faraday rotation and optical absorption of a single crystal of bismuth-substituted gadolinium iron garnet", *J. Appl. Phys.* **44**, 4789 (1973).
- ⁹⁷ H. Ferrari, V. Bekeris, and T. H. Johansen, "Direct observation of magnetic patterns in audio tapes," *Physica B* **354**, (2004).
- ⁹⁸ M. R. Koblishka, and R. J. Wijngaarden, "Magneto-optical investigations of superconductors", *Supercond. Sci. Technol.* **8**, 199 (1995).
- ⁹⁹ E. Huijter, J. C. Lehoucq, and J. P. Castera, "Analysis of medium-garnet interaction in a parallel high-density magneto-optic read head," *IEEE Trans. Mag.* **23** (3), 1919 (1987).
- ¹⁰⁰ H. Dammann, E. Pross, G. Rabe, W. Tolksdorf, and M. Zinke, "Phase matching in symmetrical single-mode magneto-optic waveguides by application of stress", *Appl. Phys. Lett.* **40** (26), 1755 (1986).
- ¹⁰¹ R. T. Lynch Jr., J. F. Dillon, Jr., and R. Wolfe, "Stress birefringence in ferrimagnetic garnets", *J. Appl. Phys.* **44**, 225 (1973).
- ¹⁰² A. N. Ageev, O. G. Rutkin, A. S. Trifonov, V. B. Kravtchenko, L. M. Filimonova, H. Le Gall, and J. M. Desvignes, *Rev. Phys. Appl.* **20**, 753 (1985).
- ¹⁰³ K. Ando, N. Takeda, N. Koshizuka, and T. Okuda, "Annealing effects on growth-induced optical birefringence in liquid-phase-epitaxial-grown Bi-substituted iron garnet films", *J. Appl. Phys.* **57**, 1277 (1985).
- ¹⁰⁴ H. Makino, Y. Hidaka, "Determination of magnetic anisotropy constants for bubble garnet epitaxial films using field orientation dependence in ferromagnetic resonances," *Mat. Res. Bull.*, vol. 16 (8), pp. 957-966, (1981).
- ¹⁰⁵ G. F. Dionne, "Molecular field coefficients of substituted yttrium iron garnets", *J. Appl. Phys.* **41** (12), 4874 (1970).
- ¹⁰⁶ G. R. Harrison, L. R. Hodges Jr, "Temperature Stable Microwave Hybrid Garnets", *J. Appl. Phys.* **33**, 1375 (1962).
- ¹⁰⁷ E. A. Maguire, and J.J. Green, "Magnetic Properties of Yttrium-Gadolinium-Aluminum-Iron Garnets", *J. Appl. Phys.* **33**, 1373 (1962).

-
- ¹⁰⁸ H. Dammann, E. Pross, G. Rabe, and W. Tolksdorf, "45 waveguide isolators with phase mismatch," *Appl. Phys. Lett.* **56**, 1302 (1990).
- ¹⁰⁹ T. Suzuki, F. Sequeda, H. Do, T. C. Huang, and G. Gorman, "Magnetic and magneto-optic properties of Bi-substituted garnet films crystallized by rapid thermal processing," *J. Appl. Phys.* **67**, 4435 (1990).
- ¹¹⁰ H. Kano, K. Shono, S. Kuroda, N. Koshino, and S. Ogawa, "Optimized structure of sputtered garnet disks," *IEEE Trans. Magn.* **25**, 3737 (1989).
- ¹¹¹ B. Bechevet, D. Challeton, B. Rolland, M. F. Armand, B. Valon, and J. Mouchot, "Rapid thermal annealing of CeDyGaIG films for magneto-optical disk storage," *J. Appl. Phys.* **69**, 4767 (1991).
- ¹¹² T. Suzuki, "Magnetic and magneto-optic properties of rapid thermally crystallized garnet films," *J. Appl. Phys.* **69**, 4756 (1991).
- ¹¹³ K. Shono, S. Kuroda, H. Kano, N. Koshino, and S. Ogawa, "Magneto-optical recording of sputtered garnet films crystallized during deposition," in *Proc. Materials Research Soc. Symp.* **150**, 131 (1989).
- ¹¹⁴ C.-J. Lin, "Materials for magneto-optic data storage," in *Proc. Materials Research. Soc. Symp.* **150**, 15 (1989).
- ¹¹⁵ M. Gomi, S. Satoh, and M. Abe, "Giant Faraday rotation of Ce-substituted YIG films epitaxially grown by RF sputtering," *Jpn. J. Appl. Phys.* **27**, L1536 (1988).
- ¹¹⁶ S. Mino, M. Matsuoka, A. Tate, A. Shibukawa, and K. Ono, "Completely Bi-Substituted Iron Garnet (BIG) films prepared by Electron Cyclotron Resonance (ECR) sputtering," *Jpn. J. Appl. Phys.* **31**, 1786 (1992).
- ¹¹⁷ J. Fujita, M. Levy, R.M. Osgood Jr., L. Wilkens, and H. Dötsch, "Waveguide optical isolator based on Mach-Zehnder interferometer," *Appl. Phys. Lett.* **76**, 2158 (2000).
- ¹¹⁸ B. J. H. Stadler and A. Gopinath, "Magneto-optical garnet films made by reactive sputtering," *IEEE Trans. Magn.* **36**, 3957 (2000).
- ¹¹⁹ G. Simsa, R. Gerber, T. Reid, R. Tesar, R. Atkinson, and P. Papakonstantinou, "Optical absorption and Faraday rotation of Barium Hexaferrite films prepared by laser ablation deposition," *J. Phys. Chem. Solids* **59**, 111 (1998).
- ¹²⁰ O. Heczko, R. Gerber, and Z. Simsa, "Structural, magnetic and magneto-optical properties of SrFe Al O hexaferrite thin films prepared by laser ablation deposition," *Thin Solid Films* **358**, 206 (2000).
- ¹²¹ S. A. Oliver, M. L. Chen, I. Kozulin, S. D. Yoon, X. Zuo, and C. Vittoria, "Growth and characterization of thick oriented Barium Hexaferrite films on MgO (111) substrates," *Appl. Phys. Lett.* **76**, 3612 (2000).
- ¹²² S. A. Oliver, M. L. Chen, I. Kozulin, and C. Vittoria, "Structure and magnetic properties of Barium Hexaferrite films deposited at low Oxygen pressures," *J. Magn. Magn. Mat.* **213**, 326 (2000).
- ¹²³ M. Tanaka, H. Shimizu, H. Hayashi, H. Shimada, and K. Ando, "Ferromagnetic semiconductor heterostructures based on (GaMn)As," *J. Vac. Sci. Technol.* **A18**, 1247 (2000).
- ¹²⁴ H. Shimizu and M. Tanaka, "Magneto-Optical properties of semiconductor-based superlattices having GaAs with MnAs nanoclusters," *J. Appl. Phys.* **89**, 7281 (2001).

¹²⁵ M. Levy, "The On-Chip Integration of Magneto-optic Waveguide Isolators", IEEE J. Sel. Topics Quantum Electron. **8** (6), 1300 (2002).

¹²⁶ M. Bruel, "The history, physics and applications of the smart-cut process," Mat. Res Soc. Bullet., 35 (1998).

¹²⁷ M. Levy, R. M. Osgood Jr., A. Kumar, and H. Bakhru, "Epitaxial liftoff of thin oxide layers: Yttrium iron garnets onto GaAs," Appl. Phys. Lett. **71**, 2617 (1997).

¹²⁸ R. C. Jones, "A new calculus for the treatment of optical systems; I. description and discussion of the calculus", J. Opt. Soc. Am. **31**, 488 (1941).